



저작자표시-비영리-변경금지 2.0 대한민국

이용자는 아래의 조건을 따르는 경우에 한하여 자유롭게

- 이 저작물을 복제, 배포, 전송, 전시, 공연 및 방송할 수 있습니다.

다음과 같은 조건을 따라야 합니다:



저작자표시. 귀하는 원저작자를 표시하여야 합니다.



비영리. 귀하는 이 저작물을 영리 목적으로 이용할 수 없습니다.



변경금지. 귀하는 이 저작물을 개작, 변형 또는 가공할 수 없습니다.

- 귀하는, 이 저작물의 재이용이나 배포의 경우, 이 저작물에 적용된 이용허락조건을 명확하게 나타내어야 합니다.
- 저작권자로부터 별도의 허가를 받으면 이러한 조건들은 적용되지 않습니다.

저작권법에 따른 이용자의 권리는 위의 내용에 의하여 영향을 받지 않습니다.

이것은 [이용허락규약\(Legal Code\)](#)을 이해하기 쉽게 요약한 것입니다.

[Disclaimer](#)

공학박사 학위논문

철강 산업에서 열처리 공정 부품의 새로운 설계 및  
성능 향상

**New Design and Performance Improvement of  
Components of Heat Treatment Process in Steel  
Industry**

울산대학교 대학원

기계공학과

**Ngo Thien Tu**

**Doctor of Philosophy**

**New Design and Performance Improvement of  
Components of Heat Treatment Process in Steel  
Industry**

**The Graduate School  
of University of Ulsan**

**School of Mechanical Engineering  
Ngo Thien Tu**

**New Design and Performance Improvement of  
Components of Heat Treatment Process in Steel  
Industry**

지도교수 이병룡

지도교수 이근식

이 논문을 공학박사 학위 논문으로 제출함

**2019년 05월**

울산대학교 대학원

기계공학과

**Ngo Thien Tu**

**New Design and Performance Improvement of  
Components of Heat Treatment Process in Steel  
Industry**

**Supervisor: Prof. Byung Ryong Lee**

**Supervisor: Prof. Geun Sik Lee**

**A Dissertation**

**Submitted to  
the Graduate School of University of Ulsan  
In partial Fulfillment of the Requirements  
for the Degree of**

**Doctor of Philosophy**

**by**

**Ngo Thien Tu**

**School of Mechanical Engineering  
University of Ulsan, Republic of Korea**

**May 2019**

Ngo Thien Tu 의 공학박사 학위 논문을 인준함

심 사 위원장 이목인



심 사 위 원 이근식



심 사 위 원 이병룡



심 사 위 원 장경식



심 사 위 원 김무근



울산대학교 대학원

2019 년 05 월

# New Design and Performance Improvement of Components of Heat Treatment Process in Steel Industry

This certifies that the dissertation  
of Ngo Thien Tu is approved.

  
\_\_\_\_\_  
Committee Chairman Prof. MOKIN LEE

  
\_\_\_\_\_  
Committee Member Prof. GEUN SIK LEE

  
\_\_\_\_\_  
Committee Member Prof. BYUNG RYONG LEE

  
\_\_\_\_\_  
Committee Member Prof. KYOUNG SIK CHANG

  
\_\_\_\_\_  
Committee Member Prof. MOO GEUN KIM

School of Mechanical Engineering  
University of Ulsan, Republic of Korea

May 2019

## **ACKNOWLEDGMENTS**

I would like to thank my supervisor Professor Byung Ryong Lee who helped me as well as comments and suggestions to accomplish my PhD thesis in the University of Ulsan. In addition, I would like to send my best sincerely thanks to my supervisor Professor Geun Sik Lee, who not only gave me motivation, encouragement, and providing enthusiasm but also supported me finance during my PhD course in the University of Ulsan. I am also owing to my Professor for his ideas, suggestions, comments and corrections to this thesis. I would like to thank partners in my lab for their cooperation.

Many thanks to the committee members for their help as well as comments and suggestions to improve my thesis. I sincerely thank the University of Ulsan for the scholarship support and opportunity to study in Korea. I am greatly thankful to the staffs at the school of Mechanical and Automotive Engineering for providing valuable expertness, helpful suggestions, and necessary environment for doing research and the other kindly helps.

My deepest thankfulness and love to my friends and family members for their love, encouragement and valuable advice during I studied in University of Ulsan, Korea. I am also thankful to the Union of Vietnamese Students in University of Ulsan and Korea, as well as the friends for spiritual helping and consulting about abroad living experience.

Ulsan, May 30, 2019

**NGO THIEN TU**

# Abstract

## New Design and Performance Improvement of Components of Heat Treatment Process in Steel Industry

Department of Mechanical Engineering

Ngo Thien Tu

For the steel preheating process, the three new gas torch models were designed to enhance the exit flow uniformity of a gas torch with multiple exit holes for effective heating of a steel plate. The objective of this study is to design and to improve performance of new components of heat treatment process in steel industry. The flow uniformity ( $\gamma$ ) of the velocity distribution of the multiple exit holes was investigated with the pressure drop ranging from 100 to 500 Pa. The basic model had flow uniformity ranging from 0.849 to 0.852, but the three new models had  $\gamma_1 = 0.901 - 0.912$ ,  $\gamma_2 = 0.902 - 0.911$ , and  $\gamma_3 = 0.901 - 0.914$ , respectively. The maximum percentage difference of the flow uniformity index between the three new models and the basic model was 7.3%. The basic model with non-uniform flow distribution made a temperature difference of the back side of the steel plate from the center to the edge of around 229°C, while the modified model with uniform flow distribution had a smaller temperature difference of 90°C. For the annealing furnace, the three new models were designed to reduce the temperature difference among the steel pipes by modifying the inlet structure of a furnace and arranging pertinently a bundle of the inside steel pipes. The elbow inlet generated the swirl flow horizontally and a downward injection angle ranging from 0 to 45 degrees generated the downward jet flow followed by the upward buoyancy flow. The temperature difference of a bundle of steel pipes for the basic model was 55.4°C. On the other hand, the temperature differences of a bundle of steel pipes for the three modified models with the downward inlet angle of 0 degrees, 30 degrees, and 45 degrees were 15.3°C, 13°C, and 23.6°C, respectively. Therefore, the elbow angle inlet of 30 degrees was selected to be the optimized angle to reduce the temperature difference among the bundle of steel pipes. The more increased Reynolds number at the inlet the more increased the temperature difference among the steel pipes. Effect of the horizontal ( $S_h/d$ ) and vertical ( $S_v/d$ ) steel spacing on the temperature difference of steel pipes was also examined. The lowest temperature difference of the bundle of steel pipes was achieved in  $S_h/d = 3.13$  and  $S_v/d = 1.56$ . In short, presently modified annealing furnaces had uniform temperature distribution on the bundle of steel pipes than the basic one.

**Keywords:** Flow uniformity of the gas torches; temperature distribution of steel plate in preheating; swirl flow; downward jet flow; upward buoyancy flow; annealing furnace.

# Contents

<b>Chapter 1. Introduction .....</b>	<b>1</b>
1.1 An overview of steel preheating process by gas torch and annealing process within annealing furnace in industry .....	1
1.1.1 Steel preheating before welding .....	1
1.1.2 Annealing furnace .....	2
1.2. Problem statement, necessary, objectives and thesis layout.....	4
<b>Chapter 2. Enhancement of exit flow uniformity by modifying the shape of a gas torch to obtain a uniform flow at the outlet of gas torch .....</b>	<b>7</b>
2.1 Principal operation of gas torch and applications.....	7
2.2 Enhancement of the uniform flow at the outlet of gas torch .....	9
2.2.1 Basic gas torch model.....	9
2.2.2 Three new models.....	10
2.3 Numerical simulation.....	13
2.4 Results and discussion.....	16
2.5 Summary .....	23
<b>Chapter 3. Flame jet behavior from gas torches with multiple exit holes and the temperature distribution of a steel plate .....</b>	<b>24</b>
3.1 System description of steel preheating process.....	24
3.2 Mathematic model.....	26
3.2.1 Boundary condition and numerical simulation .....	30
3.2.2 Grid independence check.....	34
3.3 Comparison of the temperature distribution at the back side of a steel plate between the experiment and simulation.....	35
3.4 Comparison of flame structure and steel plate temperature distribution of the models with and without guide vane .....	44
3.5 Unsteady temperature distribution at the back side of steel plate.....	48
3.6 Effect of operational variables on temperature distribution at steady state.....	51
3.6.1 Effect of equivalent ratio ( $\Phi$ ) on temperature .....	51
3.6.2 Effect of Reynolds number (Re) on temperature .....	53
3.6.3 Effect of the distance from gas torch outlet to steel plate on temperature... ..	55
3.7 Optimizing the guide vane angle on the gas torch outlet surface.....	56
3.8 Summary.....	58

<b>Chapter 4. Study of flow field and temperature distribution of Hot Mixing Chamber (HMC) .....</b>	<b>60</b>
<b>4.1 Description of operating principle of Hot Mixing Chamber (HMC).....</b>	<b>60</b>
<b>4.2 Basic and modified HMC models .....</b>	<b>61</b>
<b>4.2.1 Basic HMC model.....</b>	<b>61</b>
<b>4.2.2 Modified HMC model .....</b>	<b>62</b>
<b>4.3 Boundary conditions and method.....</b>	<b>64</b>
<b>4.4 Comparison between the basic and modified HMC model .....</b>	<b>66</b>
<b>4.5 Experimental validation .....</b>	<b>70</b>
<b>4.6 Summary.....</b>	<b>72</b>
<b>Chapter 5. Enhancement of Mixing and Temperature Distribution of Steel Pipes inside an Annealing Furnace by Adopting a Modified Inlet Structure .....</b>	<b>73</b>
<b>5.1 Introduction.....</b>	<b>73</b>
<b>5.2 Annealing furnace models .....</b>	<b>75</b>
<b>5.2.1 Basic model .....</b>	<b>75</b>
<b>5.2.2 Modified annealing furnace models.....</b>	<b>76</b>
<b>5.3 Mathematical model and boundary conditions .....</b>	<b>79</b>
<b>5.3.1 Mathematical model.....</b>	<b>79</b>
<b>5.3.2. Boundary conditions and grid independence checking .....</b>	<b>80</b>
<b>5.4 Results and discussions .....</b>	<b>82</b>
<b>5.4.1 Flow field and steel pipe temperature distribution of the basic model.....</b>	<b>82</b>
<b>5.4.2 Validation for the three modified models .....</b>	<b>85</b>
<b>5.4.3 Flow fields and steel pipes temperature distribution of the modified models.....</b>	<b>86</b>
<b>5.5 Effect of Reynolds number at the inlet and the horizontal and vertical steel spacing on the steel temperature difference among steel pipes.....</b>	<b>93</b>
<b>5.5.1 Effect of Reynolds number at the inlet on the temperature difference among the steel pipes .....</b>	<b>93</b>
<b>5.5.2 Effect of horizontal steel spacing on steel temperature difference among the steel pipes .....</b>	<b>94</b>
<b>5.5.3 Effect of vertical steel spacing on steel temperature difference among the steel pipes .....</b>	<b>95</b>
<b>5.6 Unsteady state 3D simulation during annealing process .....</b>	<b>96</b>
<b>5.7 Total deformation of steel pipes during annealing process.....</b>	<b>99</b>
<b>5.8 Summary.....</b>	<b>102</b>

<b>Chapter 6. Conclusions and Further Works.....</b>	<b>104</b>
<b>6.1 Conclusions .....</b>	<b>104</b>
<b>6.2 Limitations and Further Works.....</b>	<b>106</b>

## LIST OF FIGURES

<b>Figure 1.1</b> The gas torches for steel preheating: (a) single hole; (b) multi-holes.....	2
<b>Figure 1.2</b> (a) Schematic diagram of annealing process; (b) Steel pipes are arranged before annealing process .....	3
<b>Figure 1.3</b> Objective and interrelation among chapters in this whole thesis .....	4
<b>Figure 2.1</b> Comparison of typical flow field and temperature distribution of a steel plate: (a) Basic gas torch; (b) Modified gas torch.....	8
<b>Figure 2.2</b> Diagram of a basic gas torch .....	9
<b>Figure 2.3</b> The inner and outer shapes of three new gas torch models: (a) model 1; (b) model 2; (c) model 3 .....	12
<b>Figure 2.4</b> Meshes and boundary conditions of a three-dimensional gas torch.....	14
<b>Figure 2.5</b> Grid-independence check for velocity at the outlets along the lengthwise (x) direction.....	16
<b>Figure 2.6</b> (a) Pressure contour of the basic gas torch, (b) Inside streamline and velocity vector at the outlet .....	17
<b>Figure 2.7</b> Pressure contours at the middle plane of the three new gas torches: (a) model 1; (b) model 2; (c) model 3 .....	18
<b>Figure 2.8</b> Inner streamlines and velocity vectors at the outlet of the three new gas torches: (a) model 1; (b) model 2; (c) model 3 .....	20
<b>Figure 2.9</b> Exit velocity distribution along the lengthwise direction of the basic and three new gas torches .....	21
<b>Figure 2.10</b> Comparison of velocity uniformity index at the outlet between the basic torch and the three new gas torches as a function of pressure drop .....	23
<b>Figure 3.1</b> Experiment apparatus setup: (a) basic model; (b) Modified model; (c) TVS-200EX infrared camera and back side of the steel plate .....	26
<b>Figure 3.2</b> Schematic diagram of steel preheating process with gas torch, fluid domain, and steel plate; (a) A half model (x-y plane cut view); (b) Three-dimensional magnified view of the quarter model; (c) Mesh model of the quarter model .....	31
<b>Figure 3.3</b> Grid independence check with increasing elements .....	35

<b>Figure 3.4</b> The temperature contours of a combustion flame zone at the center-line view during the steel-plate preheating process: (a) Basic model; (b) Modified model .....	36
<b>Figure 3.5</b> The species mole fraction and temperature variations of the stoichiometric LPG/air mixture for the basic model and modified model.....	37
<b>Figure 3.6</b> Steel plate temperature distribution at the back-side with the incomplete combustion $\Phi = 1.4$ : (a) Basic model experiment; (b) Basic model simulation; (c) Modified model experiment; (d) Modified model simulation .....	40
<b>Figure 3.7</b> Steel plate temperature distribution at the backside with the complete combustion $\Phi = 1.0$ : (a) Basic model experiment; (b) Basic model simulation; (c) Modified model experiment; (d) Modified model simulation .....	42
<b>Figure 3.8</b> Comparison of the temperature distribution at the backside steel plate from the center to the edge for the complete combustion .....	43
<b>Figure 3.9</b> Comparison of the temperature distribution at the backside steel plate from the center to the edge for the complete combustion .....	44
<b>Figure 3.10</b> Comparison of the temperature distribution with and without the guide vanes as a function of $Y/d$ . .....	45
<b>Figure 3.11</b> Temperature contours from the gas torch outlets to the steel plate at the center view (left) and side view (right) section when preheating the steel plate at $\Phi = 1$ , $Re = 3483$ , and $Y/d = 50$ : (a) With guide vanes; (b) without guide vanes .....	47
<b>Figure 3.12</b> Temperature contours at the bottom surface of the steel plate for two models at the operating conditions of $\Phi = 1$ , $Re = 3483$ , and $Y/d = 50$ : (a) With guide vanes; (b) without guide vanes.....	48
<b>Figure 3.13</b> Temperature contour on the backside of steel plate: (a) Numerical simulation; (b) Experiment results .....	50
<b>Figure 3.14</b> Temperature at the center point of the back-side of the steel plate as a function of time during steel preheating process.....	51
<b>Figure 3.15</b> (a) Temperature distribution for various equivalent ratios as a function of $Y/d$ . (b) enlarged only for the steel plate thickness .....	52
<b>Figure 3.16</b> Effect of the Reynolds number on temperature distribution (a) as a function of $Y/d$ , (b) enlarged for only the steel plate thickness range.....	54
<b>Figure 3.17</b> Effect of distance from the gas torch on the temperature distribution along the x-direction from the center to the edge on the back side of the steel plate .. ..	55

<b>Figure 3.18</b>	Guide vane angle variation from the jet flow of the gas torch .....	56
<b>Figure 3.19</b>	Effect of the guide vane angle variations on the temperature distribution: (a) as a function of $Y/d$ , (b) enlarged for only the steel plate thickness range	58
<b>Figure 4.1</b>	Operating principle of Hot Mixing Chamber .....	61
<b>Figure 4.2</b>	The 3D basic model of Hot Mixing Chamber .....	62
<b>Figure 4.3</b>	The 3D modified model of Hot Mixing Chamber .....	64
<b>Figure 4.4</b>	The 3D mesh model of Hot Mixing Chamber: (a) Basic model; (b) Modified model .....	65
<b>Figure 4.5</b>	Velocity streamline of Hot Mixing Chamber: (a) Basic model; (b) Modified model .....	67
<b>Figure 4.6</b>	Surface temperature of Hot Mixing Chamber: (a) Basic model; (b) Modified model .....	68
<b>Figure 4.7</b>	The temperature contour of Hot Mixing Chamber: (a) at the center section; (b) Multi-sections inside HMC .....	69
<b>Figure 4.8</b>	HMC experiment apparatus setup: (a) front view; (b) side view .....	71
<b>Figure 4.9</b>	Comparison of the temperature distribution between simulation and experimental results along HMC length .....	72
<b>Figure 5.1</b>	(a) Schematic diagram of the annealing process; (b) Steel pipes are arranged before annealing process .....	74
<b>Figure 5.2</b>	The basic model with dimensions; (a) 3D view; (b) front-view .....	76
<b>Figure 5.3</b>	The modified model (a) 3D view; (b) Top and front view .....	78
<b>Figure 5.4</b>	Three kinds of the angle of elbow inlet; (a) 0 degrees, (b) 30 degrees and (c) 45 degrees .....	78
<b>Figure 5.5</b>	Three dimensional mesh model .....	81
<b>Figure 5.6</b>	Flow field distribution within the basic model; (a) 3D view; (b) bottom view; (c) side view .....	83
<b>Figure 5.7</b>	Flow temperature distribution within the basic furnace model .....	84
<b>Figure 5.8</b>	Steel pipe temperature distribution within the basic model .....	85
<b>Figure 5.9</b>	Velocity streamline at the side and bottom views of three kinds of the elbow inlet angle; (a) 0 degrees, (b) 30 degrees and (c) 45 degrees .....	89

<b>Figure 5.10</b> Flow field and temperature distribution of the flow at the inlet cross-section plane view of three kinds of the elbow inlet angle; (a) 0 degrees, (b) 30 degrees and (c) 45 degrees.....	90
<b>Figure 5.11</b> Flow temperature at every pipe position of the three modified models....	91
<b>Figure 5.12</b> Temperature distribution of steel pipes for annealing process; (a) 0 degrees, (b) 30 degrees and (c) 45 degrees.....	93
<b>Figure 5.13</b> Temperature difference of the bundle of steel pipes as a function of Reynolds number for model 2 with the elbow inlet angle of 30 degrees.....	94
<b>Figure 5.14</b> Temperature difference of steel pipes as a function of horizontal spacing to steel pipe diameter ratio at $S_v/d = 1.56$ . .....	95
<b>Figure 5.15</b> Temperature difference of steel pipes as a function of vertical spacing to steel pipe diameter ratio at $S_h/d = 1.56$ . .....	96
<b>Figure 5.16</b> Steel pipes temperature as a function of process time. ....	97
<b>Figure 5.17</b> Temperature distribution contour along steel pipes of three kind of time step: (a) 605s; (b) 10800s; (c) 20005s. ....	99
<b>Figure 5.18</b> Constrains condition of the bundle of steel pipes. ....	100
<b>Figure 5.19</b> The total deformation of steel pipes variation to three kind of time step: (a) 606s; (b) 10710s; (c) 20005s. ....	102
<b>Figure 6.1</b> Waste heat recovery from annealing furnace using TEG device.....	108

## LIST OF TABLES

<b>Table 2.1</b> Specification of a basic gas torch .....	9
<b>Table 2.2</b> The dimensions of inner and outer shapes of the three new models .....	12
<b>Table 2.3</b> Boundary conditions and numerical method .....	13
<b>Table 3.1</b> Boundary condition and numerical simulation method.....	33
<b>Table 4.1</b> Specification of the basic HMC.....	62
<b>Table 4.2</b> Specification of the modified HMC.....	63
<b>Table 4.3</b> The boundary condition of HMC .....	66
<b>Table 5.1</b> Dimensions of the basic annealing furnace and steel pipes.....	76
<b>Table 5.2</b> Boundary conditions and method .....	81
<b>Table 5.3</b> Percentage reduction of temperature difference among steel pipes between the three modified models and basic model .....	93
<b>Table 5.4</b> Mechanical properties of steel pipes.....	100

## NOMENCLATURES AND ABBREVIATION

### Nomenclature

- $A$  : Empirical constant equal to 4.0
- $B$  : Empirical constant equal to 0.5
- $d$  : Jet hole diameter (mm) / Steel pipe diameter
- $D_{i,m}$  : Mass diffusion coefficient for species  $i$
- $D_{T,i}$  : Thermal diffusion coefficient
- $E$  : Total energy (J)
- $f_i$  : Body force
- $G_k$  : Production of turbulence kinetic energy
- $G_\varepsilon$  : Generation of turbulence due to buoyancy
- $h_i$  : Enthalpy of species  $i$
- $H$  : Distance between the torch outlet and the steel plate (m)
- $I$  : Unit tensor
- $J_i$  : Diffusion flux of species  $i$
- $k$  : Turbulent kinetic energy per unit mass (J/kg)
- $M_{w,i}$  : Molecular weight of species  $i$
- $p$  : Pressure (Pa)
- $R_i$  : Net rate of production of species  $i$
- $Re$  : Reynolds number
- $S_h$  : Horizontal of pipes
- $S_v$  : Vertical of pipes
- $S_i$  : The rate of creation
- $Sc_t$  : The turbulent Schmidt number
- $T$  : Temperature (C)
- $u$  : Velocity (m/s)
- $u^T$  : Transpose velocity
- $v'_{i,r}$  : Stoichiometric coefficient for reactant  $i$  in reaction  $r$

$v''_{i,r}$	: Stoichiometric coefficient for product $i$ in reaction $r$
$Y_i$	: Local mass fraction of each species
$Y_P$	: Mass fraction of any product species, P
$Y_R$	: Mass fraction of a particular reactant, R
$Y/d$	: Non-dimensional length
$\beta$	: Coefficient of thermal expansion
$\rho$	: Density (kg/m <sup>3</sup> )
$\tau$	: Non-dimensional temperature
$\varepsilon$	: Turbulent dissipation rate (m <sup>2</sup> s <sup>-3</sup> )
$\Phi$	: Equivalent ratio

### Abbreviations

CFD	: Computational Fluid Dynamics
LPG	: Liquefied Petroleum Gas

### Subscripts

$ad$	: Adiabatic
$b$	: Buoyancy
$h$	: Horizontal space
$i$	: Species
jet	: Jet holes
$mix$	: LPG/air mixture
$p$	: Y-branch pipe
$P$	: Products
$R$	: Reactants
$unb$	: Unburned
$stoic$	: Stoichiometric
$t$	: triangle shape / turbulent
$v$	: Vertical space

---

## Chapter 1:

---

# Introduction

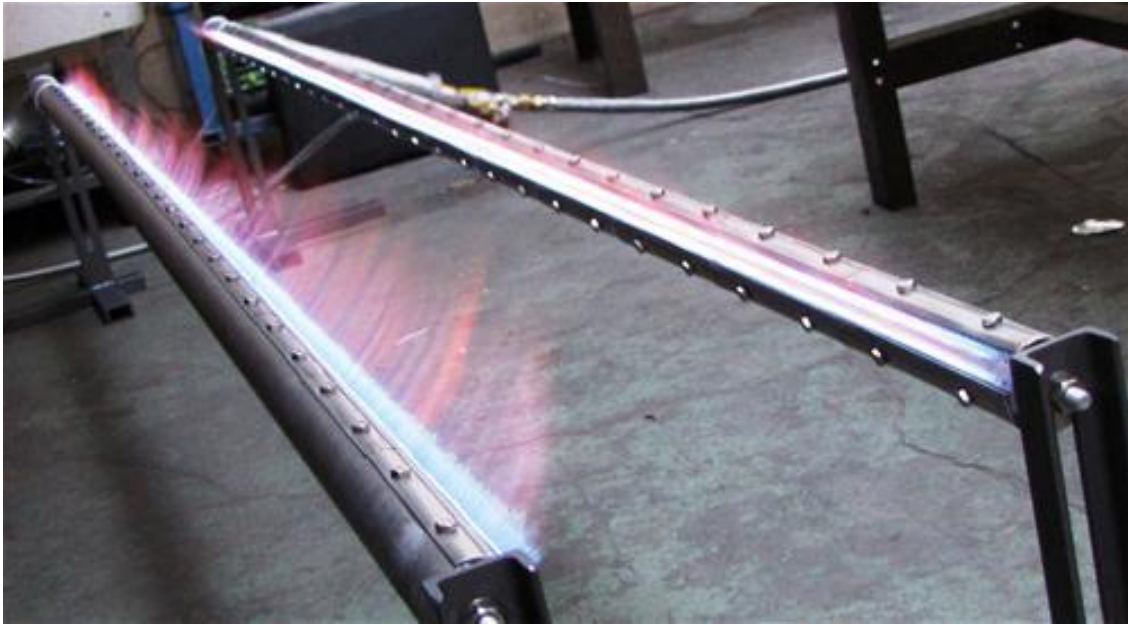
## 1.1 An overview of steel preheating process by gas torch and annealing process within annealing furnace in industry

### 1.1.1 Steel preheating before welding

Preheating involves heating the base of metal, either in a whole or just the region surrounding the joint to a specific desired temperature, it is called the preheat temperature, prior to welding. This may be necessary to reduce residual stress of metal and the hardness of the weld heat affected zone and avoid cracking of the weld metal. The need for steel preheating increases with a steel thickness or welding restraint to reduce the destruction of a metal. Preheat is commonly applied with fuel gas torches or electrical resistance heaters. Depending on the shape of the welding part of metal, the single hole or multiple holes at the outlet of gas torches can be used for steel preheating as shown in Figure 1.1.



(a)

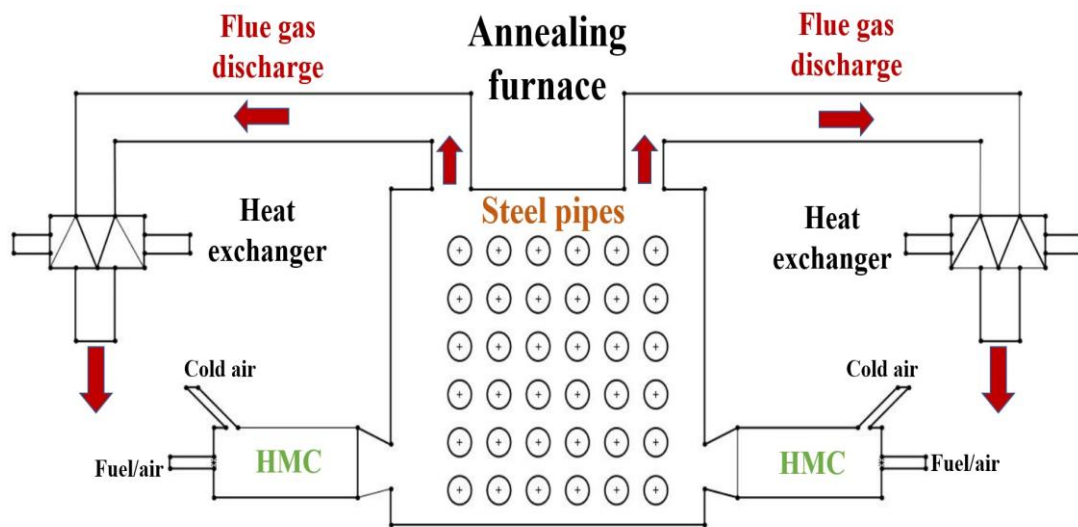


(b)

**Figure 1.1.** The gas torches for steel preheating: (a) single hole; (b) multi-holes

### **1.1.2 Annealing furnace**

Steels annealing is a process of heat treatment that alters the properties of steel to increase its ductility and also make it more workable. The annealing process is heating the steels arranged within furnace (heating period) to improve yield strength and holding at a constant temperature for a certain time (soaking period) to reform and enhance the grain crystalline structure then finally cooling at a predetermined rate (cooling period). In this study, the HMC (Hot Mixing Chamber) is the heat source which supply to annealing furnace for steel annealing arranged within the furnace. By using HMC, heat source can be adjusted by varying the Reynolds number of fuel/air mixture or equivalent ratio of the combustion process. The annealing process is showed in Figure 1.2.



(a)



(b)

**Figure 1.2** (a) Schematic diagram of annealing process; (b) Steel pipes are arranged before annealing process

## 1.2. Problem statement, necessary, objectives and thesis layout

Preheating by a gas torch is a common method, as it is easy to use and offers simple setup and portability. Also, the initial investment cost is low, and the process is one welder usually know. Steel preheating before welding helps to lessen shrinkage stresses that can lead to cracking and distortion. Due to hot materials expand and cool materials contract, a large temperature variance between the molten weld pool and the relatively cool base material can result in internal stresses as the weldment tries to normalize those temperature differences. These internal stresses increase the risk of cracking and distortion.

For the steel annealing process, steel annealing is a term that refers to the heat treatment processes carried out on metals. During the annealing process, steels are heated evenly to return them to as close to their pre-cold worked state as possible. This heat treatment process increases a metal’s ductility and ensures that metal with forming and shaping are more efficient processes.

**The objectives of this research are shown as below:**

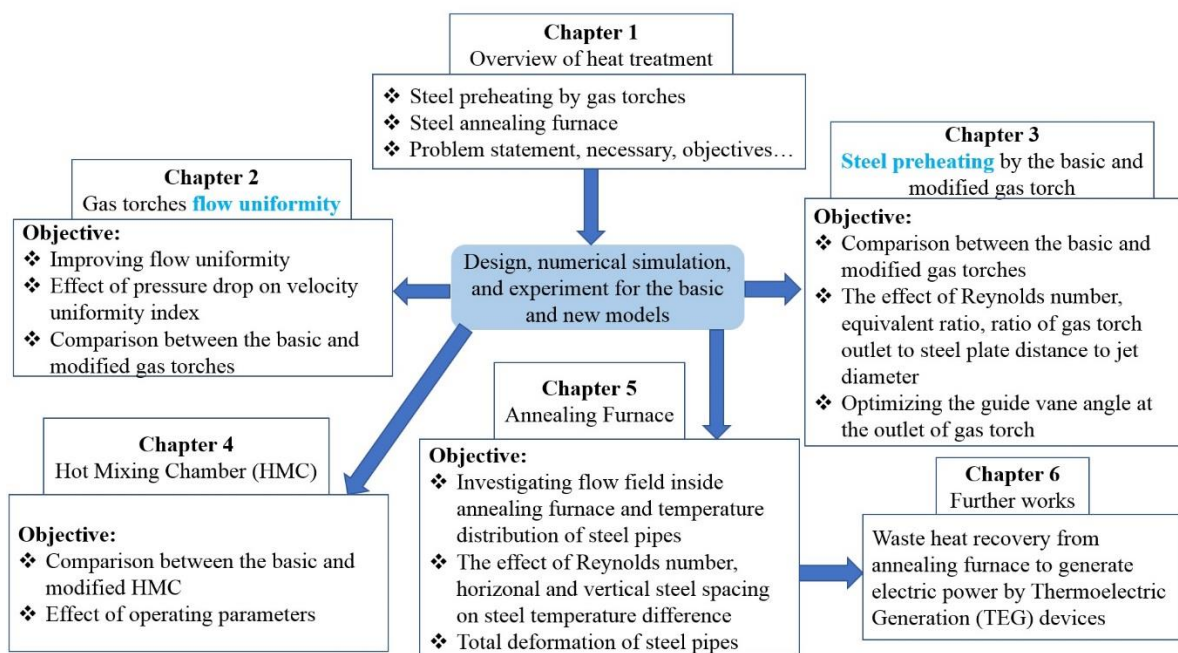


**Figure 1.3** Objective and interrelation among chapters in this whole thesis

- Numerical simulation is conducted to improve of exit flow uniformity by modifying the inner and outer shape of gas torch for steel plate preheating by CFD software ANSYS FLUENT 18.2. To get easy to handle, the model is manufactured with one inlet and multi-outlets. The problem of the original model is high flow concentrates at the center and low flow at the edge at the outlet of gas torch. Hence, three kind models were investigated to enhance the uniform flow distribution at the outlet of the gas torch by modifying the inner and outer shape of gas torch. Moreover, the steel preheating combustion process for original and modified model are performed to compare the temperature distribution on the back side of the steel plate.

- Investigating on multiple fuels like as LPG (Liquefied Petroleum Gas) with turbulent combustion and premixed flame multi-jets (array flame jets) simultaneously are rarely reported. Therefore, numerical simulation using ANSYS FLUENT software and conducting experiment for validation. The temperature distribution on the back side of steel plate varies with time during preheating process are examined. The effect of equivalent ratio ( $\Phi$ ), Reynolds number ( $Re$ ) and the ratio of burner tip plate spacing to nozzle diameter ( $Y/d$ ) are also investigated. Moreover, optimizing the angle between guide vane and horizontal direction variation at the jet outlets of the gas torch to increase temperature achievement when combustion happened.

- HMC (Hot Mixing Chamber) combustion process is studied to reduce surface temperature of HMC. The basic model with 1 cold air inlet and the modified model with 3 cold air inlets are also investigated and compared. Experiment is conducted to validate numerical simulation results.

- Annealing furnace is investigated on flow fields and temperature distribution of steel pipe simultaneously for original and three modified models. After selecting the annealing furnace which has the lowest steel pipes temperature difference in among four models, the effect of Reynolds number on steel pipe temperature difference is examined. Moreover, the horizontal and vertical spacing to steel pipe diameter ratio are also

studied to optimize the lowest steel pipe temperature difference. Transient simulation is also carried out to study the steel pipes temperature variation during annealing process. Moreover, total deformation of steel pipes arranged inside furnace is examined.

**The structure of dissertation is organized as follows:**

**Chapter 2** starts with the steel preheating by gas torches. Enhancing uniform flow at the outlet of gas torches by modifying the inner and the outer of gas torch. Effect of pressure drop on uniformity index is carried out in the middle of this chapter. The last chapter summaries and compare the original and modified models.

**Chapter 3** introduces the steel preheating combustion between the original and modified model. Comparing the numerical simulation and experimental results for transient and steady state on both of models. In addition, the effect of Reynolds number, equivalent ratio and gas torch outlet to steel plate distance also examined.

**Chapter 4** describes and compare the basic and modified HMC models. Reducing surface temperature of HMC during combustion. Experiment is conducted to validate numerical simulation results.

**Chapter 5** investigates flow field within steel annealing furnace and temperature distribution of steel pipes at transient and steady state. Effect of Reynolds number at the inlet, horizontal and vertical steel spacing on steel temperature difference. Total deformation of steel pipes during annealing process is also examined.

**Chapter 6** conclusions and the further works.

# Enhancement of exit flow uniformity by modifying the shape of a gas torch to obtain a uniform flow at the outlet of gas torch

## 2.1 Principal operation of gas torch and applications

Figure 2.1 shows the steel-plate preheating by a gas torch using Liquefied Petroleum Gas (LPG) as a fuel. The LPG passes the flow rate gauge and then enters the gas torch. In addition, compressed air enters the gas torch for combustion. The fuel and the compressed air are mixed together inside the torch. After leaving the exits, the fuel/air mixture is ignited, and then the combustion flame is used for preheating a steel plate. The steel plate in this study has a width, length, and thickness of 0.8 m, 1.5 m, and 0.02 m, respectively. Due to the non-uniform flow at the outlets of the basic model, the flame is also non-uniform during the preheating process of the steel plate, as shown in Figure 2.1(a). Consequently, the temperature distribution at the back side of the steel plate is also non-uniform when using the basic gas torch model. Hence, three modified models were designed to enhance the flow uniformity at the outlets of the gas torch, as shown in Figure 2.1(b).

This study aims to improve the exit flow uniformity by modifying the inner and outer shape of a gas torch for preheating a steel plate. For easy handling, the model was manufactured with one inlet and multiple outlets. The problem of the basic model is non-uniform flow at the outlet of the gas torch with high velocity at the center region

and low velocity at the edge. Hence, three kinds of models were designed to enhance the uniform flow distribution at the outlets of the gas torch. The applications of steel preheating by gas torch is the process to raise the temperature of the steel plate before welding. Uniform temperature distribution on steel plate significantly influence to the welding process. It is required the flame as well as the flow have uniformly distributed at the outlet of gas torch.

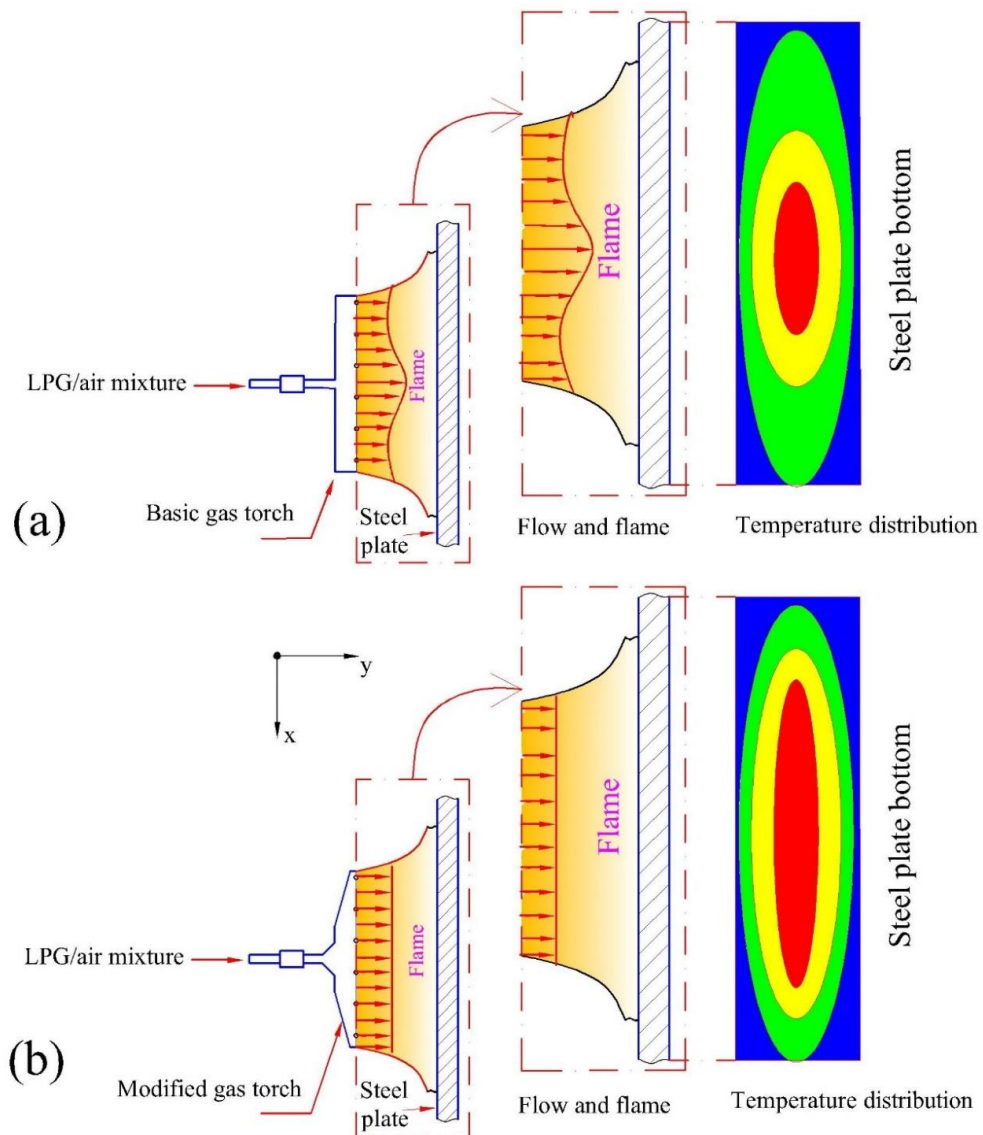


**Figure 2.1** Comparison of typical flow field and temperature distribution of a steel plate: (a) Basic gas torch; (b) Modified gas torch.

## 2.2 Enhancement of the uniform flow at the outlet of gas torch

### 2.2.1 Basic gas torch model

A diagram of a gas torch is shown in Figure 2.2. The gas torch is made of stainless steel and consists of one inlet and multiple outlets. The dimensions are listed in Table 2.1. A cylindrical tube with a diameter of 35 mm is connected to a rectangular block with 115 exit holes at the bottom surface. The fuel/air mixture enters the inlet at gauge pressure ranging from 100 to 500 Pa. Then, the flow spreads to the two sides of the gas torch and leaves the outlet holes.

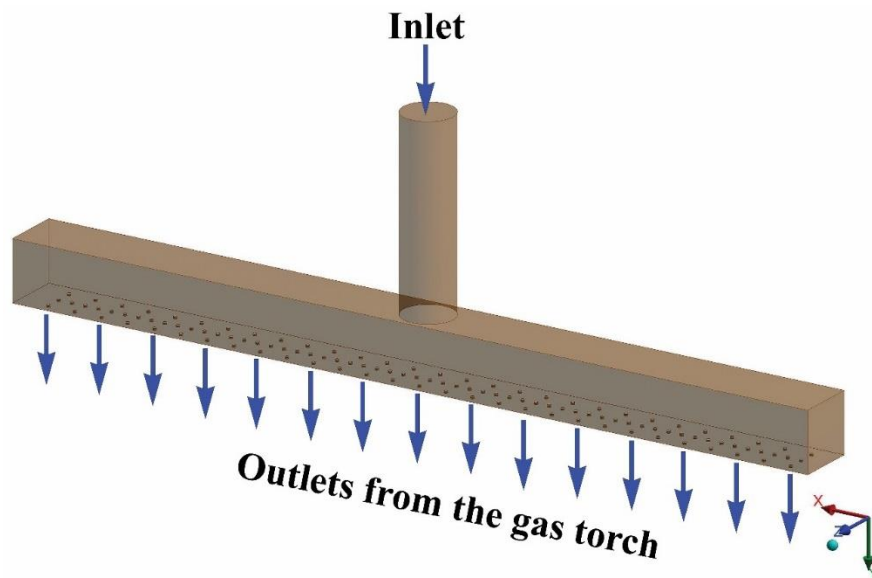


**Figure 2.2** Diagram of a basic gas torch

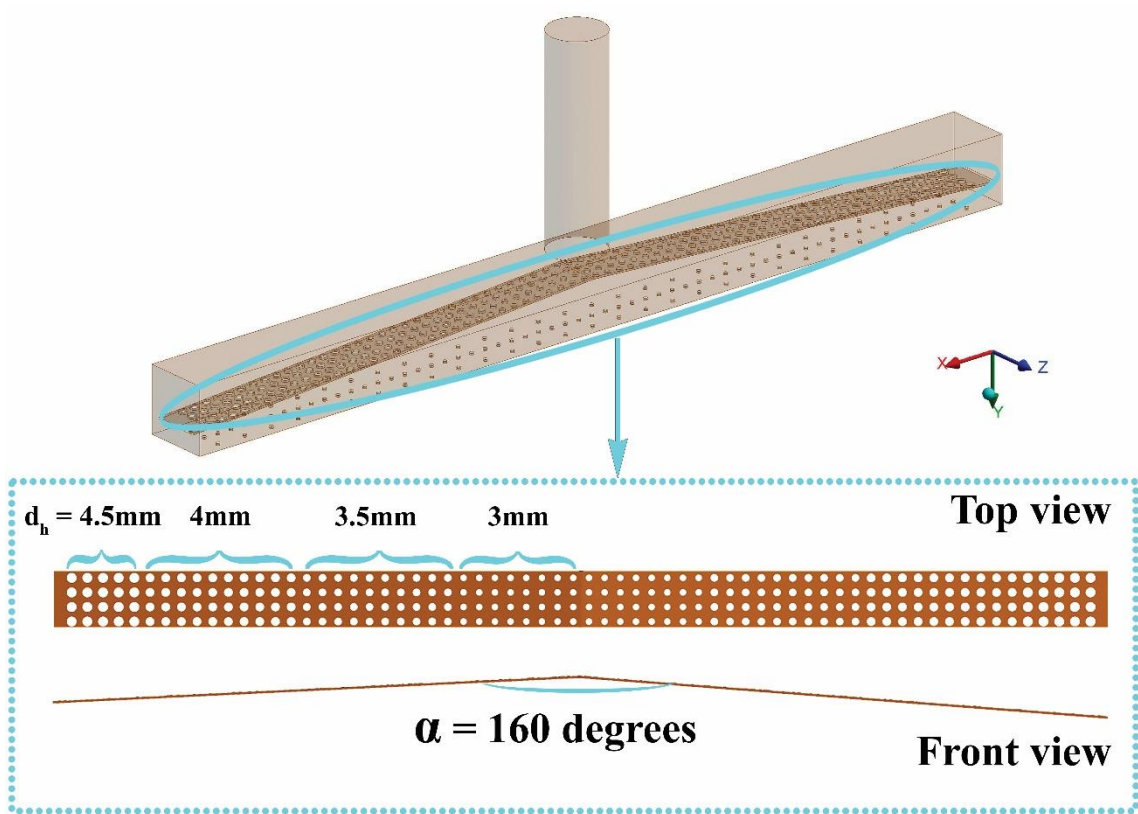
**Table 2.1.** Specification of a basic gas torch

Parameters	Dimensions, mm
Inlet diameter	35
Outlet diameter	2
Rectangular shape length	480
Number of holes	115

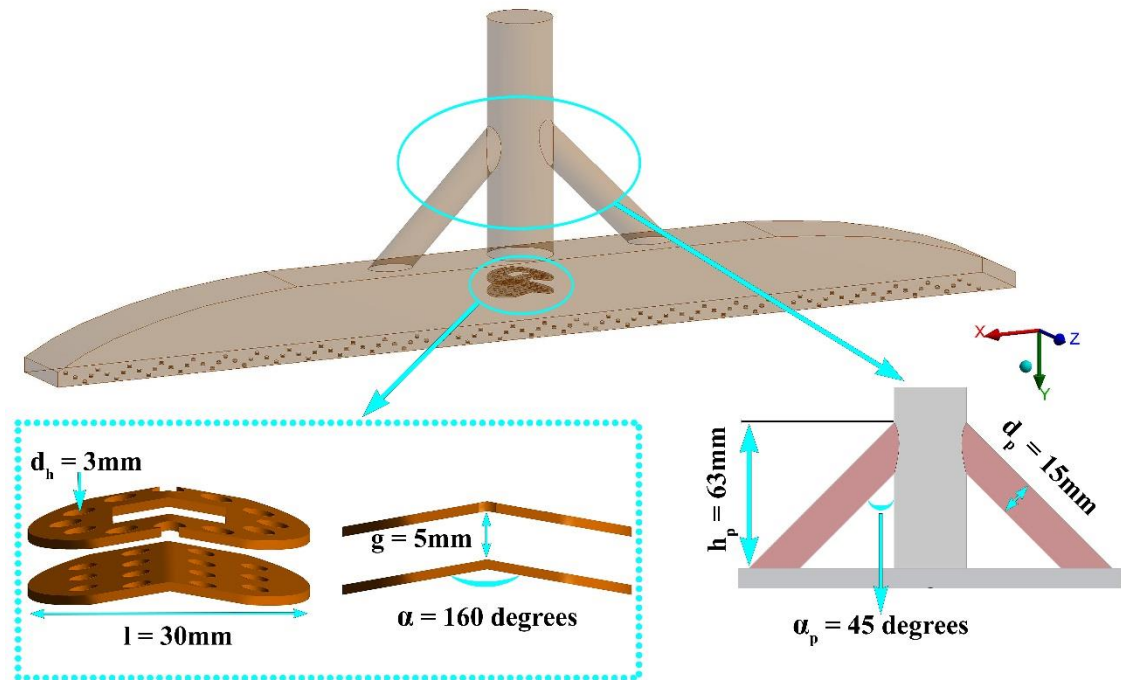
### 2.2.2 Three new models

Figure 2.3 shows the three new models used to improve the flow distribution at the outlets, which are compared with the basic model. The detailed dimensions of the inner and outer shapes of the new models are shown in Table 2.2. Model 1 has a long perforated strip that is divided into 4 parts with different hole diameters from the center to the right and left ends. The holes in the center region have a diameter of 3 mm. From the center hole to the end hole, the diameters sizes are followed by proportions of  $\alpha = 1, 1.17, 1.33, \text{ and } 1.5$ , respectively. The inlet flow approaches the long perforated strip and splits to the two sides along the strip. Part of the flow passes through the strip holes and then mixes together with the other flows.

Model 2 has a reverse Y-branch (2 symmetric bypass pipes in the inlet region), a two-stage diffuser in the center flow region, and a cut corner shape at both ends. The two bypass pipes have a diameter of 15 mm. The angle and height of the bypass pipe based on the center pipe are 45 degrees and 63 mm, respectively. The two stages of the diffuser have angles of 160 degrees. Model 3 has an enlarged inlet with triangular shapes. The two triangle-shape parts have a height of 63 mm, an angle of 45 degrees, a short perforated strip in the center flow region, and a cut corner shape at both ends.



(a)



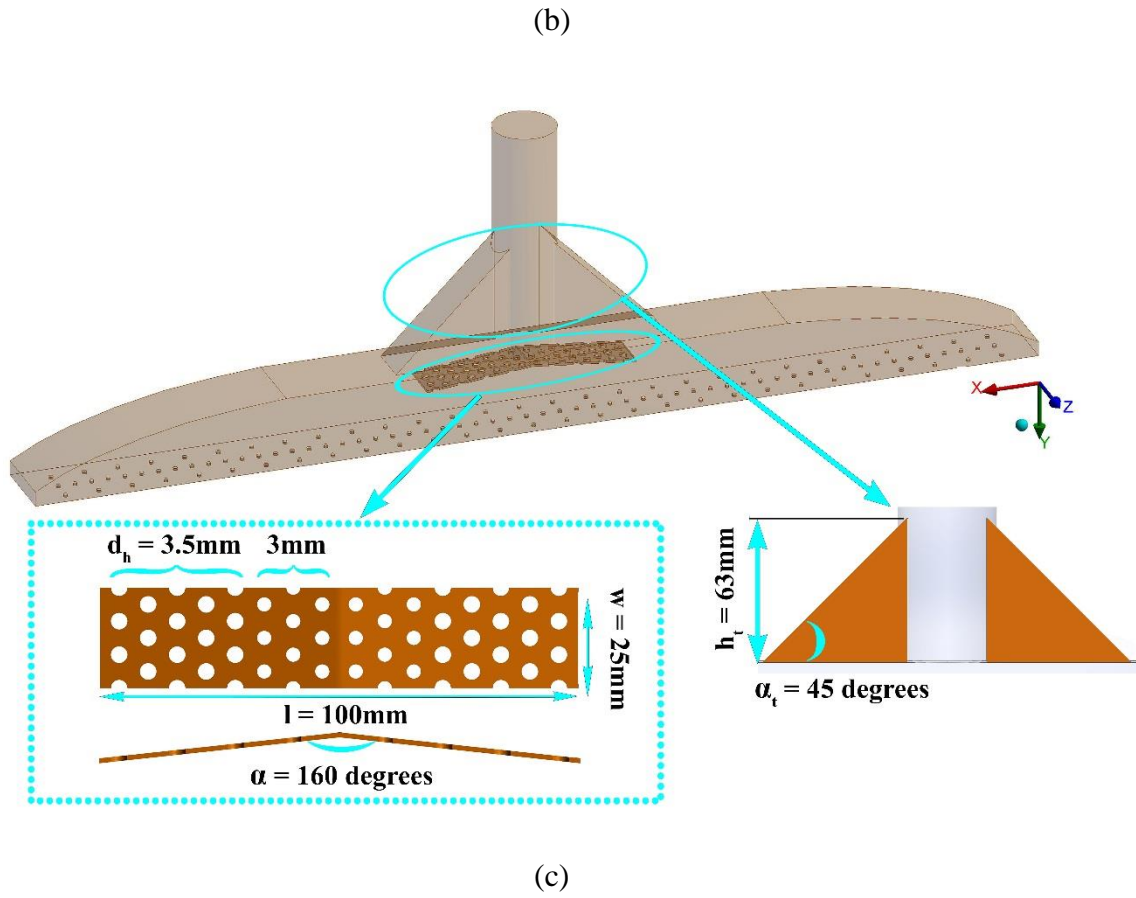


**Figure 2.3** The inner and outer shapes of three new gas torch models: (a) model 1; (b) model 2; (c) model 3

**Table 2.2.** The dimensions of inner and outer shapes of the three new models.

	Model 1	Model 2	Model 3
Guide vane holes diameters ( $d_h$ )	3 – 4.5 mm	3 mm	3 – 3.5 mm
Guide vane length ( $l$ )	480 mm	30 mm	100 mm
Guide vane width ( $w$ )	25 mm	25 mm	25 mm
Guide vane angle ( $\alpha$ )	160 degrees	160 degrees	160 degrees
Outer shape height ( $h_p, h_t$ )	-	63 mm	63 mm
Outer shape angle ( $\alpha_p, \alpha_t$ )	-	45 degrees	45 degrees
Y-branch pipes diameter ( $d_p$ )	-	15 mm	-

### 2.3 Numerical simulation

Steady-state numerical simulations were done using ANSYS FLUENT 18.2 software based on finite volume discretization. The boundary conditions and numerical method for the basic and modified gas torches are shown in Table 2.3. The standard k- $\epsilon$  turbulence model was used in this study. The SIMPLE algorithm was adopted for coupling the pressure and velocity in the simulation. For more accuracy, the second-order upwind scheme was selected for the spatial discretization. The convergence criterion was set up as  $10^{-4}$  for the momentum, continuity, and turbulence equations.

The numerical simulation was conducted to investigate the velocity profile inside and at the outlets of the gas torches. The meshes and boundary conditions of the basic model are shown in Figure 2.4. The inlet boundary condition was set as a pressure inlet of the fuel/air mixture. An ambient pressure outlet boundary condition was set at the outlet of the gas torch. A no-slip wall boundary condition was set for the other sides of the torch.

**Table 2.3** Boundary conditions and numerical method

Gauge pressure inlet	100Pa~500Pa
Gauge pressure outlet	0Pa
Walls	Non-slip wall
Turbulent model	Standard k- $\epsilon$
Convergence criterion	$10^{-4}$

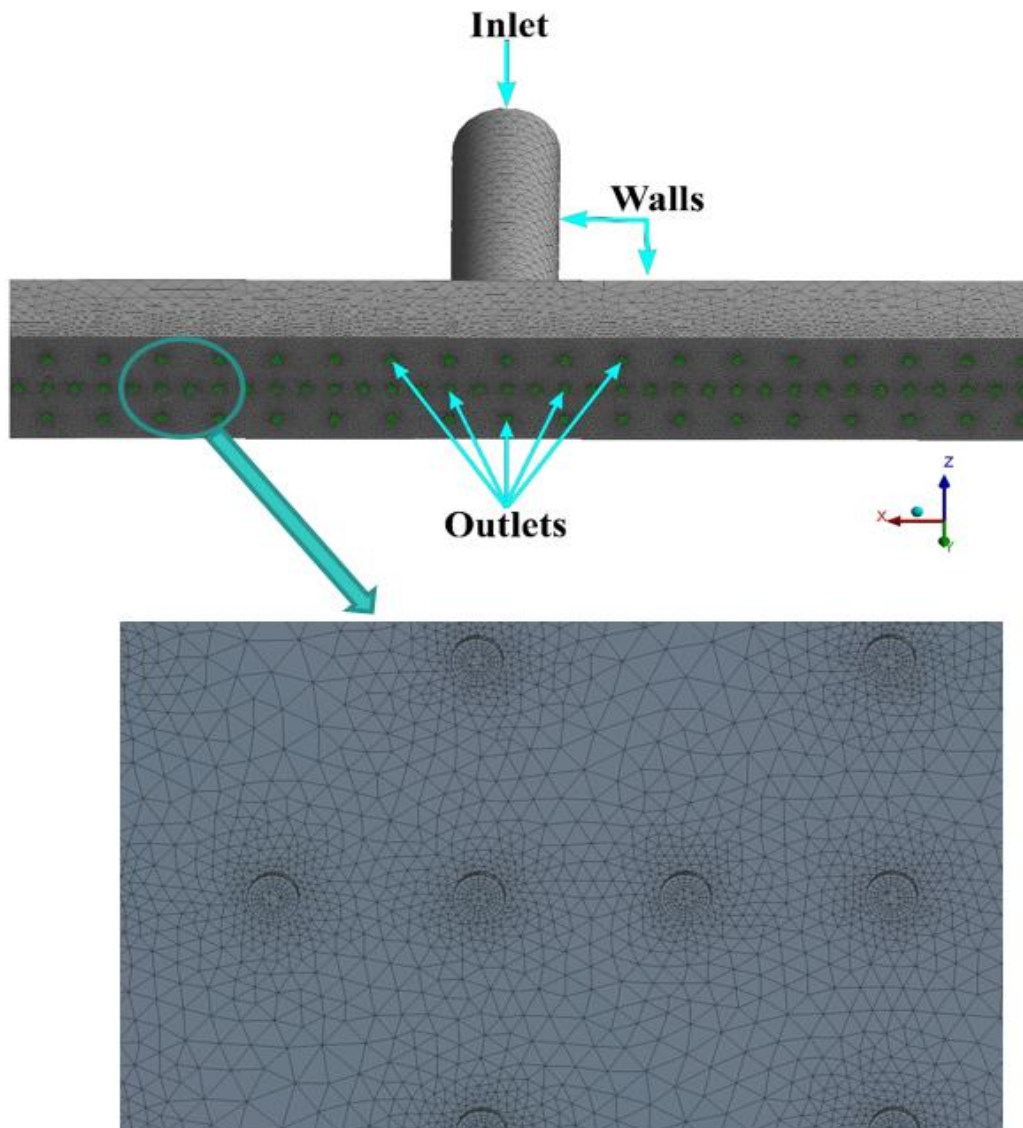


**Figure 2.4** Meshes and boundary conditions of a three-dimensional gas torch

The governing equations for the continuity, momentum, kinetic energy, and dissipation energy of the turbulence model [22] are the following:

Continuity equation:

$$\nabla \cdot (\rho \vec{u}) = 0 \quad (2.1)$$

Momentum equation:

$$\nabla \cdot (\rho \vec{u} \vec{u}) = -\nabla p + \nabla \cdot (\mu + \mu_t) \left[ \left( \nabla \vec{u} + \nabla \vec{u}^T \right) - \frac{2}{3} \nabla \cdot \vec{u} \mathbf{I} \right] \quad (2.2)$$

The turbulence kinetic energy  $k$  and the rate of its dissipation  $\varepsilon$  are obtained from the following transport equations:

$$\frac{\partial}{\partial x_i} (\rho k u_i) = \frac{\partial}{\partial x_j} \left[ \left( \mu + \frac{\mu_t}{\sigma_k} \right) \frac{\partial k}{\partial x_j} \right] + G_k - \rho \varepsilon \quad (2.3)$$

$$\frac{\partial}{\partial x_i} (\rho \varepsilon u_i) = \frac{\partial}{\partial x_j} \left[ \left( \mu + \frac{\mu_t}{\sigma_\varepsilon} \right) \frac{\partial \varepsilon}{\partial x_j} \right] + C_{1\varepsilon} \frac{\varepsilon}{k} G_k - C_{2\varepsilon} \rho \frac{\varepsilon^2}{k} \quad (2.4)$$

The turbulent viscosity is modeled as:

$$\mu_t = \rho C_\mu \frac{k^2}{\varepsilon} \quad (2.5)$$

The production of turbulence kinetic energy is defined as:

$$G_k = -\overline{\rho u'_i u'_j} \frac{\partial u_j}{\partial x_i} \quad (2.6)$$

$$-\overline{\rho u'_i u'_j} = \mu_t \left( \frac{\partial u_i}{\partial x_j} + \frac{\partial u_j}{\partial x_i} \right) - \frac{2}{3} \left( \rho k + \mu_t \frac{\partial u_k}{\partial x_k} \right) \delta_j \quad (2.6a)$$

The model constants  $C_{1\varepsilon}$ ,  $C_{2\varepsilon}$ ,  $C_\mu$ ,  $\sigma_k$ , and  $\sigma_\varepsilon$  have the following default values:  $C_{1\varepsilon} = 1.44$ ,  $C_{2\varepsilon} = 1.92$ ,  $C_\mu = 0.09$ ,  $\sigma_k = 1.0$ , and  $\sigma_\varepsilon = 1.3$ . Before investigating the velocity behavior of the gas torch, a grid-independence check was carried out by changing the amounts of elements to 583,137, 946,429, and 1,200,767, as shown in Figure 2.5. To reduce the computation time, 946,429 elements were selected as the amount to simulate the gas torch fluid domain.

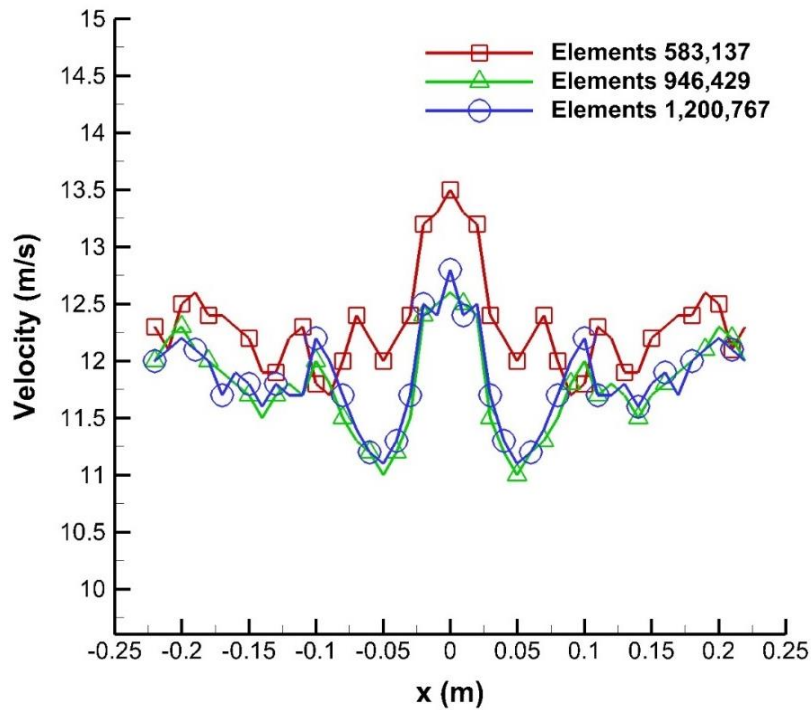
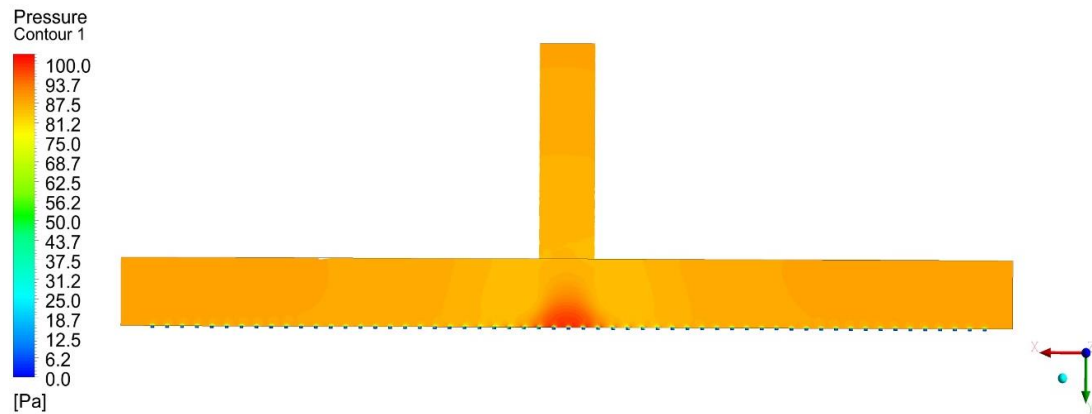


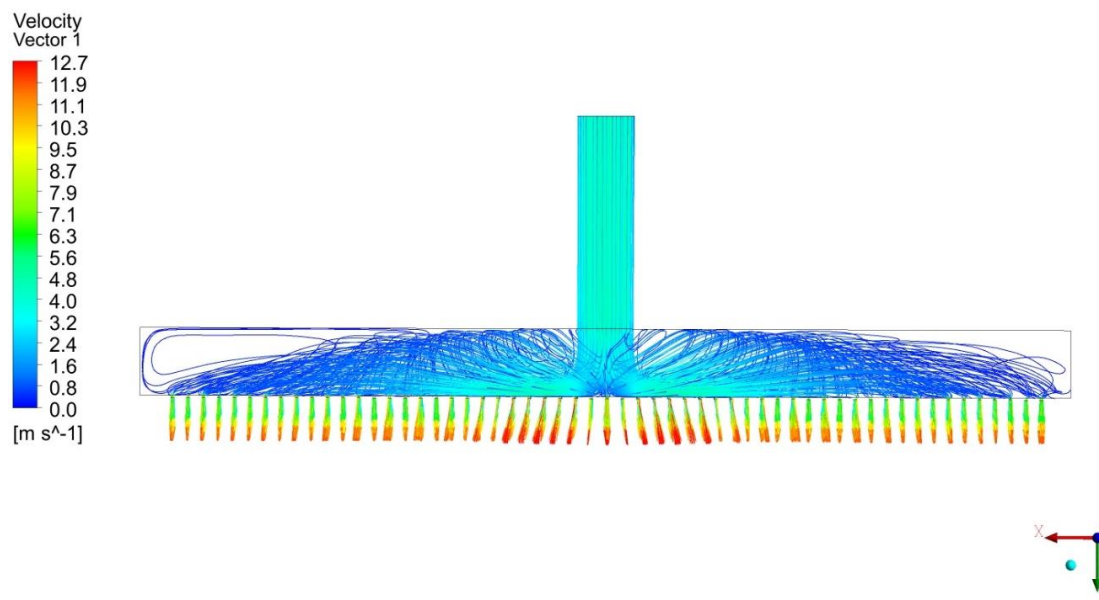
**Figure 2.5** Grid-independence check for velocity at the outlets along the lengthwise (x) direction

## 2.4 Results and discussion

Figure 2.6(a) shows the pressure contours at the mid-plane, and Figure 2.6(b) shows the streamlines and velocity vectors of the basic gas torch. The flow tends to concentrate in the center region, and two corner sides of the gas torch have very low velocity. Hence, the exit velocity is high in the center region and low in the right and left side regions, as shown in Figure 2.6(b). Consequently, the flow distribution at the outlet was non-uniform. The  $Y^+$  value of 4.78 in this case at the standard  $k-\epsilon$  turbulent model with standard wall functions was obtained.



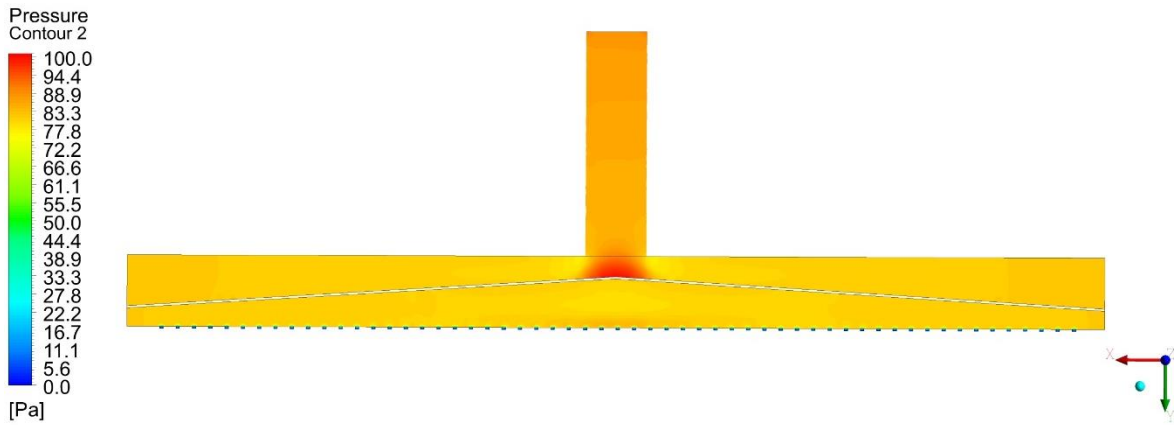
(a)



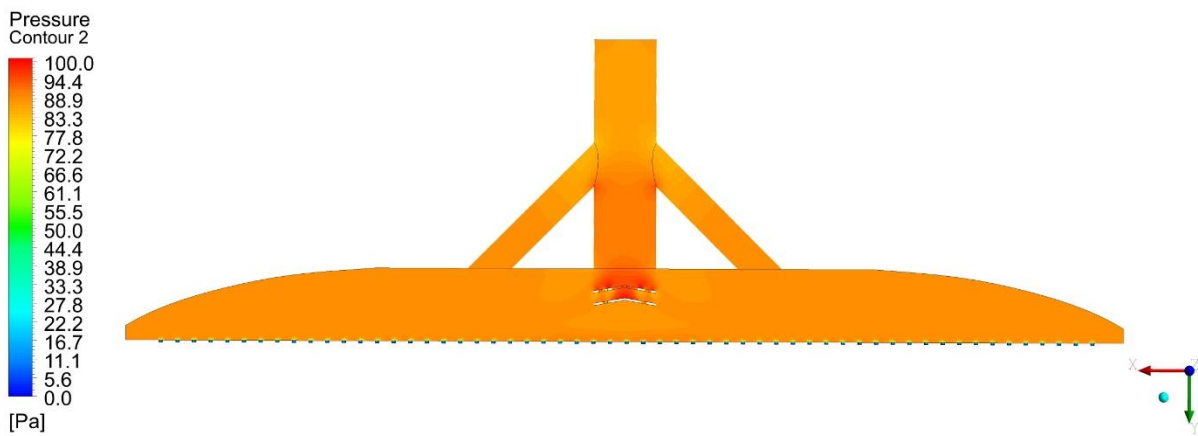
(b)

**Figure 2.6** (a) Pressure contour of the basic gas torch, (b) Inside streamline and velocity vector at the outlet

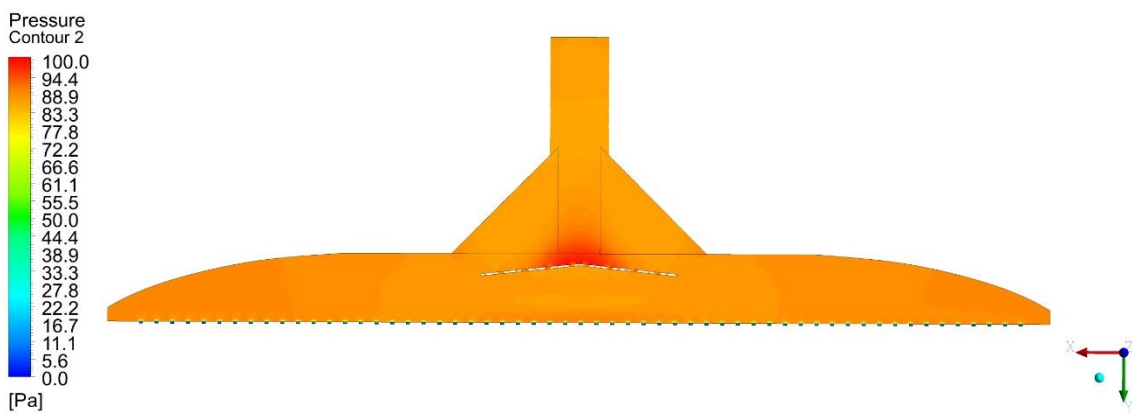
Figure 2.7 shows the pressure contours at the mid-plane of the three new models. Due to the flow impinging on the guide vanes at the center of the three modified models, the highest pressure is observed at the top on the guide vanes. The pressure then decreases as the central flow spreads towards the right and left side regions. Compared with the basic model, all three new models have uniform pressure at the outlets of the gas torches. This leads to enhanced uniformity of the flow velocity at the outlet.



(a)



(b)



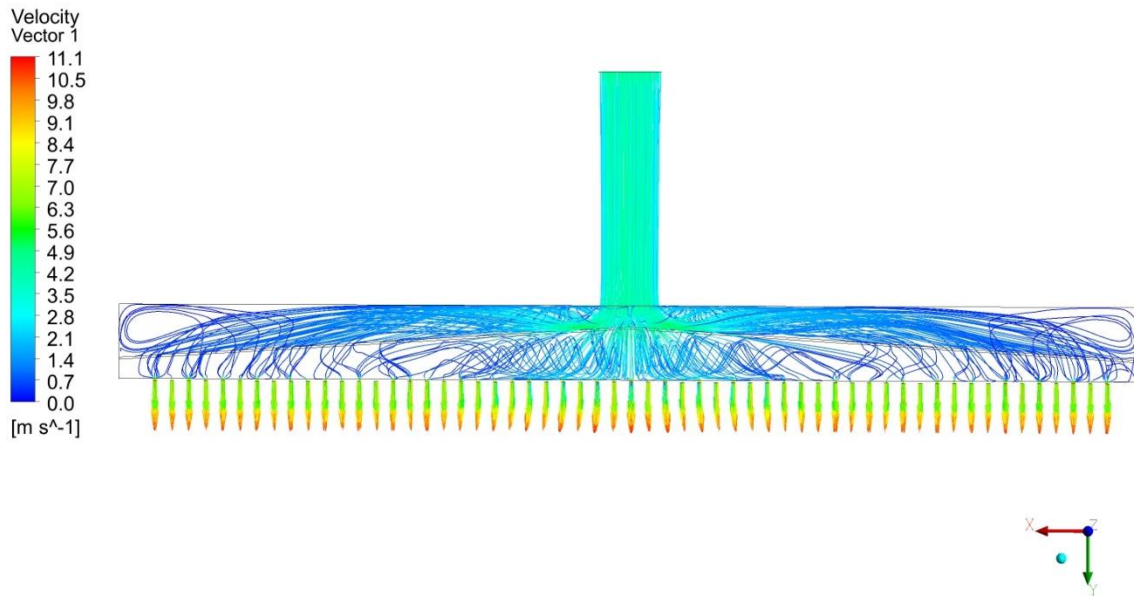
(c)

**Figure 2.7** Pressure contours at the middle plane of the three new gas torches:  
(a) model 1; (b) model 2; (c) model 3

The inner streamlines and velocity vectors at the outlets of the three new gas torches are shown in Figure 2.8. The highest velocity of all three models was around 11.1 m/s, which is less than velocity of 12.7 m/s of the basic model. In model 1, with a long perforated plate, one part of the flow passes through the perforated plate directly, and the rest spreads to the two sides. In model 2, the main flow goes through the diffuser with many holes, and the two split flows go through the two smaller pipes to produce uniform exit flow.

Model 3 was expected to operate with combined characteristics of model 1 and model 2 because it has combined structures from the inner strip from model 1 and the enlarged inlet and corner cuts at both sides from model 2. It is clear that there is a uniform velocity distribution at the outlets of the three new models. In these cases, the high velocity at the center was reduced, and the two side velocities were increased. Thus, the velocity uniformity along the x-direction was remarkably improved.

The physical mechanism of enhancing the flow uniformity for the three modified models was that the high velocity at the center of gas torch could be reduced by inserting the new designed inner and outer structures. Moreover, the two vortices at two sides of the basic gas torch could be also avoided.



(a)

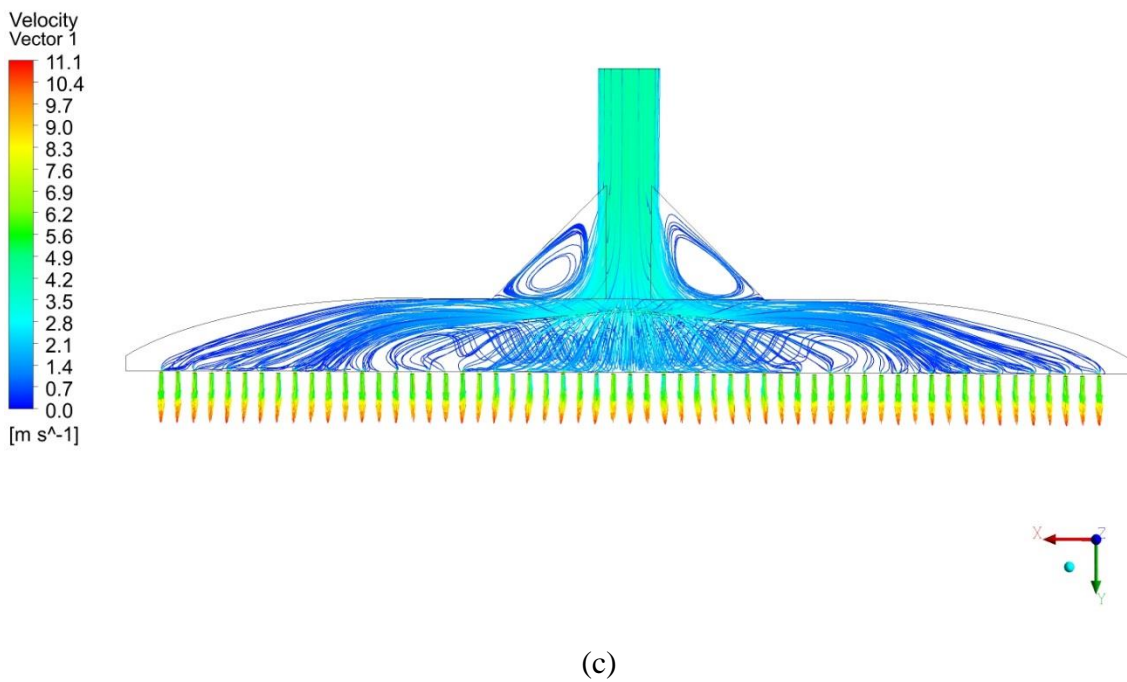
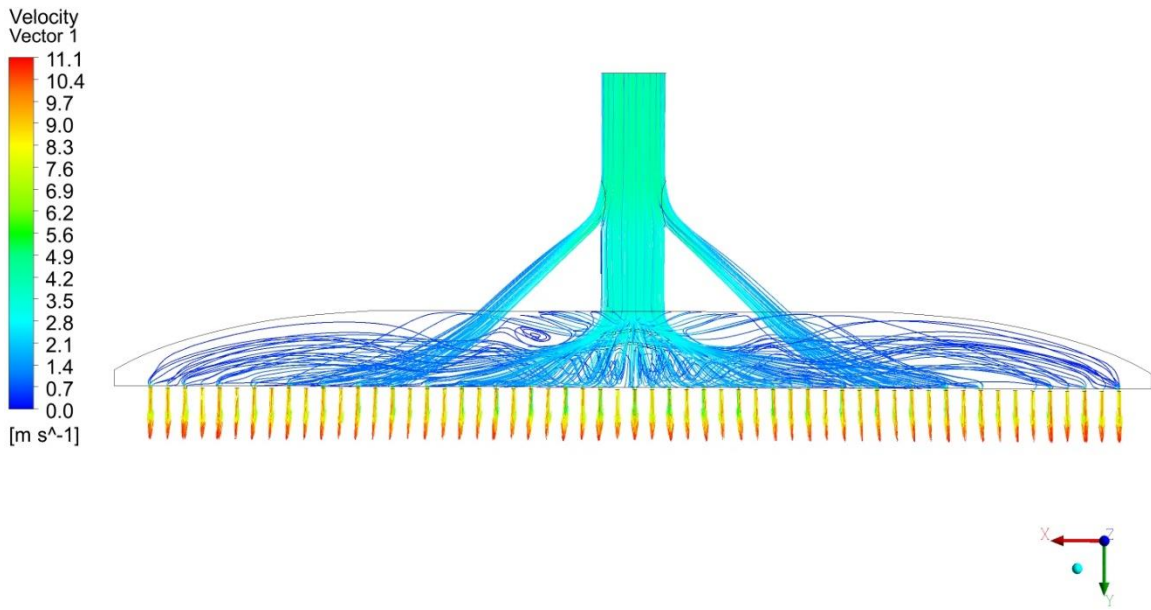


**Figure 2.8** Inner streamlines and velocity vectors at the outlet of the three new gas torches: (a) model 1; (b) model 2; (c) model 3

The exit velocity distribution along the lengthwise  $x$ -direction of the basic torch and new torches is shown in Figure 2.9. The flow velocity from the left side to the right

side of the basic gas torch is around 11 to 12.7 m/s. The highest velocity is concentrated in the center region of the torch. Therefore, the flow distribution at the outlet of the basic torch is non-uniform. All three modified models had similar shapes of the velocity distribution from the left to the right of the torch. By modifying the inner and outer shapes of the torches, the flow field distribution along the x-direction became uniform from the left to the right side. This a uniform flow at the outlets of the torches leads to a uniform temperature distribution of the steel plate during the preheating process.

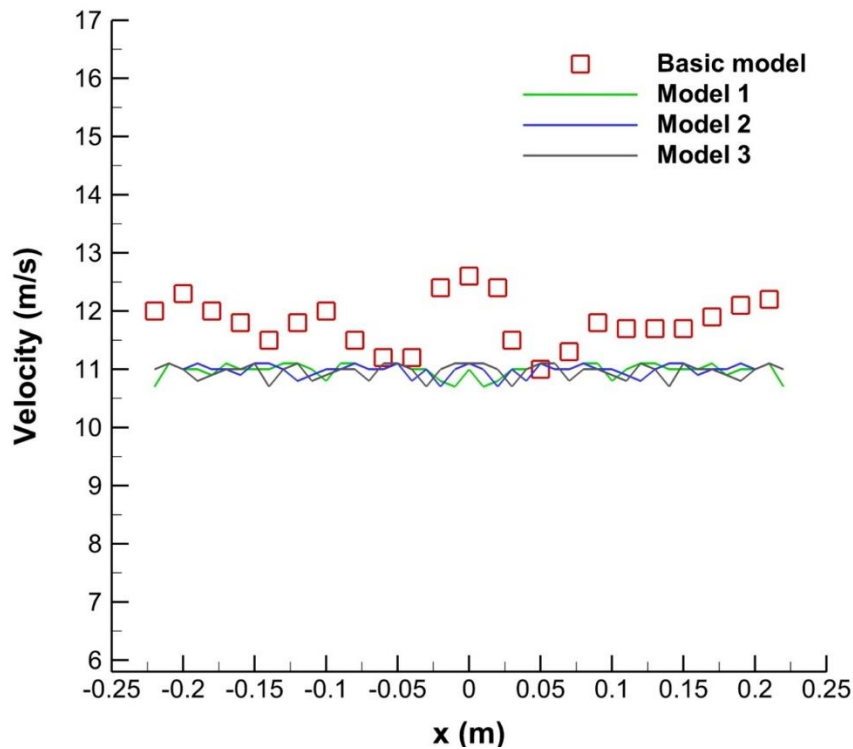


**Figure 2.9** Exit velocity distribution along the lengthwise direction of the basic and three new gas torches

To evaluate the uniformity of the flow fields at the outlet of the torches, the velocity uniformity index was utilized as follows:

$$\gamma = 1 - \frac{\sum_{m=1}^n (|u_m - \bar{u}_a| A_m)}{2|\bar{u}_a| \sum_{m=1}^n A_m} \quad (2.7)$$

Where,

$$\overline{u_a} = \frac{\sum_{m=1}^n u_m A_m}{\sum_{m=1}^n A_m} \quad (2.8)$$

Here,  $\gamma$  is the velocity uniformity index, and  $n$  is the total number of outlet positions.

$u_m$  is the velocity at the  $m$ <sup>th</sup> position, and  $\overline{u_a}$  is the mean of all the velocities. The value of  $\gamma = 1$  indicates a perfectly uniform distribution [22]. Figure 2.10 shows a comparison of the velocity uniformity index at the outlets between the basic torch and the three new torches as a function of the pressure drop. The velocity uniformity of the basic model was the lowest and ranged from 0.849 to 0.852. However, the three new models had high values of  $\gamma_1 = 0.901 - 0.912$ ,  $\gamma_2 = 0.902 - 0.911$ , and  $\gamma_3 = 0.901 - 0.914$ . The maximum percentage increase in the uniformity index between the three new models and the basic model was 7.3%. As the pressure drop increases, the velocity uniformity index of the three modified models increases.

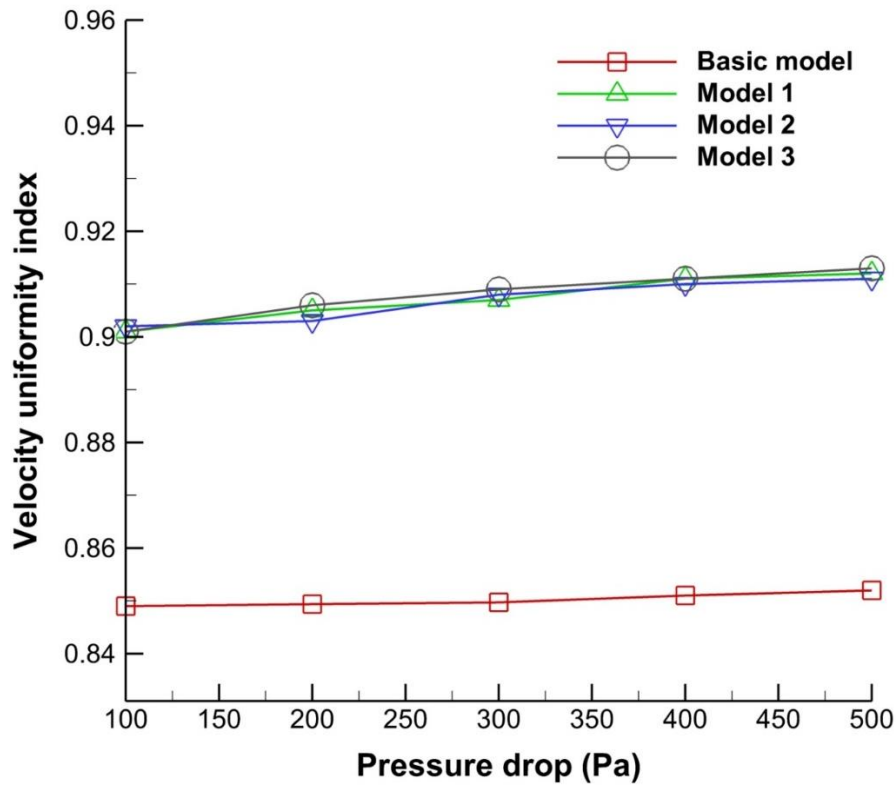


**Figure 2.10** Comparison of velocity uniformity index at the outlet between the basic torch and the three new gas torches as a function of pressure drop

## 2.5 Summary

The uniform flow distribution at the outlet of a gas torch and turbulent combustion for steel preheating were studied using ANSYS FLUENT 18.2 and experiments. The flow uniformity at the outlets of the torch was improved by the three new models. The velocity distribution at the outlets was also nearly uniform along the lengthwise direction, in contrast to with that of the basic model, and the velocity uniformity was better. The maximum percentage of the uniformity index between the three new models and basic model was 7.3%. With a trade-off between the capital cost of the new design and the operating cost to save fuel energy and obtain good quality for steel preheating, a suitable geometry for a gas torch can be selected for actual applications, particularly in preheating steel plates.

# Flame jet behavior from gas torches with multiple exit holes and the temperature distribution of a steel plate

## 3.1 System description of steel preheating process

Because the velocity uniformity at the outlet of gas torch was investigated in chapter 2, the numerical simulation and experimental combustion is carried out for the basic and modified models. An experiment was conducted to obtain validation for the numerical simulation results by ANSYS FLUENT 18.2 software. An experimental apparatus was designed for the basic and modified models in the steel preheating process, as shown in Figure 3.1. The uniformity of the three modified torches was nearly the same, as revealed in Figures 2.9 and 2.10, so model 3 was selected to carry out the experiment and compared with the basic model. The full steel plate has a width, length, and thickness of 0.8 m, 1.5 m, and 0.02 m, respectively. The distance between the outlets of the torch and the steel plate is 0.1 m.

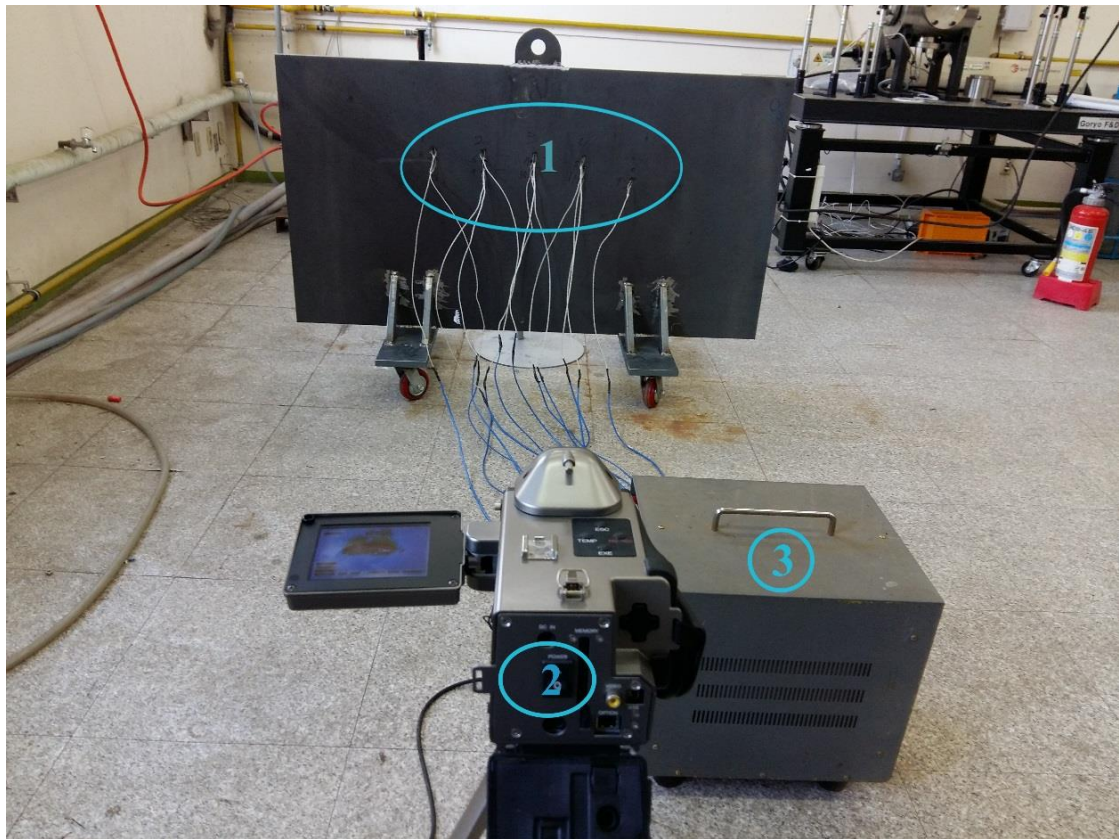
Figures 3.1(a) and (b) show that the LPG/air mixture is ignited to start the preheating processes after moving out of the basic and modified torches at the outlet. A TVS-200EX infrared camera is used to measure the temperature distribution on the back side of the steel plate, as shown in Figure 3.1(c). Since the camera image of the temperature distribution can cover a wide range of the heating region of the steel plate, temperatures measured by thermocouples are used as a reference.



(a)



(b)



(c)

**Figure 3.1** Experiment apparatus setup: (a) basic model; (b) Modified model; (c) TVS-200EX infrared camera and back side of the steel plate

### 3.2 Mathematic model

The governing equations include the continuity, momentum, energy, and species conservation equations, which were solved by ANSYS FLUENT 18.2. Multiple simultaneous chemical reactions can be modeled with reactions occurring in the bulk phase (volumetric reactions). To solve these conservation equations for chemical species, ANSYS FLUENT predicts the local mass fraction of each species,  $Y_i$ , through the solution of a convection and diffusion equation for the  $i_{th}$  species.

Continuity equation:

$$\frac{\partial \rho}{\partial t} + \nabla \cdot (\rho \vec{u}) = 0 \quad (3.1)$$

Momentum equation:

$$\frac{\partial(\rho \vec{u})}{\partial t} + \nabla \cdot (\rho \vec{u} \vec{u}) = -\nabla p + \nabla \cdot (\mu + \mu_t) \left[ \left( \nabla \vec{u} + \nabla \vec{u}^T \right) - \frac{2}{3} \nabla \cdot \vec{u} \vec{I} \right] \quad (3.2)$$

Energy equation:

$$\frac{\partial}{\partial t} (\rho E) + \nabla \cdot (\vec{u} (\rho E + p)) = \nabla \cdot \left( k \nabla T - \sum_j h_j \vec{J}_j + (\tilde{\tau} \cdot \vec{u}) \right) + S_h \quad (3.3)$$

Equation (3.3) shows the energy transfer in a control volume. The first term on the left-hand side represents the energy change in transient state. The second term on the left-hand side represents the energy transfer due to convection. Three terms on the right-hand side represent net energy transfer around control surface due to conduction heat transfer, species diffusion, and viscous dissipation. The last term represents source term including chemical reaction, radiation (DO radiation source term in this study), and so on.

For multi-component mixing flow, the transport of enthalpy due to species diffusion can have a significant effect on the enthalpy field and should not be neglected.

$$\nabla \cdot \left[ \sum_{i=1}^n h_i \vec{J}_i \right] \quad (3.4)$$

The turbulence kinetic energy  $k$  and the rate of its dissipation  $\varepsilon$  are obtained from the following transport equations:

$$\frac{\partial k}{\partial t} + \frac{\partial}{\partial x_i} (\rho k u_i) = \frac{\partial}{\partial x_j} \left[ \left( \mu + \frac{\mu_t}{\sigma_k} \right) \frac{\partial k}{\partial x_j} \right] + G_k - \rho \varepsilon \quad (3.5)$$

$$\frac{\partial \varepsilon}{\partial t} + \frac{\partial}{\partial x_i} (\rho \varepsilon u_i) = \frac{\partial}{\partial x_j} \left[ \left( \mu + \frac{\mu_t}{\sigma_\varepsilon} \right) \frac{\partial \varepsilon}{\partial x_j} \right] + C_{1\varepsilon} \frac{\varepsilon}{k} G_k - C_{2\varepsilon} \rho \frac{\varepsilon^2}{k} \quad (3.6)$$

Turbulent viscosity is modelled as:

$$\mu_t = \rho C_\mu \frac{k^2}{\varepsilon} \quad (3.7)$$

The production of turbulence kinetic energy is defined as:

$$G_k = -\overline{\rho u'_i u'_j} \frac{\partial u_j}{\partial x_i} \quad (3.8)$$

$$-\overline{\rho u'_i u'_j} = \mu_t \left( \frac{\partial u_i}{\partial x_j} + \frac{\partial u_j}{\partial x_i} \right) - \frac{2}{3} \left( \rho k + \mu_t \frac{\partial u_k}{\partial x_k} \right) \delta_{ij} \quad (3.8a)$$

The model constants  $C_{1\varepsilon}$ ,  $C_{2\varepsilon}$ ,  $C_\mu$ ,  $\sigma_k$  and  $\sigma_\varepsilon$  have the following default values  $C_{1\varepsilon} = 1.44$ ,  $C_{2\varepsilon} = 1.92$ ,  $C_\mu = 0.09$ ,  $\sigma_k = 1.0$ ,  $\sigma_\varepsilon = 1.3$ .

The species conservation equation:

$$\frac{\partial}{\partial t} (\rho Y_i) + \nabla \cdot (\rho \vec{u} Y_i) = -\nabla \cdot \vec{J}_i + R_i \quad (3.9)$$

where  $R_i$  is the net rate of production of species by chemical. In turbulent flows, the mass diffusion is computed as the following form:

$$J_i = - \left( \rho D_{i,m} + \frac{\mu_t}{Sc_t} \right) \nabla Y_i - D_{T,i} \frac{\nabla T}{T} \quad (3.10)$$

where  $Sc_t$  is the turbulent Schmidt number, and the default value is 0.7. It should be noted that turbulent diffusion generally overwhelms laminar diffusion, and the specification of detailed laminar diffusion properties in turbulent flows is generally not necessary. The turbulent-chemistry interaction model combines turbulent flow and complex chemical kinetics. Turbulence enhances the mixing of the reactants. The chemical reactions involve the temperature rise, change density, and affect the flow

itself. Therefore, the coupling between turbulence and chemical reactions plays a crucial role in turbulent reactive flows. ANSYS FLUENT provides a turbulence-chemistry interaction model called the eddy-dissipation model (EDM), which is based on the work of Magnussen and Hjertager. The net rate  $R_{i,r}$  of the production of species  $i$  due to reaction  $r$  is given by the smaller of the two equations below:

$$R_{i,r} = v'_{i,r} M_{w,i} A \rho \frac{\varepsilon}{k} \min \left( \frac{Y_R}{v'_{R,r} M_{w,R}} \right) \quad (3.11)$$

$$R_{i,r} = v'_{i,r} M_{w,i} A B \rho \frac{\varepsilon}{k} \frac{\sum_P Y_P}{\sum_j^N v''_{j,r} M_{w,j}} \quad (3.12)$$

where,

$v'_{i,r}$  is the stoichiometric coefficients for reactant  $i$  in reaction  $r$

$v''_{j,r}$  is the stoichiometric coefficients for product  $j$  in reaction  $r$

$M_w$  is the molecular weight (kg/kmol)

$k$  is the turbulence kinetic energy rate (J/kg)

$\varepsilon$  is the turbulent dissipation rate ( $m^2/s^3$ )

$Y_P$  is the mass fraction of product species, P

$Y_R$  is the mass fraction of a particular reactant, R

A is an empirical constant equal to 4.0

B is an empirical constant equal to 0.5

The reaction rates are assumed to be controlled by the turbulence hence the Arrhenius chemical kinetic calculations can be neglected.

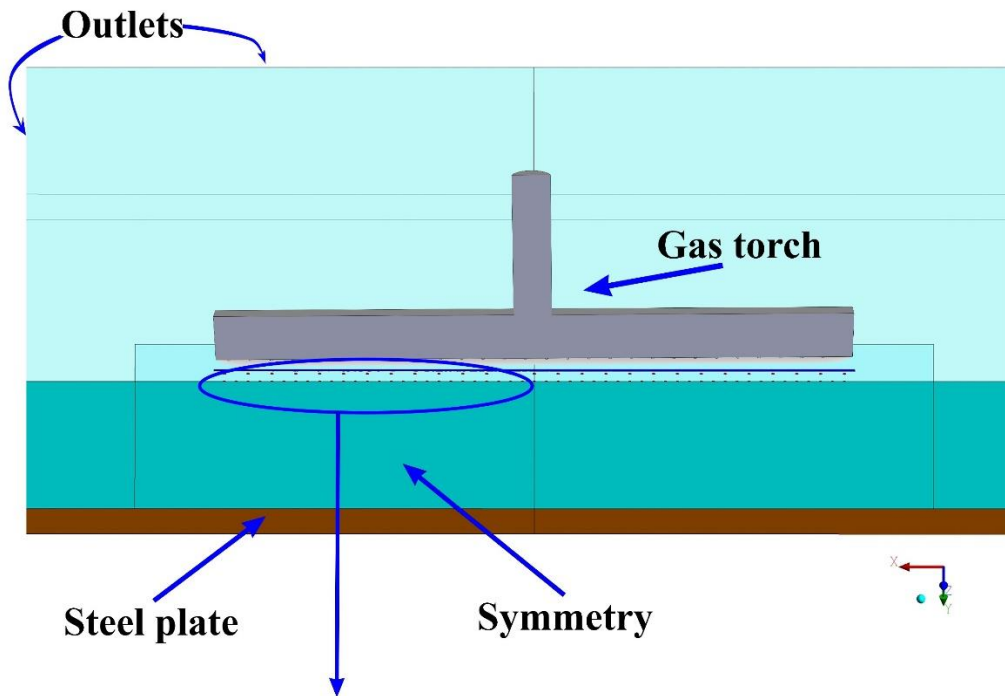
The Reynolds number is calculated based on cold LPG/air mixture gases

$$\text{Re} = \frac{\rho_{\text{mix}} v_{\text{mix}} d}{\mu_{\text{mix}}} \quad (3.13)$$

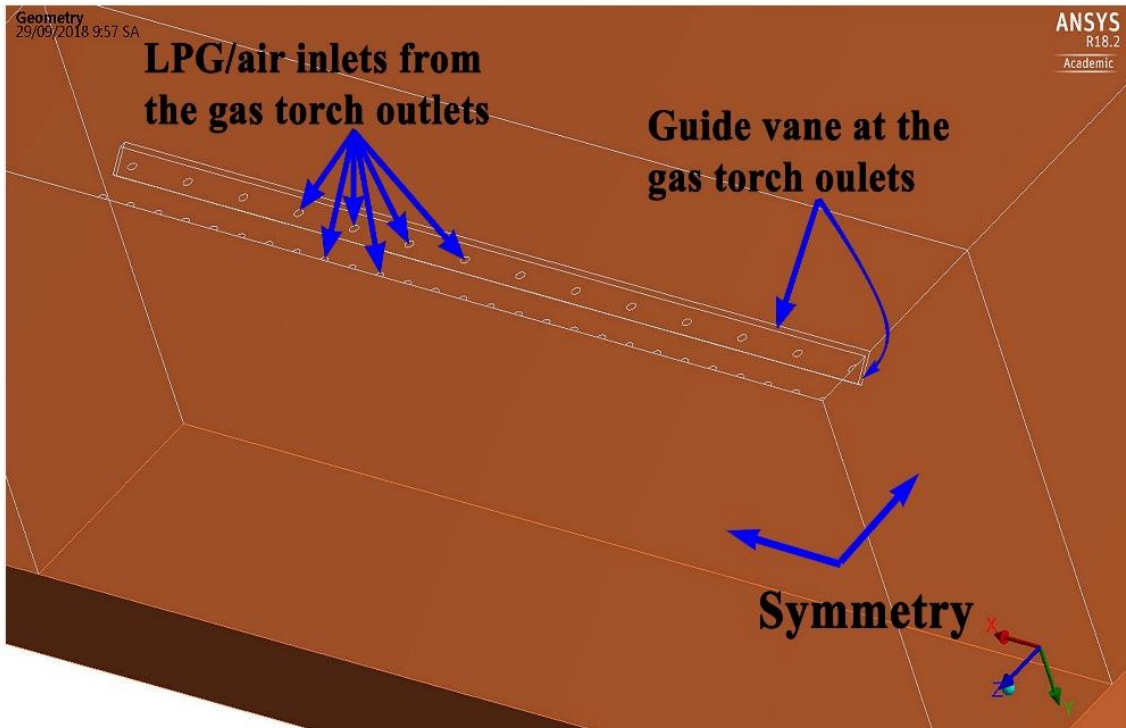
The equivalence ratio is defined as follows:

$$\phi = \frac{(\text{Fuel/ Air})_{\text{actual}}}{(\text{Fuel/ Air})_{\text{stoic}}} \quad (3.14)$$

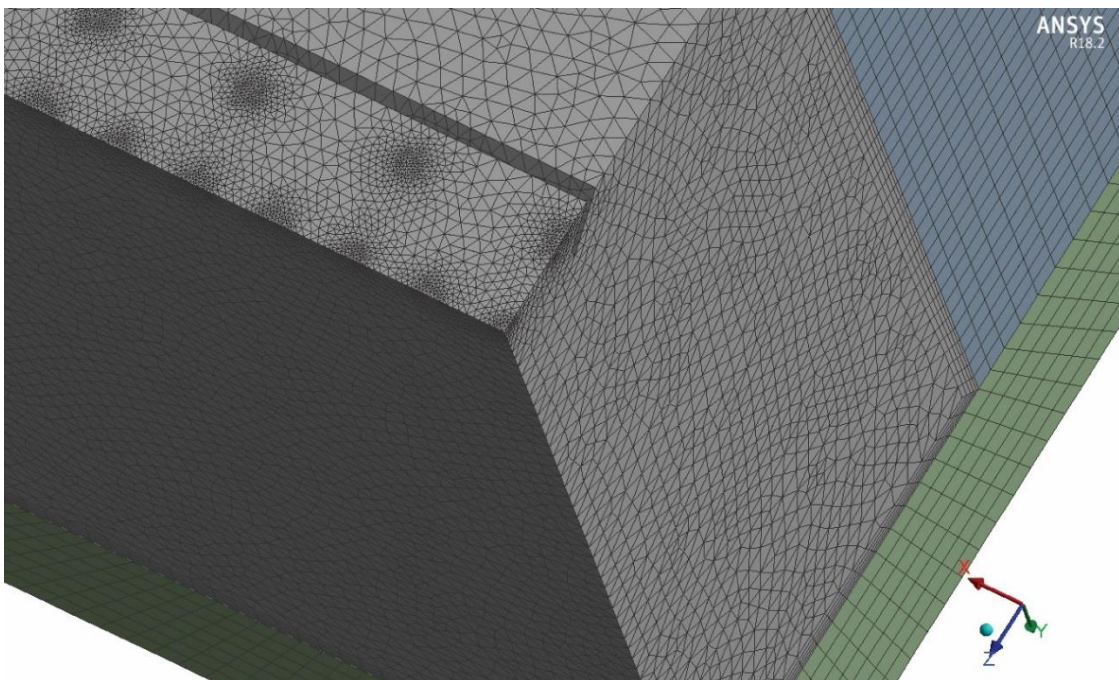
### 3.2.1 Boundary condition and numerical simulation



(a)



(b)



(c)

**Figure 3.2** Schematic diagram of steel preheating process with gas torch, fluid domain, and steel plate; (a) A half model (x-y plane cut view); (b) Three-dimensional magnified view of the quarter model; (c) Mesh model of the quarter model

The quarter part of computational domain from the gas torch outlet to the steel plate is shown in Figure 3.2(a). The boundary conditions and numerical simulation method are shown in Figure 3.2 and Table 3.1. Due to the symmetry of the full model, a quarter of the model is used for the simulation to reduce the computation time is shown in Figure 3.2(b). Symmetric boundary conditions are selected at the two inner surfaces for both the fluid and steel domain. The two outer faces are set to the pressure outlet boundary conditions. The velocity boundary conditions of the jet holes are used for the LPG/air inlet. The other top surfaces except at the LPG/air inlet are treated as ambient air inlets. No-slip conditions are selected for the wall boundary conditions imposed on the impinging jet.

The high flame temperature during the combustion process is associated with radiation heat transfer to the environment, which are considered significant [69,70]. The discrete ordinates (DO) radiation model is used to examine the effect of radiation. The DO model covers the entire range of optical thickness and can solve problems ranging from surface-to-surface radiation to the radiation in combustion problems. The boundary conditions for the DO radiation model are selected by default in ANSYS FLUENT 18.2 [22]. The absorption coefficient is modeled using the weighted sum of gray gases model (WSGGM). The DO equation has the following form:

$$\nabla \cdot (I(\vec{r}, \vec{s}) \vec{s}) + (a + \sigma_s) I(\vec{r}, \vec{s}) = an^2 \frac{\sigma T^4}{\pi} + \frac{\sigma_s}{4\pi} \int_0^{4\pi} I(\vec{r}, \vec{s}') \phi(\vec{s}, \vec{s}') d\Omega' \quad (3.15)$$

where:

$\vec{r}$  is the position vector

$\vec{s}$  is the direction vector

$\vec{s}'$  is the scattering direction vector

$a$  is the absorption coefficient

$n$  is the refractive index

$\sigma_s$  is the scattering coefficient

$\sigma$  is the Stefan–Boltzmann constant ( $5.669 \times 10^{-8} \text{ W.m}^{-2}.\text{K}^{-4}$ )

$I$  is the radiation intensity

$T$  is the local temperature

$\phi$  is the phase function

$\Omega'$  is the solid angle

Equation (3.15) shows that the net radiation intensity around a control volume (the first term on the left-hand side) is equal to the sum of the extinction (the second term on the left-hand side), emission (the first term on the right-hand side), and the scattering term (the second term on the right-hand side).

**Table 3.1.** Boundary condition and numerical simulation method.

<b>Parameters/method</b>	<b>Value/range</b>	<b>Numerical simulation method</b>
LPG/air mixture velocity inlet	17 – 35 m/s	-
Outlet	0 Pa	-
Wall	No-slip	-
Process time	30 minutes	-
Equivalent ratios	0.8 - 1.2	-
Reynolds number	2,368 – 4,876	-
Burner to plate distance to nozzle diameter ratio	25 - 75	-

Turbulent model	-	Standard k-ε
Combustion model	-	Eddy dissipation model (EDM)

---

The transient and steady-state numerical simulations were performed using ANSYS FLUENT based on finite volume discretization. Double precision was used to improve the accuracy of the results. For more accuracy, the second-order upwind scheme was selected for the discretization of non-linear equations such as the mass, momentum, energy, and species transport equations. The SIMPLE algorithm is adopted for coupling the pressure and velocity. A convergence criterion of  $10^{-4}$  is set for the momentum, continuity, turbulence, and species equations, and  $10^{-6}$  is used for the energy equation.

### **3.2.2 Grid independence check**

The grid independence of the solution was checked for three numbers of elements: 808,045, 1,829,319, and 3,792,625. The temperature distribution is plotted as a function of the y-directional distance between the gas torch and the steel plate in Figure 3.3. The medium and largest members of elements showed similar trends. In contrast to these two cases, the temperature distribution with the fewest elements presented a larger difference. Therefore, to save calculation time for the simulation, the medium number of 1,829,319 was employed.

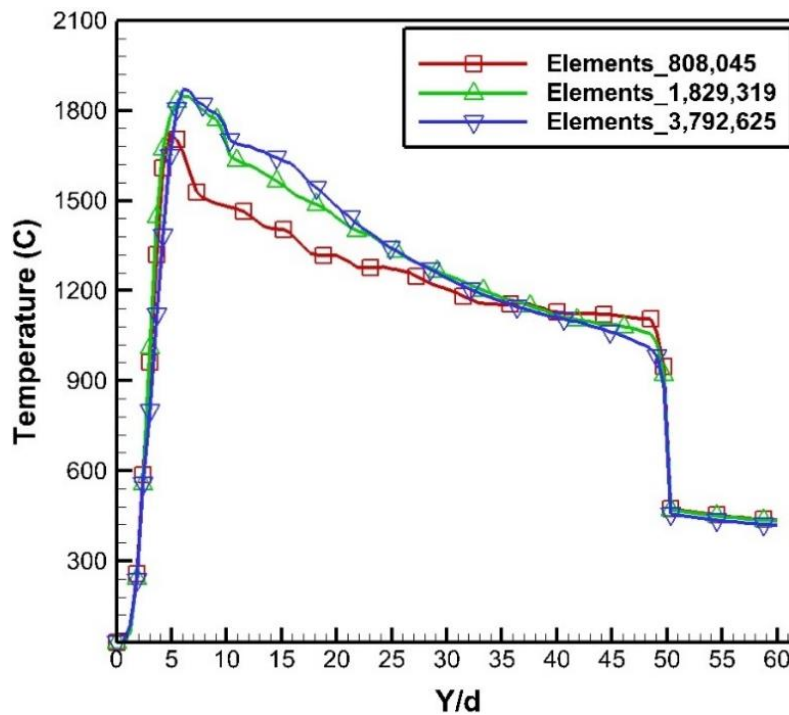


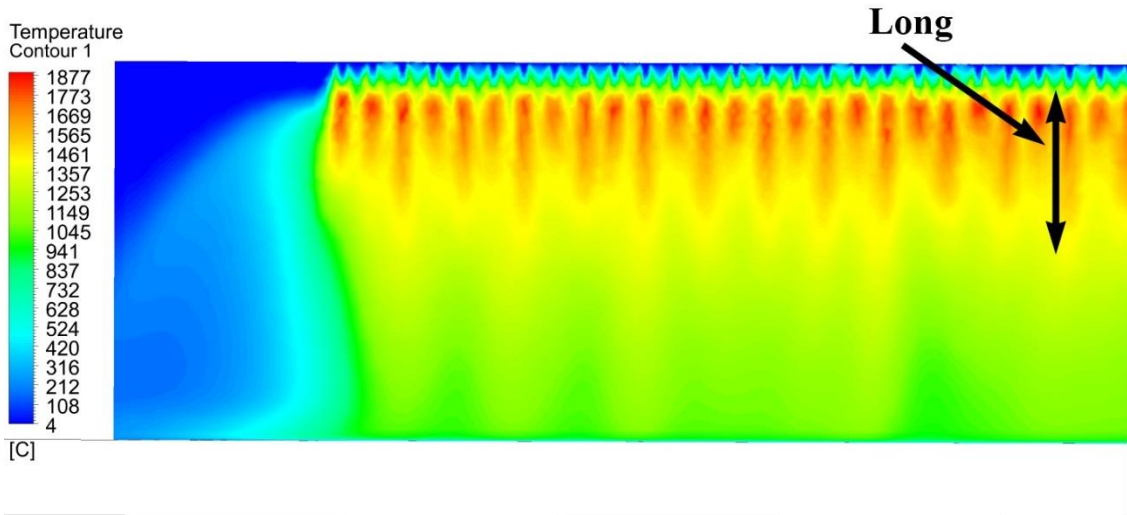
**Figure 3.3** Grid independence check with increasing elements

### **3.3 Comparison of the temperature distribution at the back side of a steel plate between the experiment and simulation**

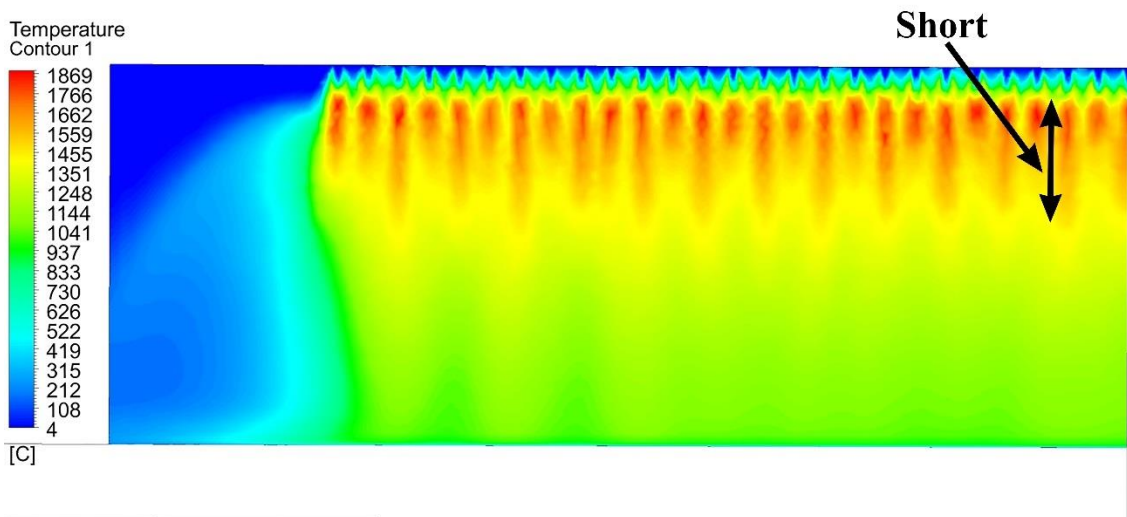
Due to the uniform flow and almost the same velocity magnitude at the outlets of the modified torches in chapter 2, model 3 was selected to carry out the simulation and experiment and then compared with the basic model. Figure 3.4 shows the temperature contour of a combustion flame zone at the center line view in the steel preheating zone for the basic and modified model with an LPG/air mixture as a fuel.

The highest temperature for the basic model approaches 1877°C at an equivalence ratio ( $\Phi$ ) of 1.0 and steel-plate distance of 0.1 m. This temperature is slightly higher than that of 1869°C for the modified model. This is due to the fact that higher flame temperature in a narrow center region can be obtained from a higher Reynolds number. Thus, the basic model has a longer flame structure near the center region than the modified model. The ambient air near the jet holes is entrained to the flame zone due to the high-speed jet stream. The entrained air also participates in the

combustion process. The primary jet line at the center line of the torch is associated with the main combustion process, and the combustion flame of the primary jet lines makes a major contribution to the steel-plate heating.



(a)



(b)



**Figure 3.4.** The temperature contours of a combustion flame zone at the center-line view during the steel-plate preheating process: (a) Basic model; (b) Modified model

Figure 3.5 shows the species mole fraction and temperature variations of the stoichiometric of the LPG/air mixture as a function of the jet flow direction at the center region for the basic model and modified model. For the basic model, before the combustion happens, the mole fractions of  $C_3H_8$ ,  $C_4H_{10}$ , and  $O_2$  are approximately 0.01, 0.02, and 0.2, respectively. The temperature of the unburned mixture is  $27^\circ C$  (300K). After the combustion happens, the reactant mole fractions decrease quickly, and then  $CO_2$  and  $H_2O$  are generated. Thus, the products and their mole fractions increase quickly. The flame temperature increases very fast in a short distance when the combustion happens.

For the modified model, because of the smaller Reynolds number than the basic model, the turbulent combustion has higher temperature and higher product mole fractions in all positions except the starting position ( $Y = 0$  mm) and the last position ( $Y = 12$  mm) than the basic model case.

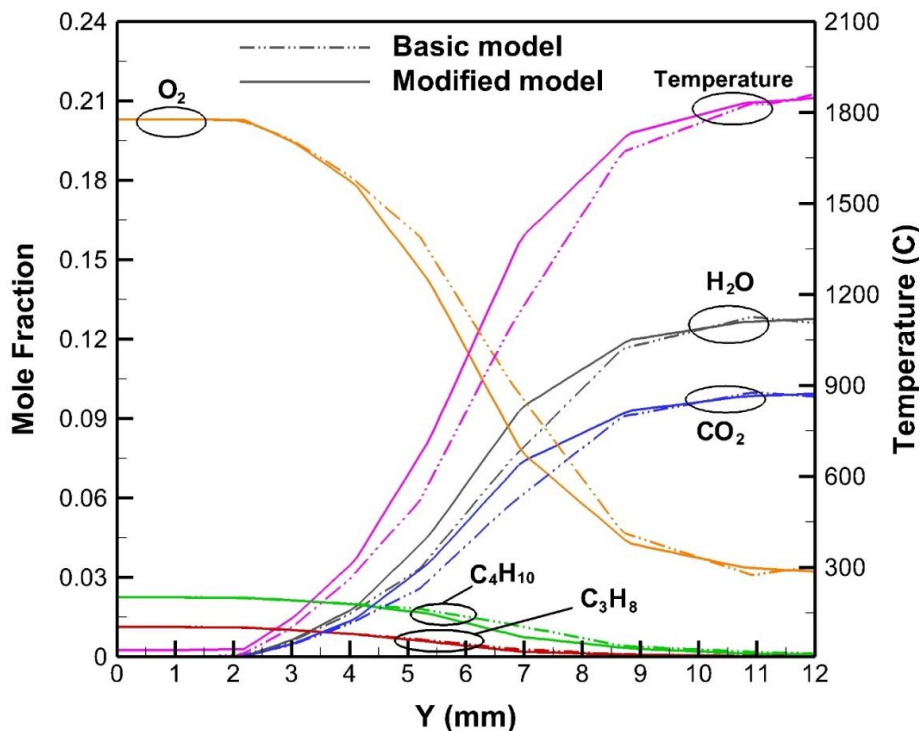
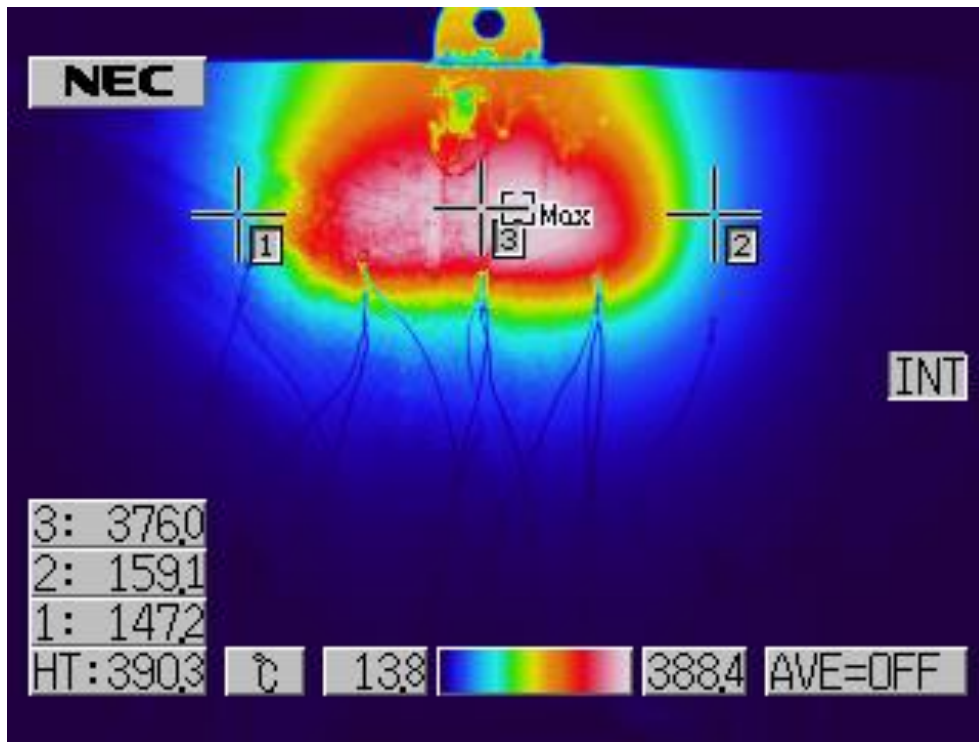


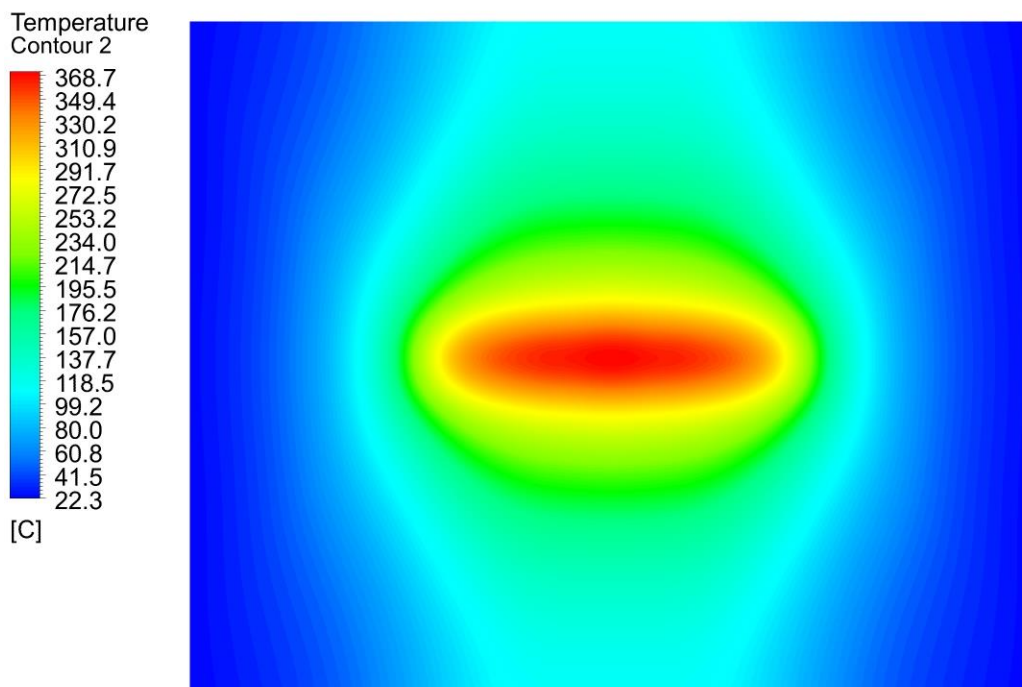
**Figure 3.5.** The species mole fraction and temperature variations of the stoichiometric LPG/air mixture for the basic model and modified model.

The experiment and simulation results for the basic and modified models are shown in Figure 3.6 and Figure 3.7. In the basic model in Figure 3.6(a), most of the high-temperature region is concentrated in the center region because the non-uniform flow at the center region of the torch causes high temperature in this region. Consequently, the temperature difference between the center and the edge is large (about 229°C). However, in the modified model in Figure 3.6(c), the temperature difference between the center and the edge is much smaller (about 90°C) due to the uniform flow distribution at the torch outlets.

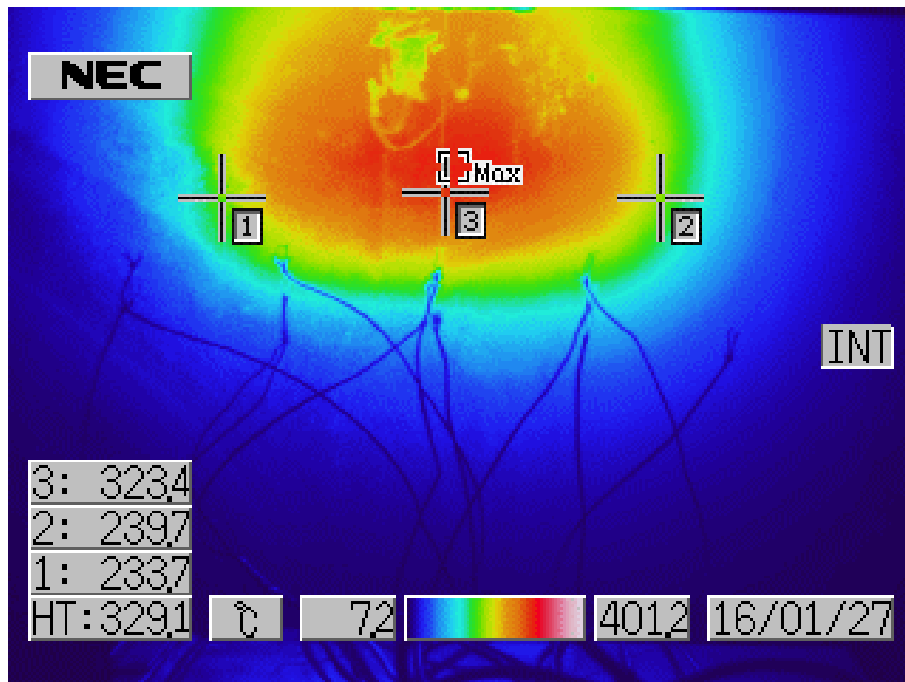
The temperature distributions at the back side of the steel plate from the numerical simulation (Figures 3.6(b) and 3.6(d)) showed good agreement with those from the experiment (Figures 3.6(a) and 3.6(c)). In the complete combustion, as shown in Figure 3.7, the temperature distribution on the steel plate is higher than that in the incomplete combustion because the fuel is completely burned in complete combustion and it releases the maximum amount of energy. The modified model (Figure 3.7(c)) shows a wider and more uniform temperature region than the basic model (Figure 3.7(a)) due to the uniform flow at the outlet of the torch. The simulation results (Figures 3.7(b) and 3.7(d)) also have good agreement with the experimental ones (Figures 3.7(a) and 3.7(c)) for both the basic model and the modified model



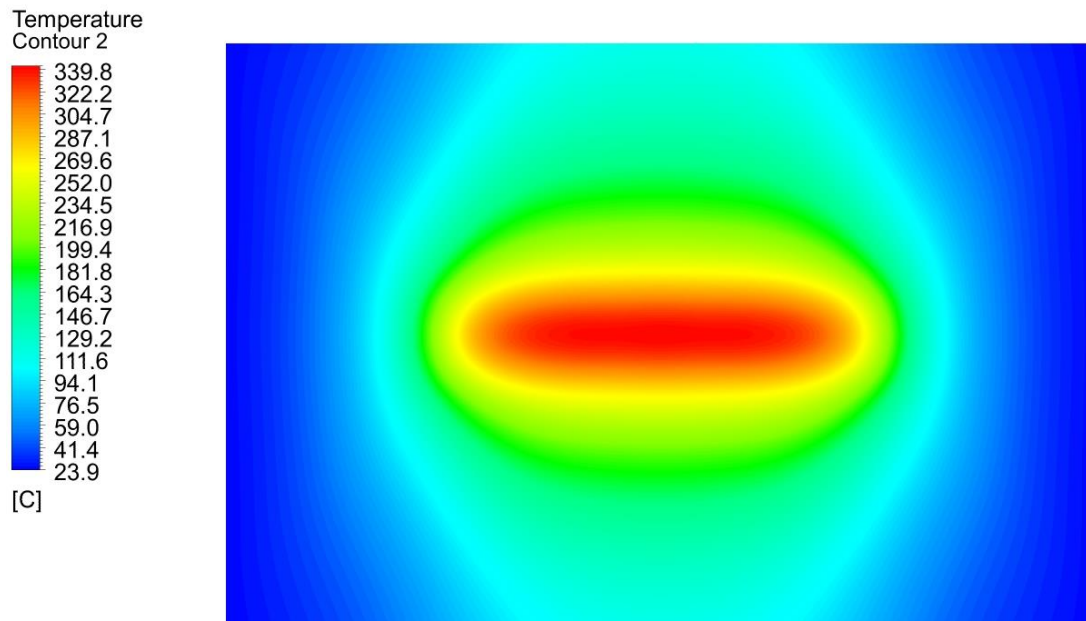
(a)



(b)

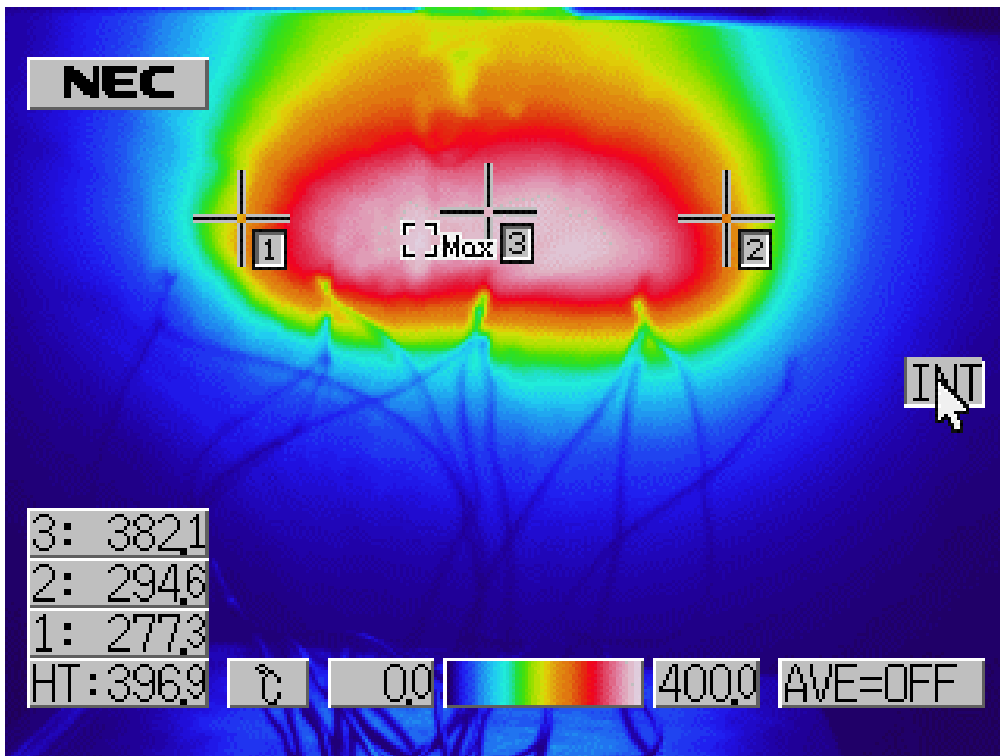


(c)



(d)

**Figure 3.6** Steel plate temperature distribution at the back-side with the incomplete combustion  $\Phi = 1.4$ : (a) Basic model experiment; (b) Basic model simulation; (c) Modified model experiment; (d) Modified model simulation.

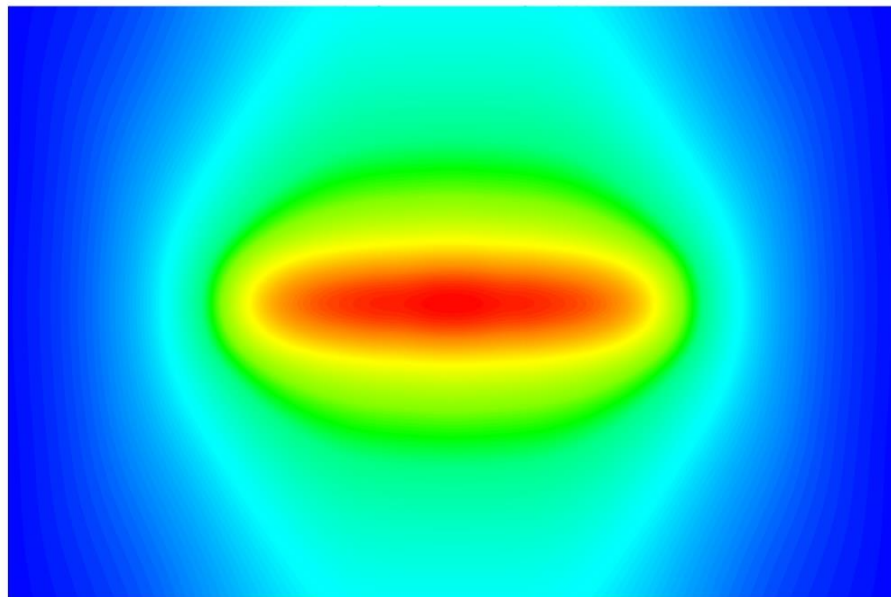


(a)

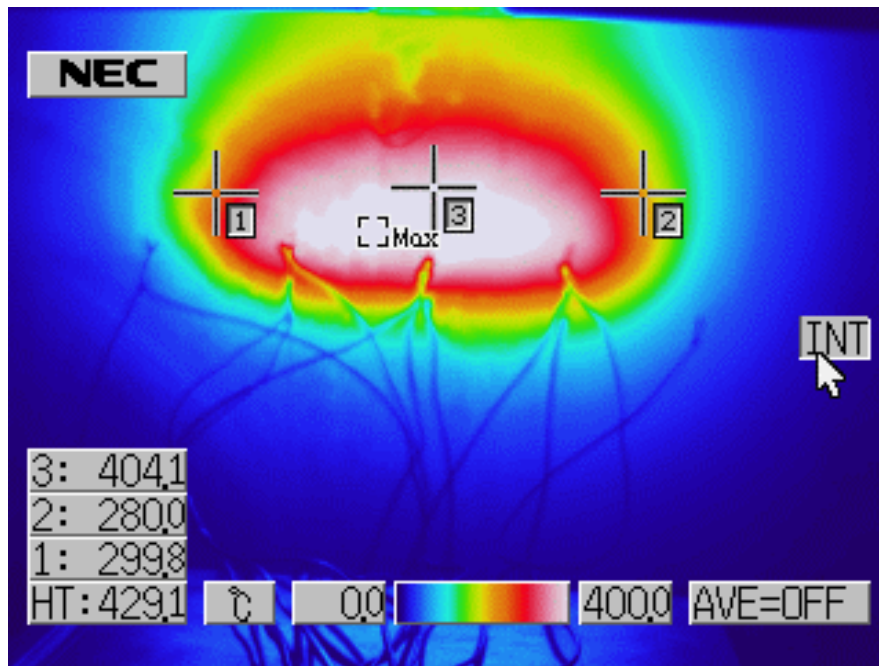
Temperature  
Contour 2



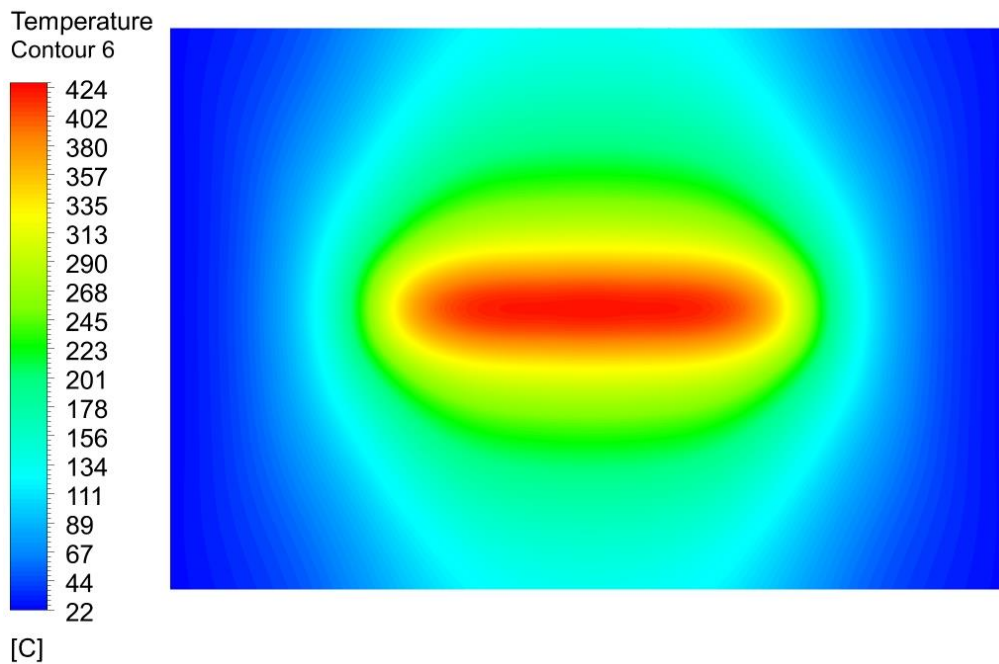
[C]



(b)



(c)



(d)

**Figure 3.7** Steel plate temperature distribution at the backside with the complete combustion  $\Phi = 1.0$ : (a) Basic model experiment; (b) Basic model simulation; (c) Modified model experiment; (d) Modified model simulation.

Figure 3.8 shows the temperature uniformity index at the backside steel plate for the basic and modified models. Due to high uniform flow at the outlet of gas torch, the modified gas torch model showed higher uniform temperature on the backside steel plate for both complete and incomplete combustion conditions than the basic gas torch model. The temperature uniformity indices of around 0.9 for the modified model were higher than those of around 0.85 for the basic model as shown in Figure 3.8.

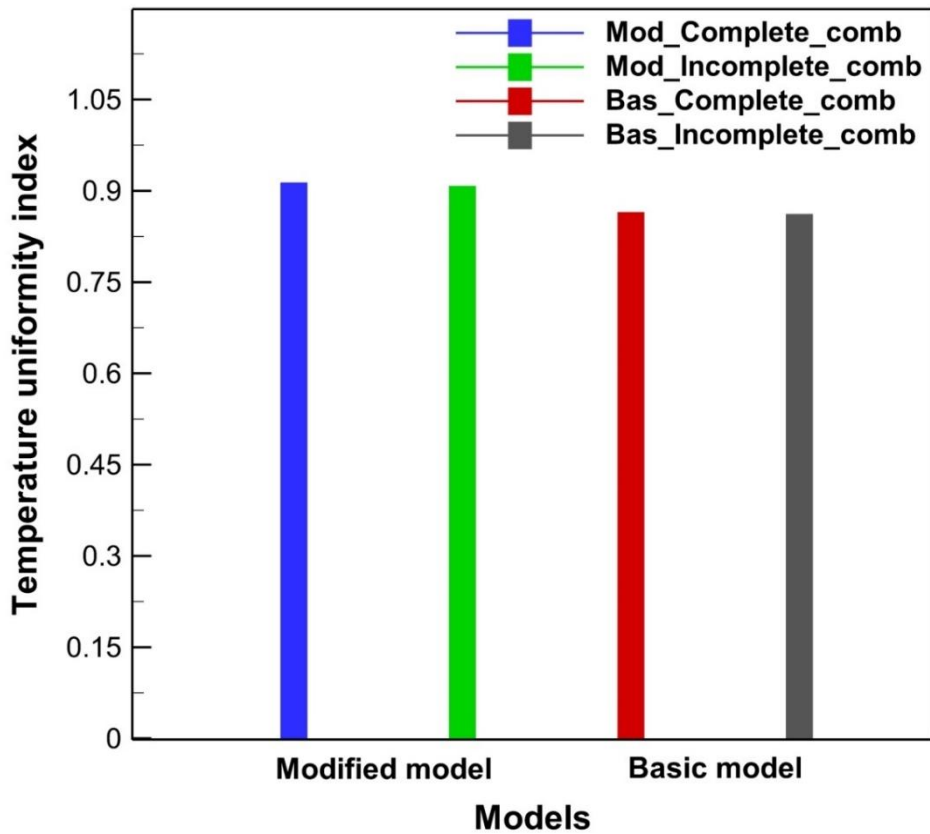


**Figure 3.8** Comparison of the temperature uniformity index at the backside of the steel plate for the basic and modified models.

Figure 3.9 shows the lengthwise temperature distribution at the backside of the steel plate from the center to the edge for combinations of the experimental and simulation result and the basic and modified model in the case of the complete combustion,  $\Phi = 1.0$ . In the basic model, temperature decrease from the center to  $x = 0.15\text{m}$  is around  $30^\circ\text{C}$  while in the modified model, temperature decrease along the

same distance is around 12°C. And then, the temperature decreases promptly due to heat transfer to the cool ambient air. However, temperature difference of the modified model is still less than that of the basic model. Numerical simulation results for the two models in these cases show also good agreements with experimental results.

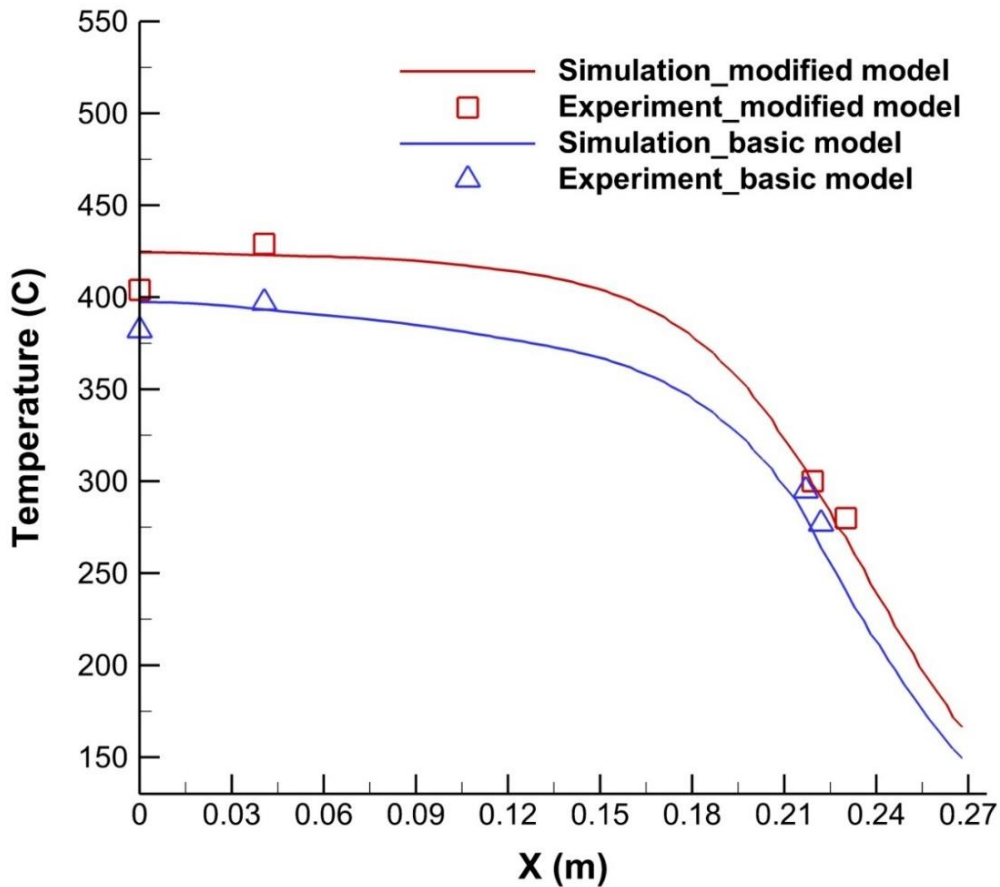


**Figure 3.9** Comparison of the temperature distribution at the backside steel plate from the center to the edge for the complete combustion.

### 3.4 Comparison of flame structure and steel plate temperature distribution of the models with and without guide vane

Base on the results of comparison between the basic and modified models, the modified model has more uniform temperature distribution than the basic model. In addition, the effect of guide vane at the outlet of gas torch is also important. Numerical simulations with and without guide vane models are performed in this section.

Figure 3.10 shows a comparison of the temperature distribution of the two models with and without the guide vanes for the region from the gas torch outlet to the steel plate. The maximum temperatures for the two cases were approximately the same when the reactant mixture is ignited. But the decrease in the gas flame temperature without the guide vanes was larger ( $Y/d = 5-50$ ) than that with the guide vanes. Furthermore, the temperature with the guide vanes inside the steel plate ( $Y/d = 50-60$ ) was higher than that without the guide vanes, as shown in Figure 3.10. This is due to the guide vanes reducing the heat loss more because the two sides of the flame jets (see Figure 3.11a (right)) protect against radiation and convection heat loss.

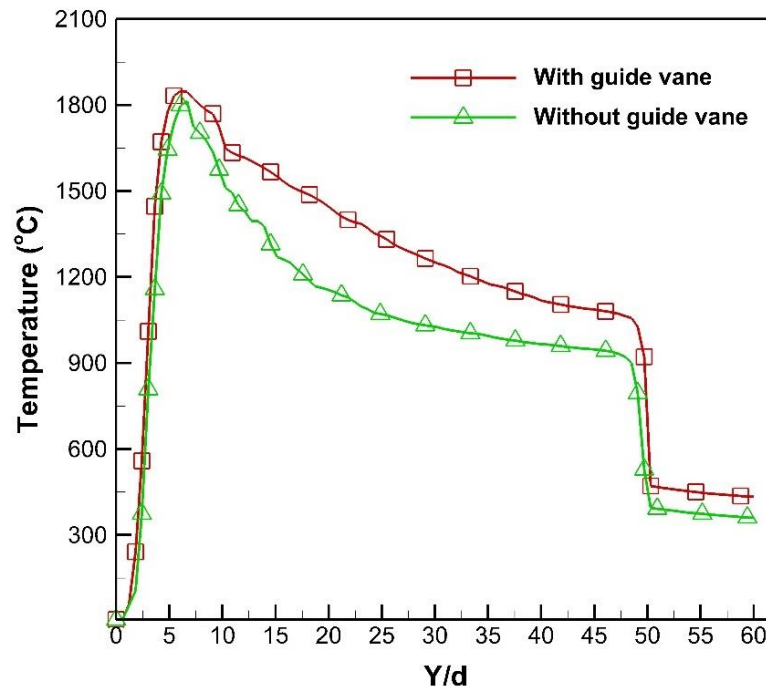
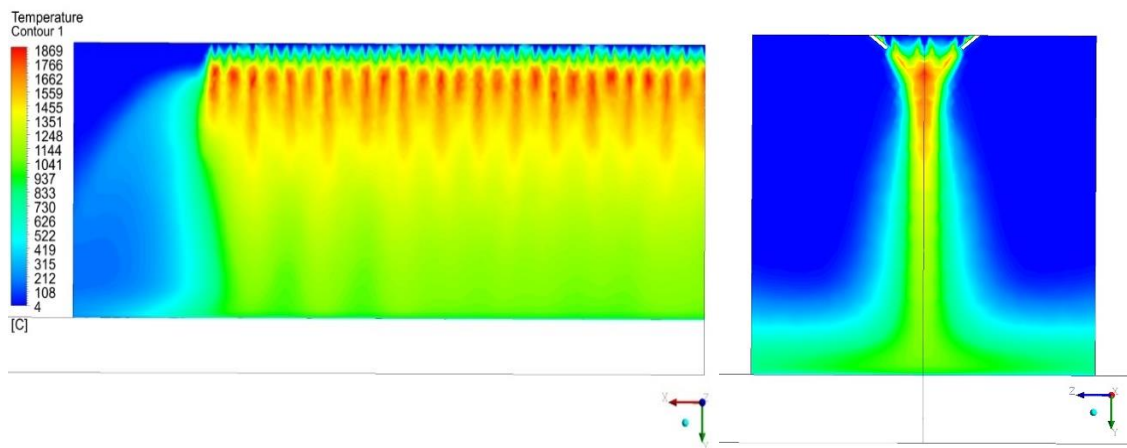


**Figure 3.10.** Comparison of the temperature distribution with and without the guide vanes as a function of  $Y/d$ .

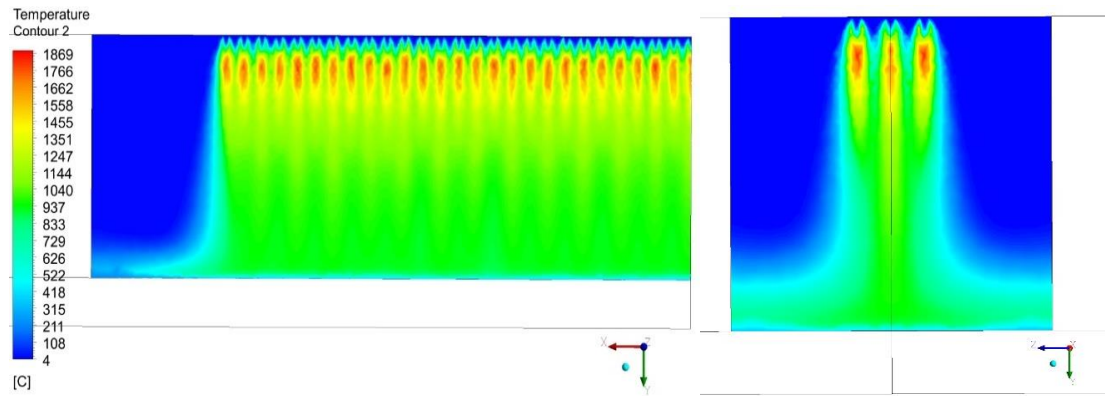
The steel preheating process was conducted with an LPG/air mixture for combustion, and the temperature contours of the center view and side view section are presented in Figure 3.11. Due to the high speed of the outlet jet, the ambient air is entrained in the flame zone and participates in the combustion process. The primary jet

line at the center line of the gas torch is associated with the main combustion process. On the side view, due to the guide vanes at the outlet, the two secondary jet lines located at the two outer sides are concentrated and enhance the plate temperature when the combustion happens. However, for the other model without guide vanes, the flame from the jet holes directly impinges on the steel plate without being focused, as shown in Figure 3.11b (right).

The temperature contours at the steel plate bottom for two models (with and without guide vane) are shown in Figure 3.12. Due to the focused flame, the highest temperature at the bottom of the steel plate was 424 °C for the model with guide vanes and 359 °C for the model without guide vanes. The temperature difference between the two models was 65 °C. Therefore, by using the guide vanes to focus the flame, the temperature of the steel plate was significantly enhanced.

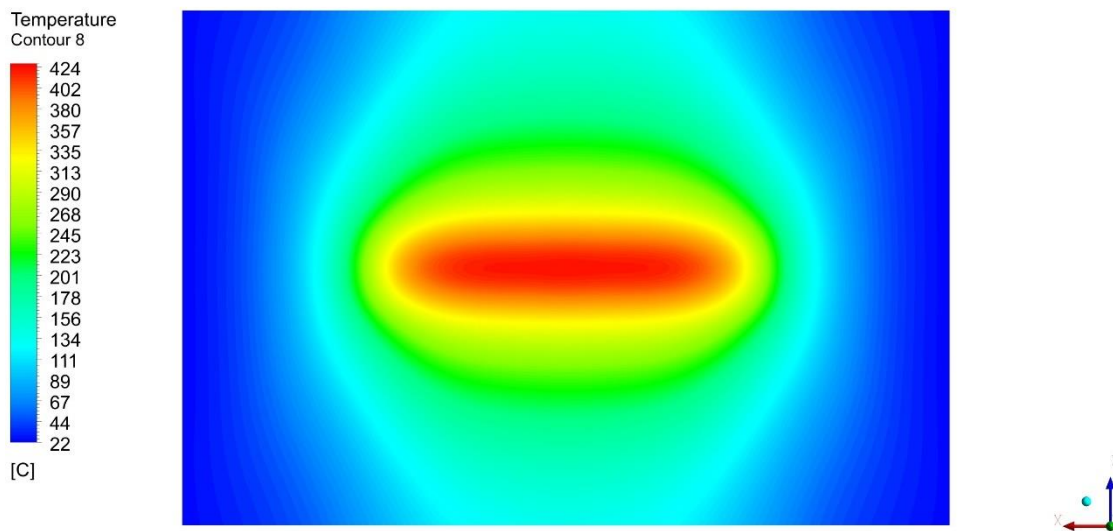


(a)

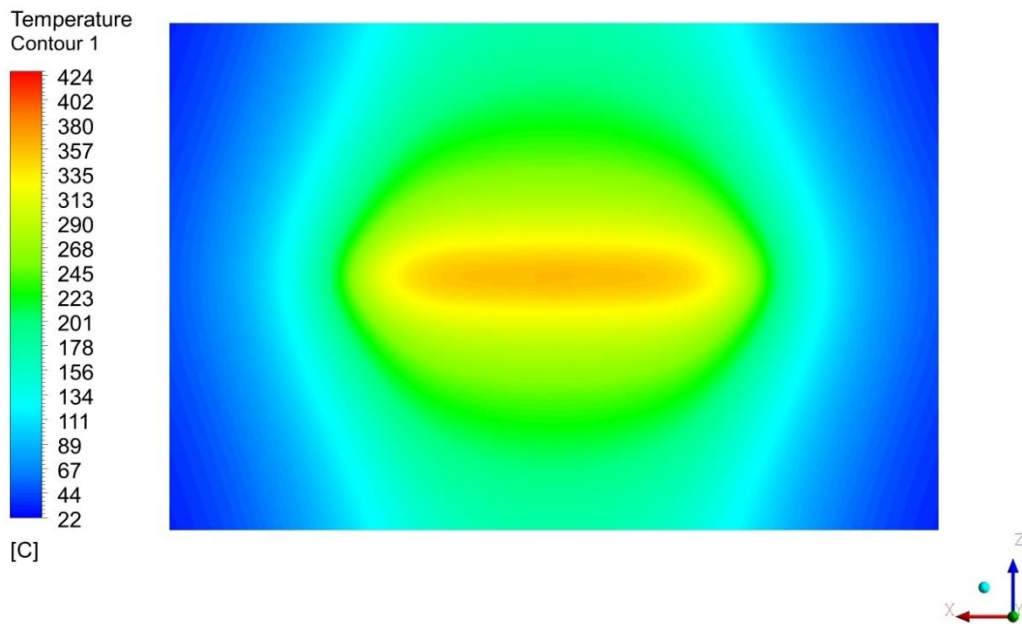


(b)

**Figure 3.11.** Temperature contours from the gas torch outlets to the steel plate at the center view (left) and side view (right) section when preheating the steel plate at  $\Phi = 1$ ,  $Re = 3483$ , and  $Y/d = 50$ : (a) With guide vanes; (b) without guide vanes.



(a)



(b)

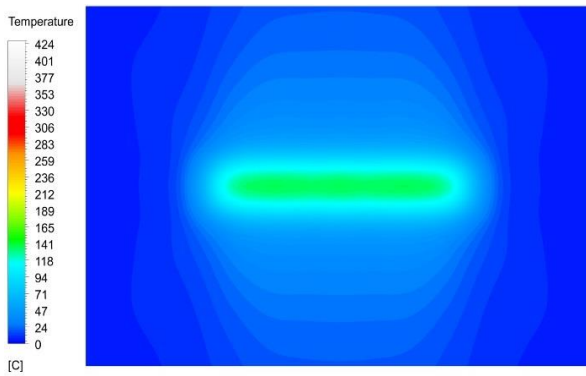
**Figure 3.12.** Temperature contours at the bottom surface of the steel plate for two models at the operating conditions of  $\Phi = 1$ ,  $Re = 3483$ , and  $Y/d = 50$ : (a) with guide vanes; (b) without guide vanes.

### 3.5 Unsteady temperature distribution at the back side of steel plate

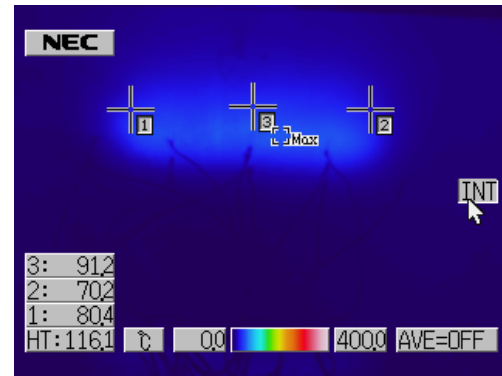
Figure 3.13 shows the transient temperature contours at the back side of the steel plate from the numerical and experimental results. At 135 second, a high temperature was observed at the center area of the back side of the steel plate. This occurs because the flame impinges on the central part of the steel plate, while the other regions are almost invariant. The steel heating process continues until 1005 second and then approaches steady state at 1800 second. At 1005 second, there is clearly a high temperature distribution in the center area.

The numerical simulations are in good agreement with the experimental results. When approaching steady state at 1800 second, the temperature at the center area from

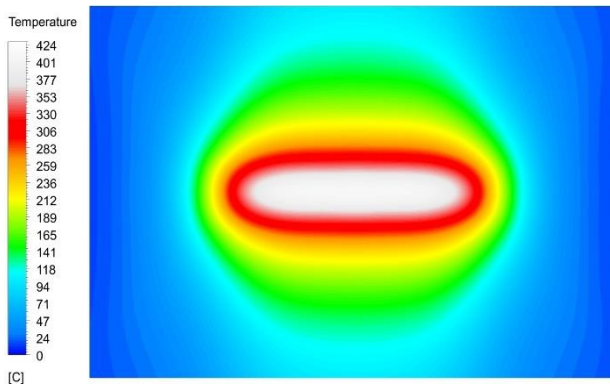
the numerical result was around 424°C, while the range of the experimental results was 404 to 429°C. Consequently, the deviation of the regional temperature at the center between the numerical simulation and the experimental results are in the range of 1.1 to 4.9%.



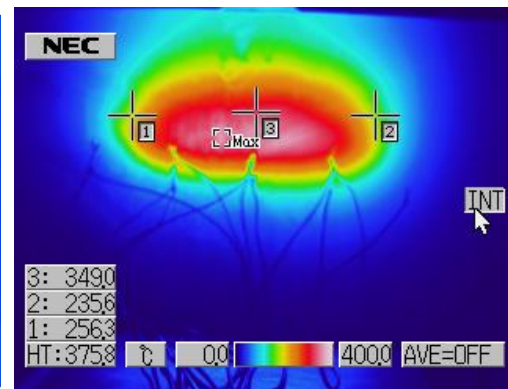
Simulation time = 135 second



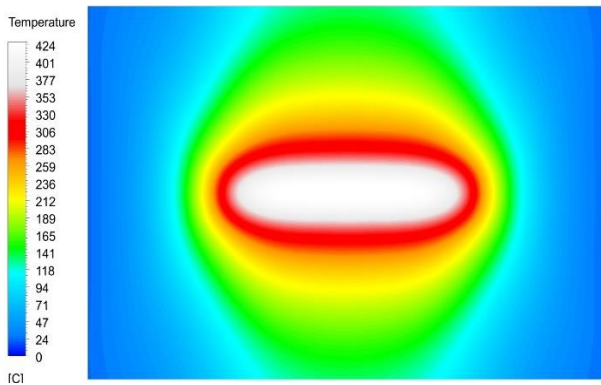
Experiment time = 135 second



Simulation time = 1005 second

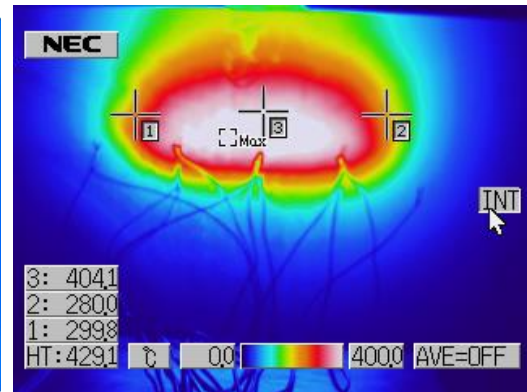


Experiment time = 1005 second



Simulation time = 1800 second

(a)



Experiment time = 1800 second

(b)

**Figure 3.13** Temperature contour on the backside of steel plate: (a) Numerical simulation; (b) Experiment results

Figure 3.14 shows the temperature at the center point of the back side of the steel plate as a function of time. The temperature increases from the initial temperature and approaches the steady-state temperature of 424°C at 1800 second. The numerical simulation results are in good agreement with the experimental results. At steady state, the deviation between the numerical simulation and experimental results is approximately 4.9%.

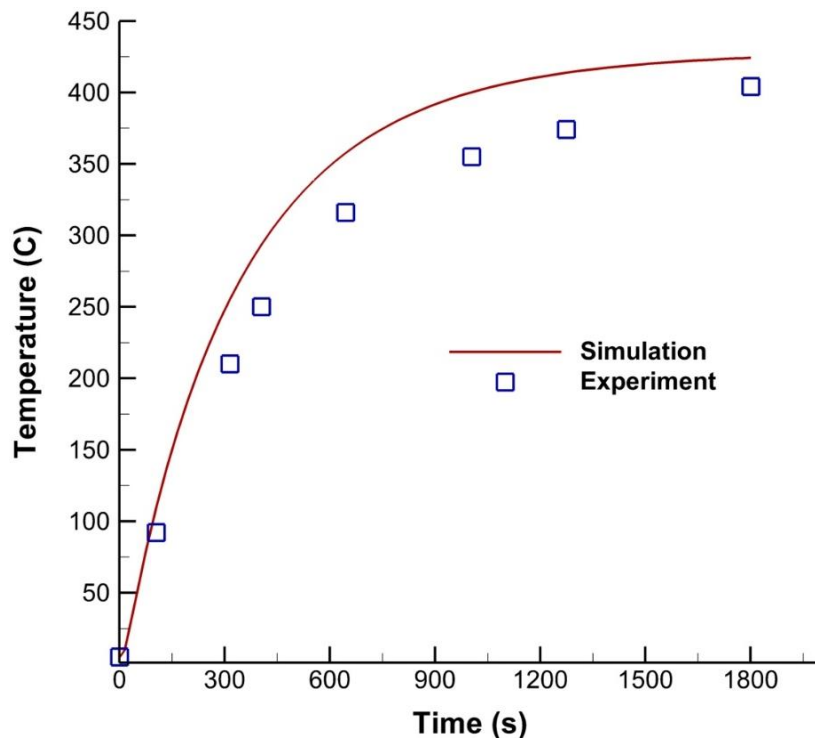


**Figure 3.14** Temperature at the center point of the back-side of the steel plate as a function of time during steel preheating process

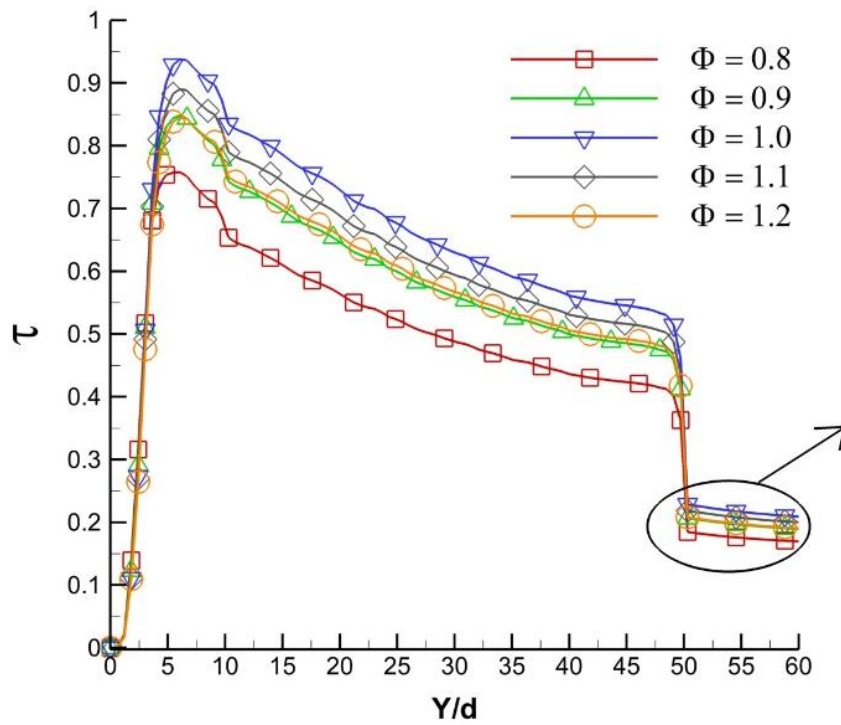
### 3.6 Effect of operational variables on temperature distribution at steady state

#### 3.6.1 Effect of equivalent ratio ( $\Phi$ ) on temperature

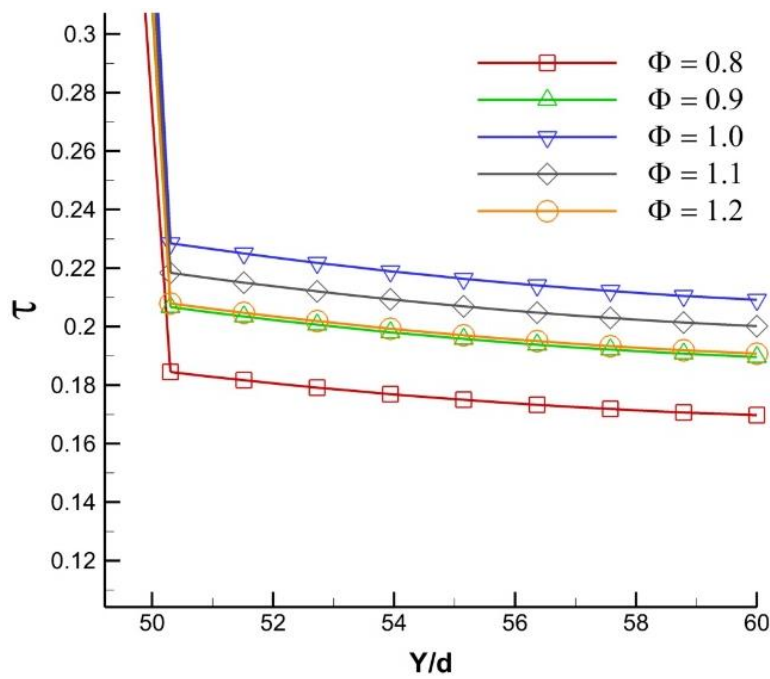
Figure 3.15(a) shows the non-dimensional temperature distributions of the impinging flame jet as a function of  $Y/d$  at various equivalence ratios (from fuel lean to fuel rich).

The non-dimensional temperature is defined as follows:

$$\tau = \frac{T - T_{unb}}{T_{ad} - T_{unb}} \quad (3.16)$$



(a)



(b)

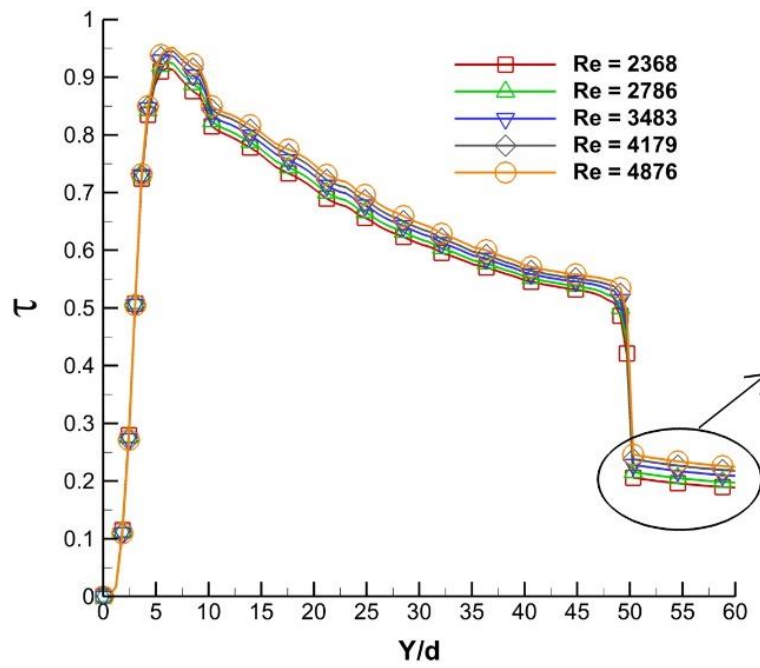
**Figure 3.15** (a) Temperature distribution for various equivalent ratios as a function of  $Y/d$ . (b) enlarged only for the steel plate thickness

All the mixture temperature distributions for different equivalence ratios showed similar trends. The mixture leaves the torch with low temperature and is then ignited. The temperature increases rapidly for a short distance ( $Y/d \approx 5$ ) near the torch. After that, the temperature decreases significantly because heat is released to the ambient air, and finally, the flame impinges on the steel plate ( $Y/d = 50$ ). The highest temperature was achieved with a stoichiometric reaction. The other cases showed lower temperatures at equivalence ratios of 1.1, 0.9, and 1.2, and finally, the lowest temperature distribution occurred at the equivalence ratio of 0.8. The heat was transferred from the flame side to the back side of the steel plate, as shown in Figure 3.15(b).

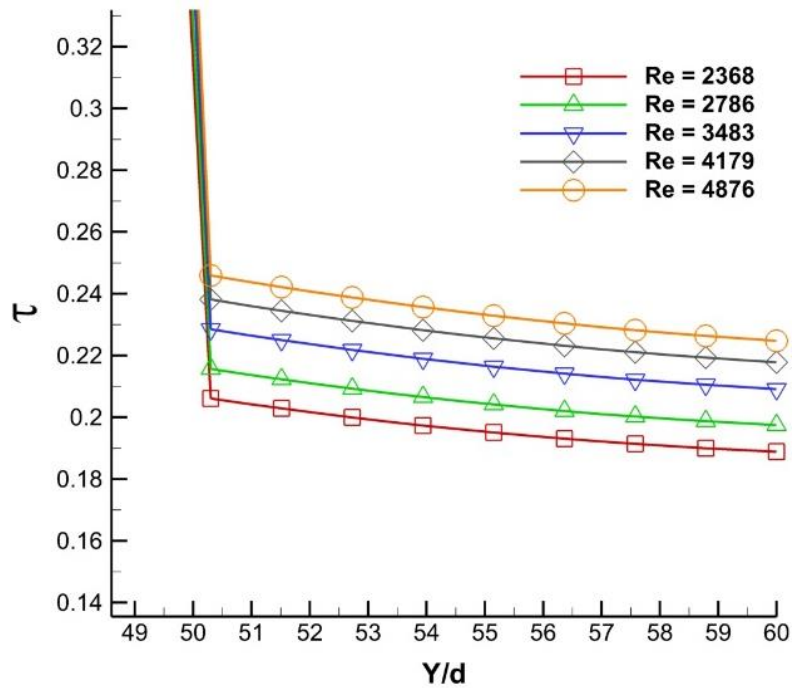
In these conditions, the line for the stoichiometric reaction also presented the highest temperature line. Because of the heat conduction inside the steel plate, the temperature trend is linear from the front side to the back side of the plate. The temperature difference between the front side and the back side is not very large due to the high thermal conductivity of the plate

### **3.6.2 Effect of Reynolds number (Re) on temperature**

The effect of the Reynolds number on the temperature distribution was investigated from  $Re = 2368$  to  $Re = 4876$  at an equivalence ratio of 1.0 and  $Y/d = 50$ , as shown in Figure 3.16(a). The temperature of the flame side and back side of the steel plate is enhanced when  $Re$  increases from 2368 to 4876. Increasing  $Re$  means increasing the flow rate of the mixture and hence increasing the heat transfer rate to the steel plate. As a result, the combustion is improved by the high level of turbulence and the high heat release rate due to the increased fuel/air mixture rate. Therefore, there is an increase in the temperature of the plate on the flame side and back side. The plate temperature increases as the Reynolds number increases. These phenomena are shown in Figure 3.16(b) and can also be found in other studies [40,41].



(a)



(b)

**Figure 3.16** Effect of the Reynolds number on temperature distribution (a) as a function of  $Y/d$ , (b) enlarged for only the steel plate thickness range

### 3.6.3 Effect of the distance from gas torch outlet to steel plate on temperature

Figure 3.17 shows the temperature distributions along the x-direction on the back side of the steel plate from the center to the edge for various distances  $H/d$ . The investigated distance range is  $H/d = 25$  to  $75$  with a stoichiometric reaction ( $\Phi = 1$ ) and Reynolds number of  $3483$ . The steel plate temperature does not change much from the center to  $X/d = 75$  but decreases much more from  $X/d = 75$  to the end due to the cooling from the ambient air. From  $H/d = 25$  to  $75$ , increasing the distance between the torch outlet and the steel plate results in a greater decrease in the temperature distribution on the back side of the plate. The combustion gas temperature decreases as the combustion gas becomes farther recedes from the gas torch.

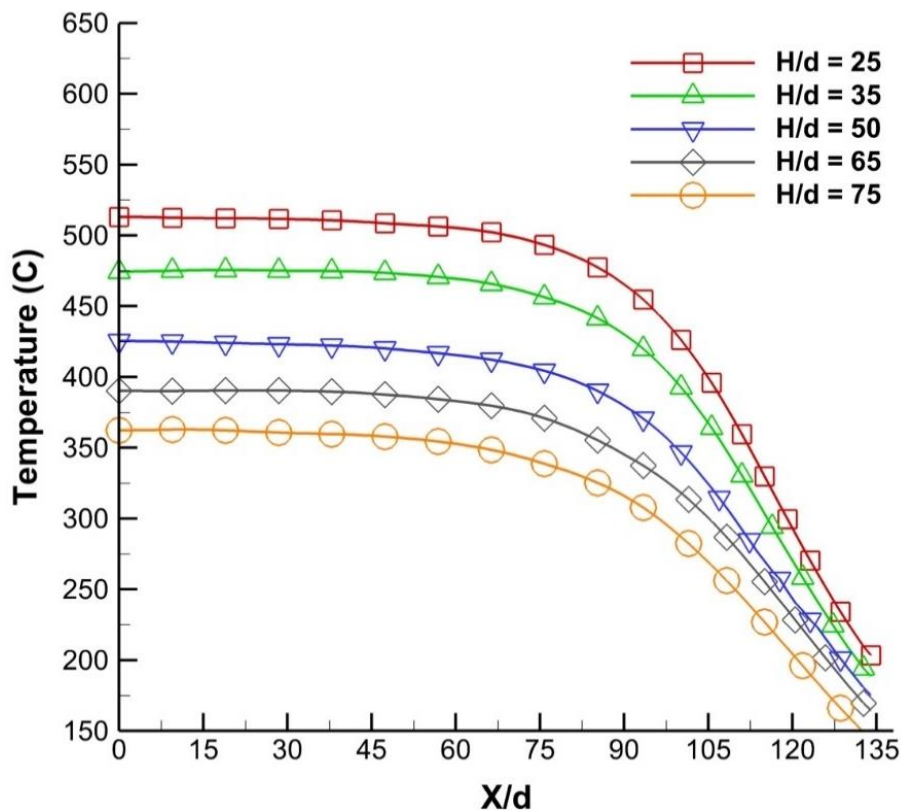


**Figure 3.17** Effect of distance from the gas torch on the temperature distribution along the x-direction from the center to the edge on the back side of the steel plate.

### 3.7 Optimizing the guide vane angle on the gas torch outlet surface

The guide vane angle at the gas torch outlet is also important to achieve a desired temperature. A guide vane with a certain horizontal angle is shown in Figure 3.18. The effect of the guide vane angle variation from 30 to 60 degrees on the steel preheating performance was examined. The Reynolds number, equivalence ratio, and ratio of the axial torch outlet-to-plate distance to the nozzle diameter were fixed at 3483, 1.0, and 50, respectively.

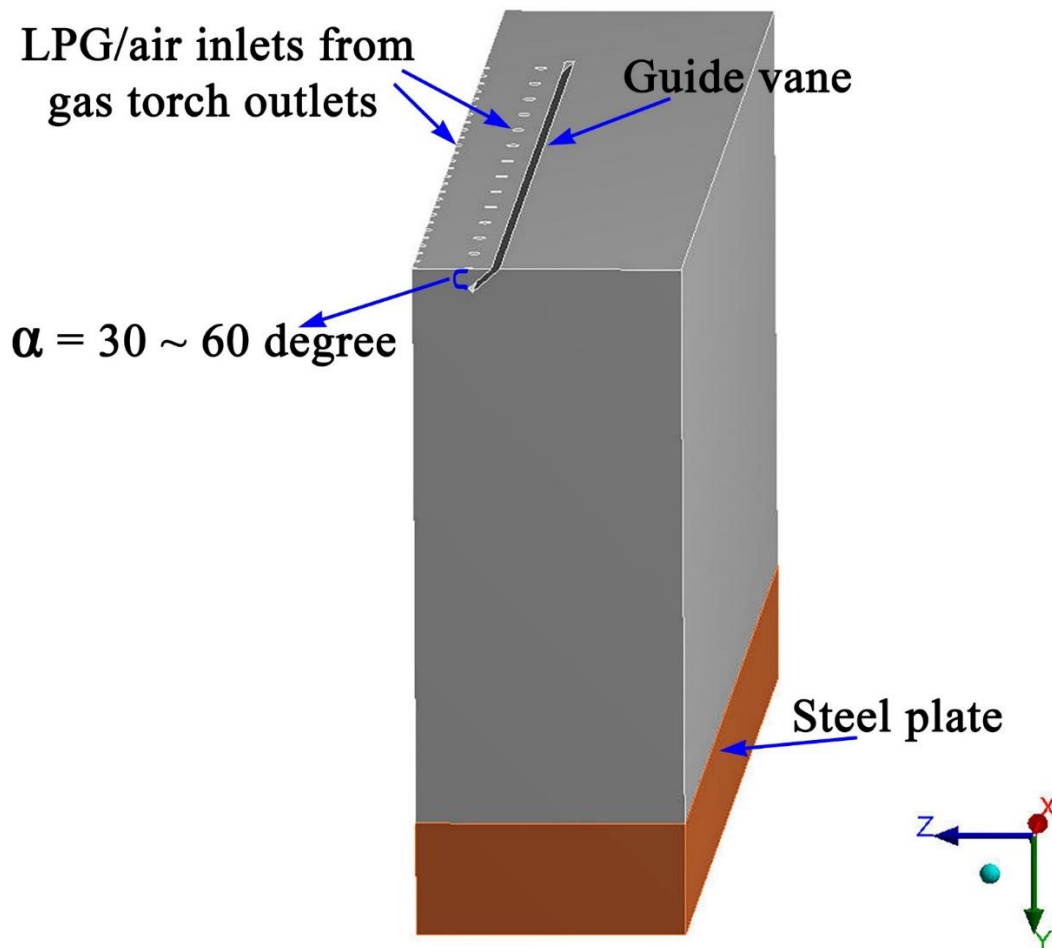
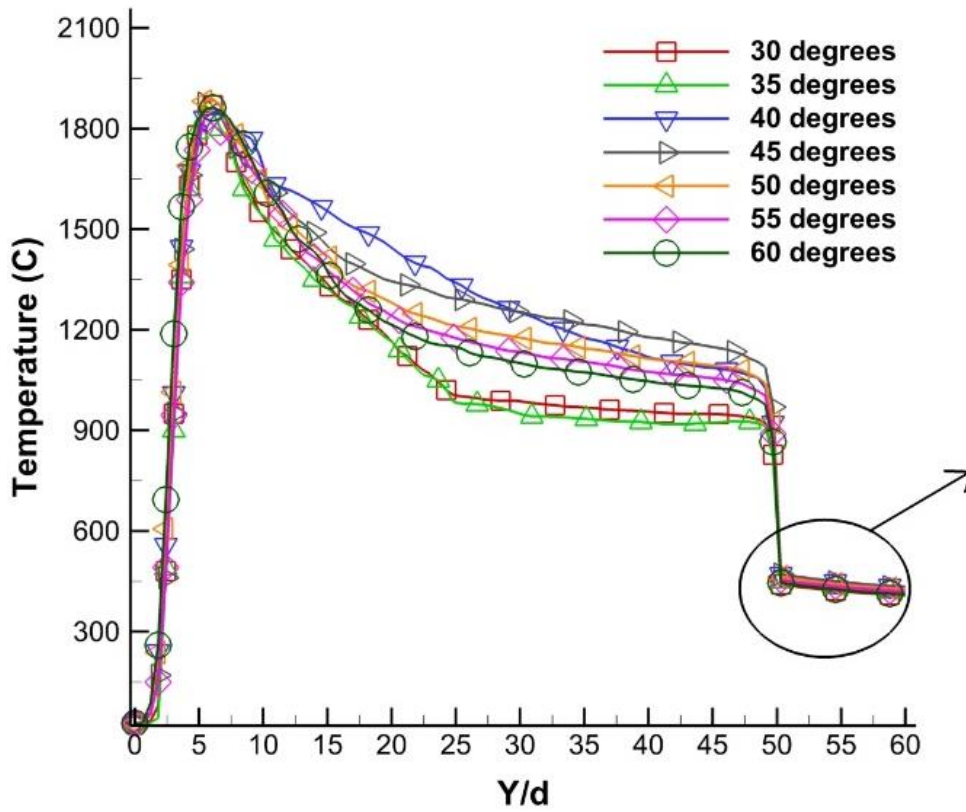


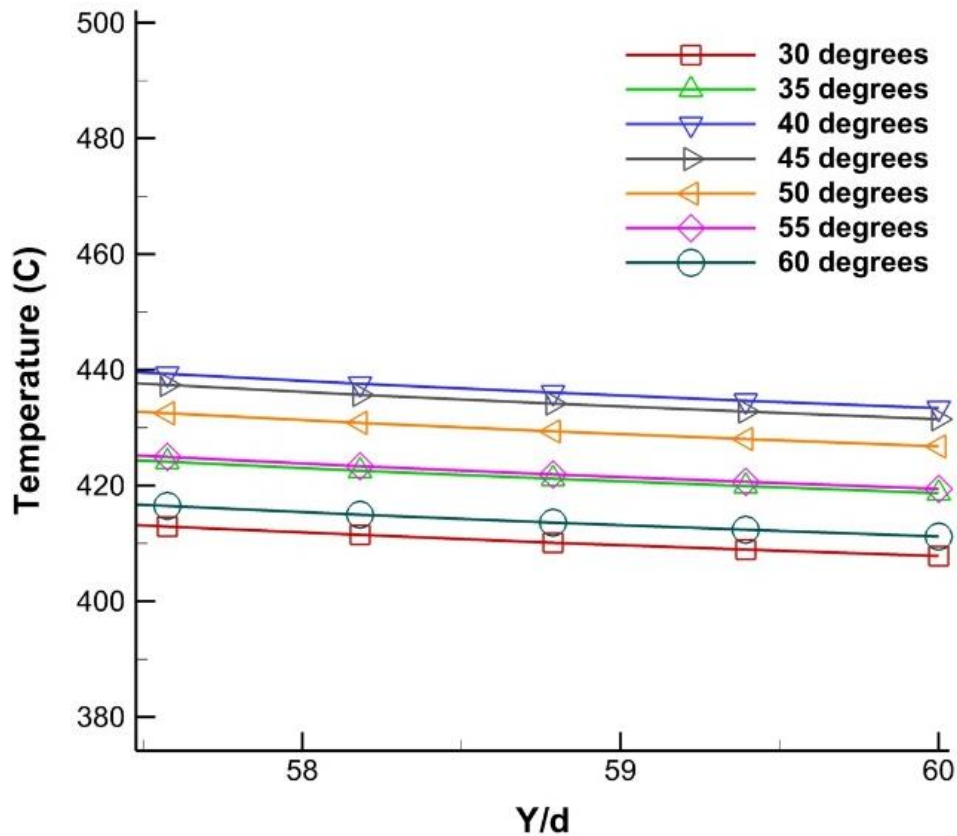
**Figure 3.18** Guide vane angle variation from the jet flow of the gas torch

The temperature distribution is plotted as a function of Y/d for various guide vane angles in Figure 3.19(a). For the initial combustion, the flame temperature

distributions for all angles are similar. After approaching the highest temperature at  $Y/d \approx 5$ , the flame temperature decreases due to ambient air cooling, and then the flame impinges on the steel plate. The temperatures for all the angles inside the steel plate are presented in Figure 3.19(b). The case with the guide vane angle of 40 degrees shows the highest temperature of the back side of the steel plate. Therefore, the optimized angle of the guide vane at the outlet of the gas torch is considered to be approximately 40 degrees.



(a)



(b)

**Figure 3.19** Effect of the guide vane angle variations on the temperature distribution: (a) as a function of Y/d, (b) enlarged for only the steel plate thickness range.

### 3.8 Summary

The temperature differences for the basic and modified models were 229°C and 90°C, respectively. The numerical simulation results using ANSYS FLUENT also showed good agreements with the experimental results for both complete and incomplete combustion. The temperature was improved for the model with the guide vanes by 65°C.

The transient numerical simulation and experimental results were in good agreement. At steady state, the back-side temperature deviation of the steel plate

between the numerical simulation and experimental results was approximately 4.9%. The influences of the equivalence ratio ( $\Phi$ ), Reynolds number ( $Re$ ), and downstream distance from the torch outlet plate toward the steel plate ( $Y/d$ ) were investigated. For the equivalence ratio, the highest temperature was found at the stoichiometric value. Higher Reynolds number resulted in higher temperature distribution on the back side of the plate. The steel plate temperature decreased monotonically as the distance between the torch outlet and the steel plate increased.

To improve the gas torch performance, the guide vane angle at the outlet of the gas torch had to be optimized. An angle of 40 degrees resulted in the highest temperature distribution. At this angle, the temperature of the steel plate showed a maximum increment of 25°C compared with other angles. In addition, guide vanes at appropriate angles may lead to energy savings by attaining higher temperature of the steel plate and high preheating performance with a uniform temperature distribution.

# **Study of flow field and temperature distribution of Hot Mixing Chamber (HMC)**

## **4.1 Description of operating principle of Hot Mixing Chamber (HMC)**

The hot mixing chamber (HMC) is a device that mixes hot combustion gas and cold air to obtain a gas with a pertinent operational temperature in the final outlet section which we can meet in industry requirements. Figure 4.1 shows the operating principle of Hot Mixing Chamber (HMC). Liquefied Petroleum Gas (LPG) pressure leaving the vessel is reduced by the pressure regulating valve. And then the LPG passes the flow rate gauge and enters to the burner device. On the other hand, the cold air is also supplied to the burner and mixed with LPG. LPG/air mixture is then used for combustion process. In addition, cold air is also supplied as the secondary stream for mixing with the combustion gas to match the required temperature at the outlet of HMC.

The physical mechanism of the enhancing flow uniformity of the modified model was that the well-mixed combustion gas was obtained compared with the basic model by modifying the inner and outer structures. Moreover, the surface temperature of the HMC was reduced when combustion happened.

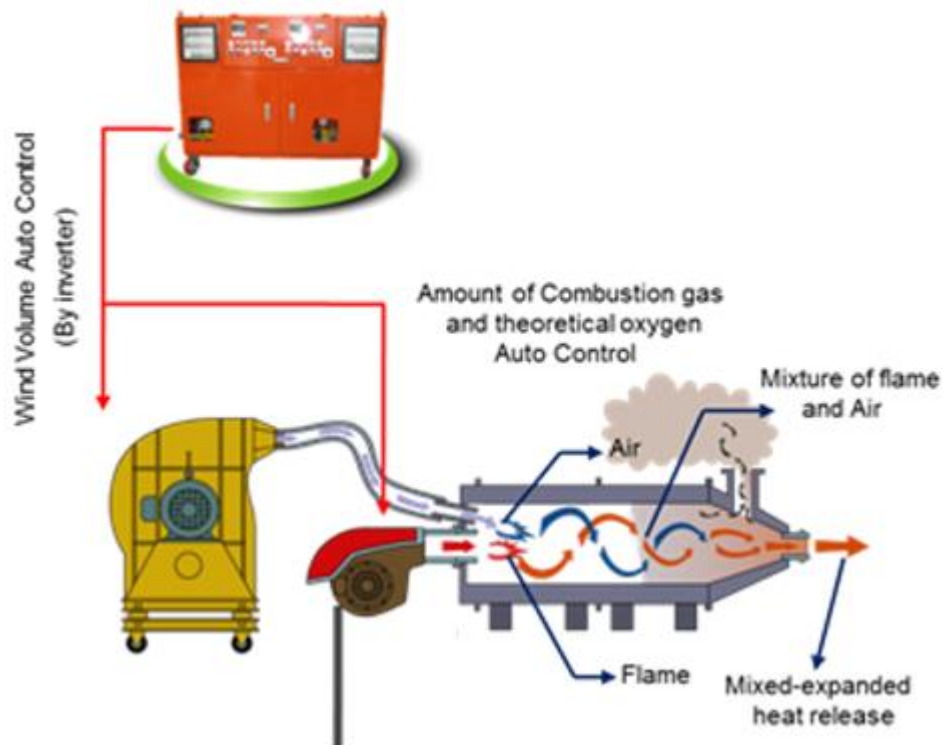


**Figure 4.1** Operating principle of Hot Mixing Chamber

## 4.2 Basic and modified HMC models

### 4.2.1 Basic HMC model

The basic HMC model has a fuel/air mixture inlet and cold air inlet as shown in Figure 4.2. The fuel/air mixture inlet is located at the center of the cross-section of the HMC. The cold air inlets are located around the HMC surface. The combustion gas and cold air are mixed together to approach the required temperature at the outlet port. The dimensions of HMC are shown in Table 4.1



**Figure 4.2** The 3D basic model of Hot Mixing Chamber

**Table 4.1** Specification of the basic HMC

Parameters	Dimensions, mm
Fuel/air inlet diameter	90
Cold air inlet diameter	52
Outlet diameter	250
HMC body diameter	400
HMC length	1300

#### 4.2.2 Modified HMC model

Design of the modified model aims to mix the combustion gas and cold air to meet the required temperature at the outlet port of HMC and reduce the HMC surface temperature during operating the HMC. The modified HMC model has a fuel/air mixture inlet and three cold air inlets as shown in Figure 4.3. The dimensions of the modified model are shown in Table 4.2. The fuel/air mixture inlet is located at the

center of the cross-section of the HMC. The three cold air inlets are located around the HMC surface and equally spaced at 120 degrees. The inside structure of the inner vessel is a perforated cylinder. There are 6 holes in each cross-sectional circle and 12 holes in each main flow direction. Every hole diameter is 30mm. The perforated inner vessel of the HMC can increase the hot and cold air mixing rate and may decrease the HMC outside surface temperature, due to successive discharging to the main flow and the collision of the splitted flow between the outer vessel and the perforated inner vessel. In addition, the vortex generator is established near the end of the perforated cylinder to enhance mixing the combustion gas and cold air.

**Table 4.2** Specification of the modified HMC

<b>Parameters</b>	<b>Dimensions, mm</b>
Fuel/air inlet diameter	90
Cold air inlet diameter	30
Outlet diameter	250
HMC body diameter	400
HMC length	1300
Holes diameter	30
Number of holes	72
Vortex generator diameter	100

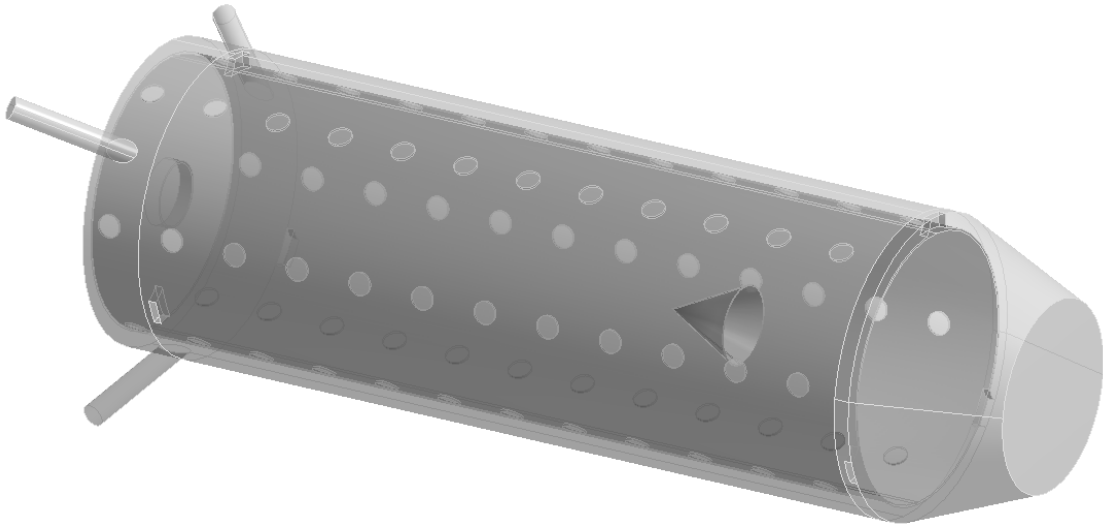


**Figure 4.3** The 3D modified model of Hot Mixing Chamber

#### **4.3 Boundary conditions and method**

In this study, the ANSYS FLUENT software is used for simulation for the basic and modified model. Figure 4.4 shows the fluid domain with the mesh grid for the HMC model. The tetrahedral grids were used to make simulation mesh. The grid number of the HMC was nearly 1.2 million. The boundary condition and method of present simulation is shown in Table 4.3. The fuel and air mixture inlet velocity is in the range of 1 to 3 m/s. Inlet velocity and temperature of the cold air were 23 m/s and 300 K, respectively. The equivalent ratio was investigated in the range from the fuel lean of 0.8 to the fuel rich of 1.2. The  $k-\epsilon$  turbulence model was used in this study. With the consideration of the radiation effect, the discrete ordinates (DO) radiation model was used. The absorption coefficient was modeled using the weighted sum of gray gases model (WSGGM). No slip condition was selected for the wall boundary condition.



(a)



(b)

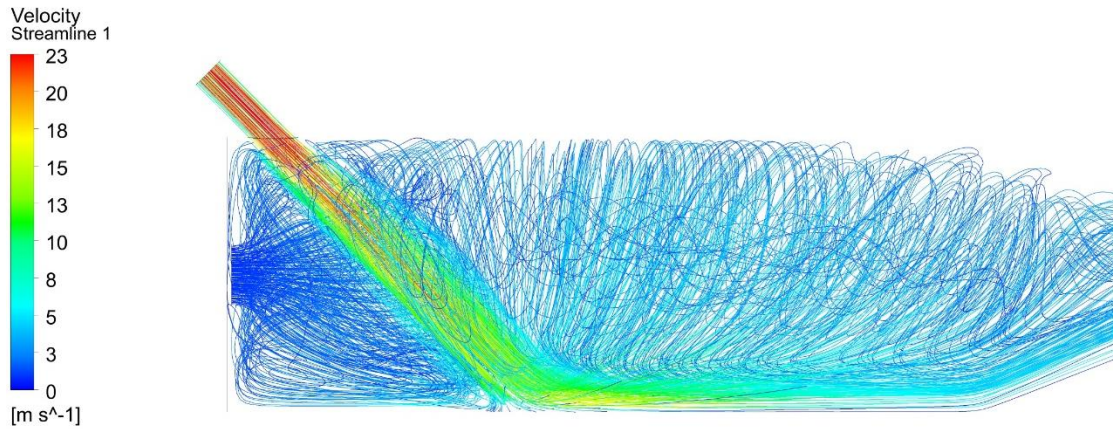
**Figure 4.4** The 3D mesh model of Hot Mixing Chamber: (a) Basic model; (b) Modified model

**Table 4.3** The boundary condition of HMC

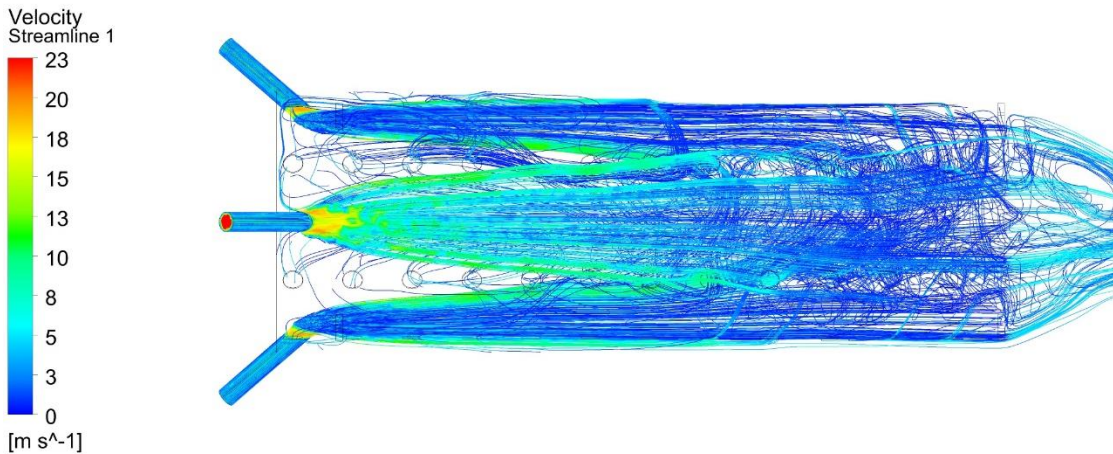
<b>Parameters</b>	<b>Values/method</b>
Fuel/air mixture velocity inlet	1-3 m/s
Cold air velocity inlet	23 m/s
Cold air inlet temperature	300 K (27°C)
Turbulent model	Standard k- $\epsilon$
Radiation model	Discrete Ordinates (DO)

#### **4.4 Comparison between the basic and modified HMC model**

For comparison of the flow field and temperature distribution between the basic and the modified model, the mass flow rates of the inlet fuel/air mixture and the inlet cold air do not change for both two models. Velocity streamline distribution inside Hot Mixing Chamber for the basic and modified model is shown in Figure 4.5. For the basic model, due to one cold air inlet, the flow field distributions at the inlet and outlet section of HMC are non-uniform. The inclined cold air flow impinges on the bottom of HMC and leaves the outlet port. This leads to not only the high surface temperature near the flame area but also the low surface temperature in the other regions. On the other hand, by using three cold air inlets and the perforated cylindrical pipe, the flow field distribution of the modified model was completely different to that of the basic model. The main cold air flows along the perforated inner cylinder and moves out HMC at the outlet section. The rest of the cold air passes through holes on the perforated cylinder to mix with the combustion gas. Moreover, the vortex generator has a function to enhance mixing of the mixture flow before moving out at the outlet. These peculiar configurations of the modified HMC make the flow mixing to be improved and also the HMC surface temperature to be greatly reduced, compared with the basic HMC model.



(a)



(b)

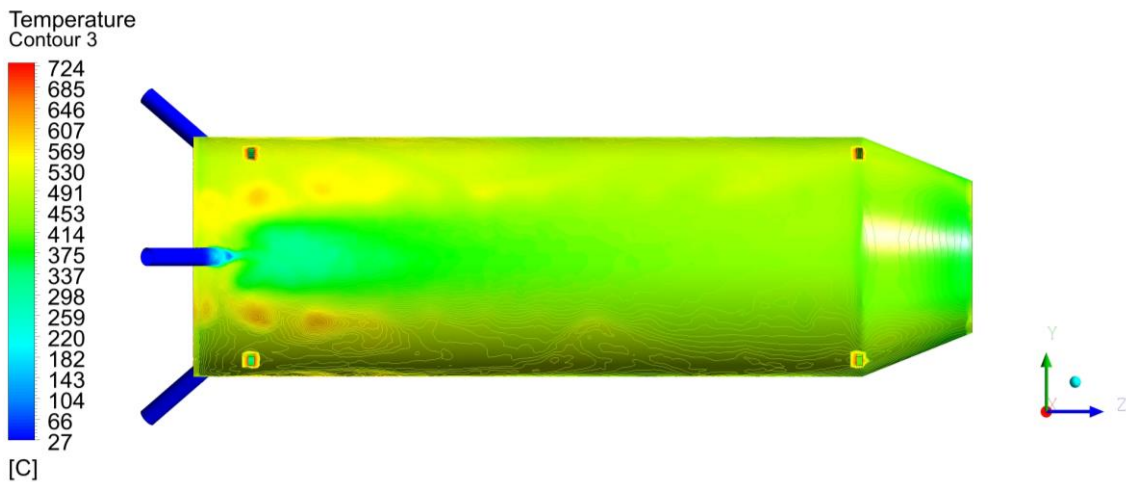
**Figure 4.5** Velocity streamline of Hot Mixing Chamber: (a) Basic model; (b) Modified model

The surface temperature contour of Hot Mixing Chamber for the basic and modified model was shown in Figure 4.6. With one unbalanced cold air inlet and without the perforated inner cylinder, the temperature distribution on the basic HMC surface was shown in Figure 4.6(a). The highest surface temperature is 724°C at flame area and 570°C at another regions. On the other hands, by using the three cold air inlets and perforated pipe, the surface temperature maintains 400°C on most of the surfaces except the highest temperature around 674°C near the start of combustion as shown in

Figure 4.6(b). Therefore, by using this configuration, the modified HMC model may reduce the surface temperature and extend the operating period of the chamber.



(a)

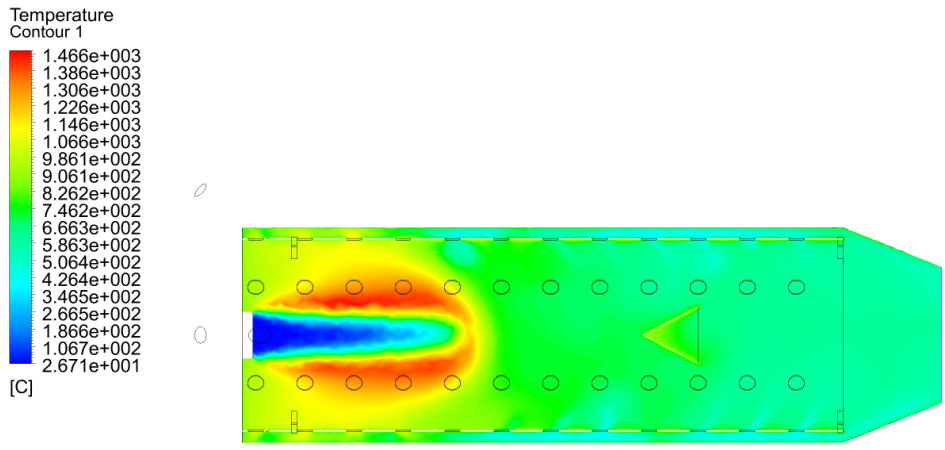


(b)

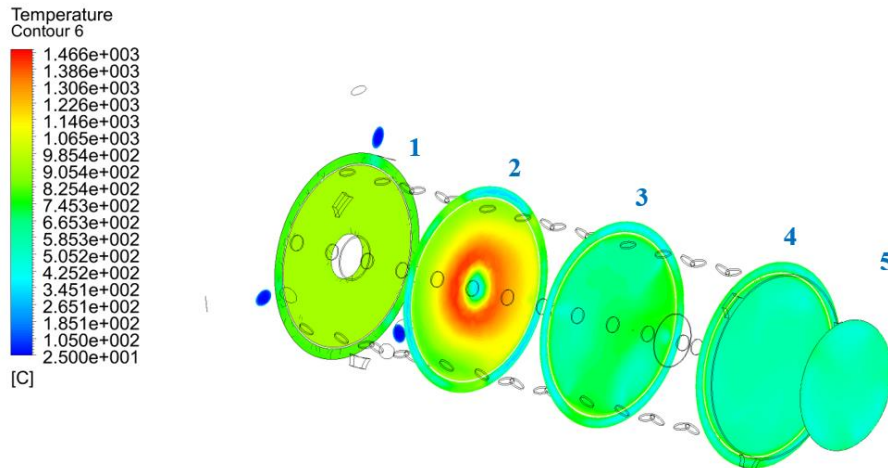
**Figure 4.6** Surface temperature of Hot Mixing Chamber: (a) Basic model; (b) Modified model

The temperature distribution within the modified Hot Mixing Chamber was shown in Figure 4.7. The highest temperature approach 1466°C at equivalent ratio ( $\Phi$ ) value of 1.0 and Reynolds number (Re) at fuel/air mixture inlet of 6302. Due to the cold air pass along the perforated cylinder and the inner HMC surface, the temperature in this region is lower than the others. It can be observed in the multi-sections of HMC in

Figure 4.7(b). The highest temperature is located at plane 2 and the flow temperature decreases up to plane 5 at the outlet of HMC. Through all section planes, it can be found that the HMC surface (edge of sections) has lower temperature than the inner sections. This is because the surface cooling by three cold air inlets. And the outlet temperature is also uniform because the downstream flow is well mixed by the perforated inner cylinder and the vortex generator device.



(a)

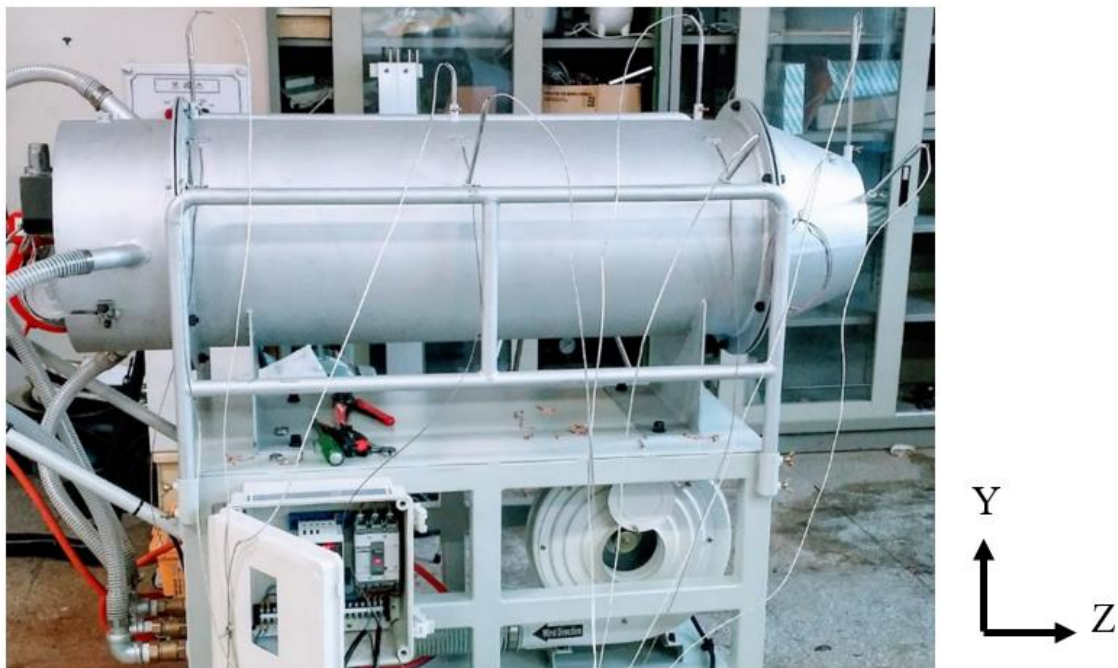


(b)

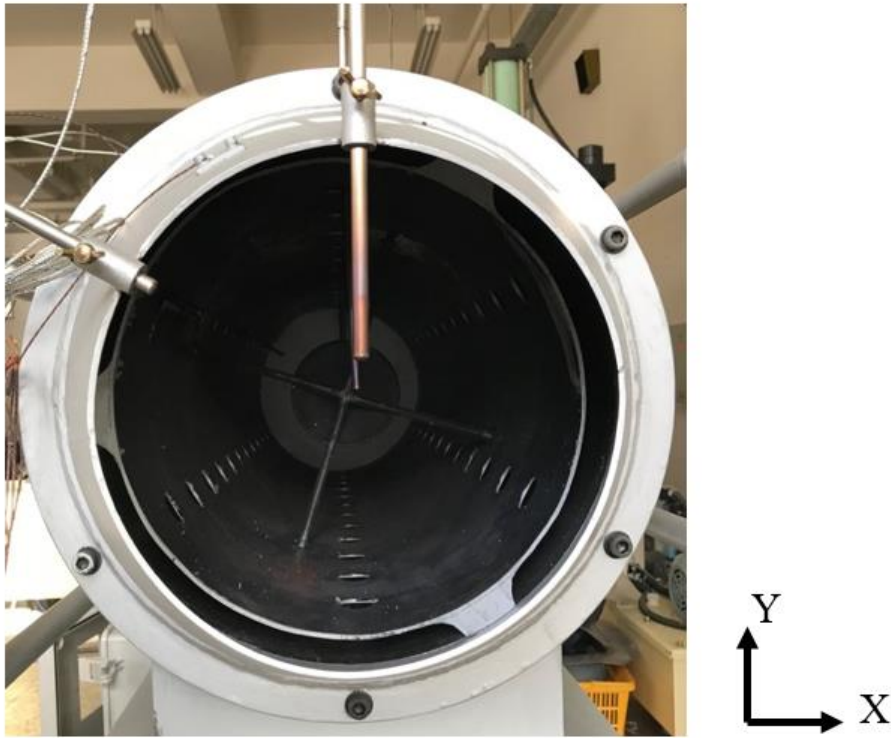
**Figure 4.7** The temperature contour of Hot Mixing Chamber: (a) at the center section; (b) Multiple sections inside HMC

#### 4.5 Experimental validation

Experiment was carried out to get validation and compare with numerical simulation results by ANSYS FLUENT software. Experimental apparatus for the HMC was setup and shown in Figure 4.8. The LPG/air mixture was supplied to the burner and then the flame was ignited by the auto ignition device. On the other hand, the cold air velocity was adjusted and supplied by the type of the KHB centrifugal blower to Hot Mixing Chamber for two objectives: the first is for mixing with the hot combustion air, the second is cooling down the HMC surface temperature during the combustion process. The temperature was measured by the K-type thermocouples and the results was displayed by the Yokogawa temperature recorder.



(a)



(b)

**Figure 4.8** HMC experiment apparatus setup: (a) front view; (b) side view

Temperature distribution along z-direction was shown in Figure 4.9 for simulation and experimental results at the center, the half of radius, and the surface of the HMC. At the center, the fuel/air mixture leaves the burner with low temperature and then is ignited to set flame. The temperature increases rapidly and approaches the highest temperature around 1400°C. After that, the temperature decreases significantly because of heat release to the chamber wall and the ambient cold air. Finally, the combustion gas leaves the hot mixing chamber through the outlet. Due to the cooling air from the three cold air inlets, the surface temperature of the modified HMC is reduced significantly, compared with that of the basic model as mentioned in previous section (Figure 4.6(a)). The numerical simulation results for the center, half of radius, and surface temperature in these cases showed good agreements with experimental results.

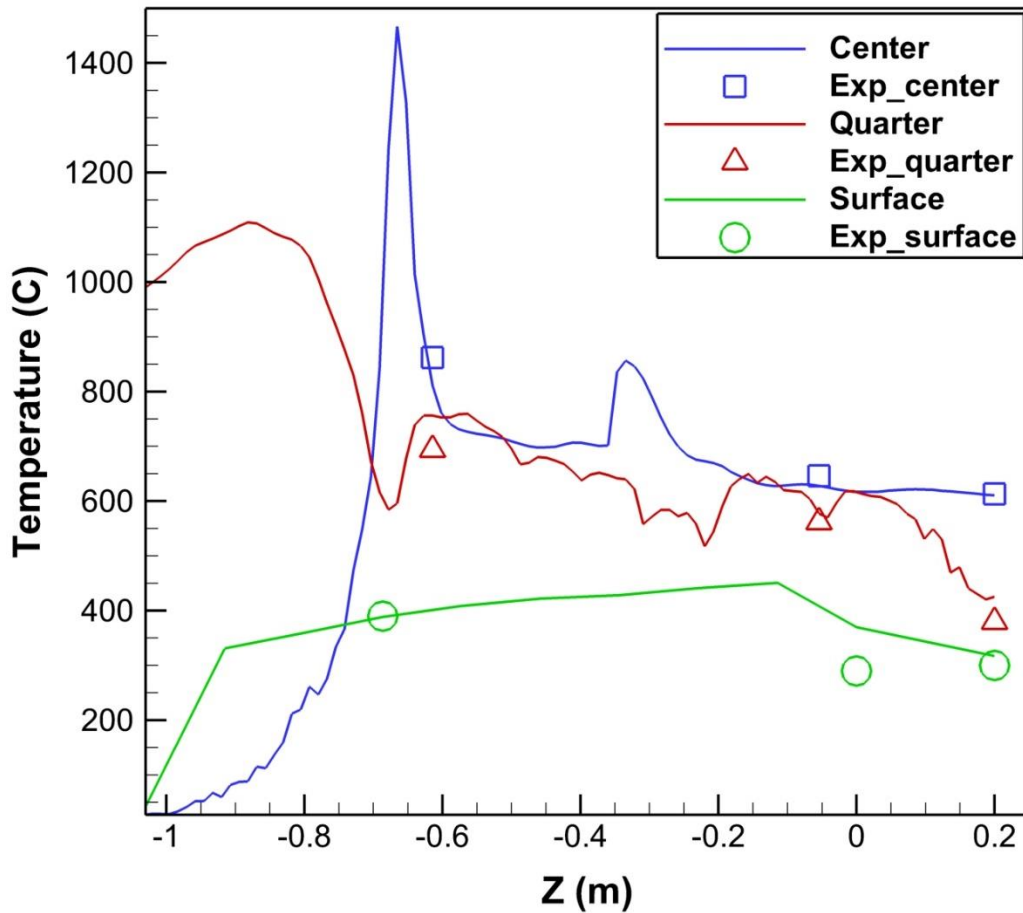


**Figure 4.9** Comparison of the temperature distribution between simulation and experimental results along HMC lengthwise direction.

#### 4.6 Summary

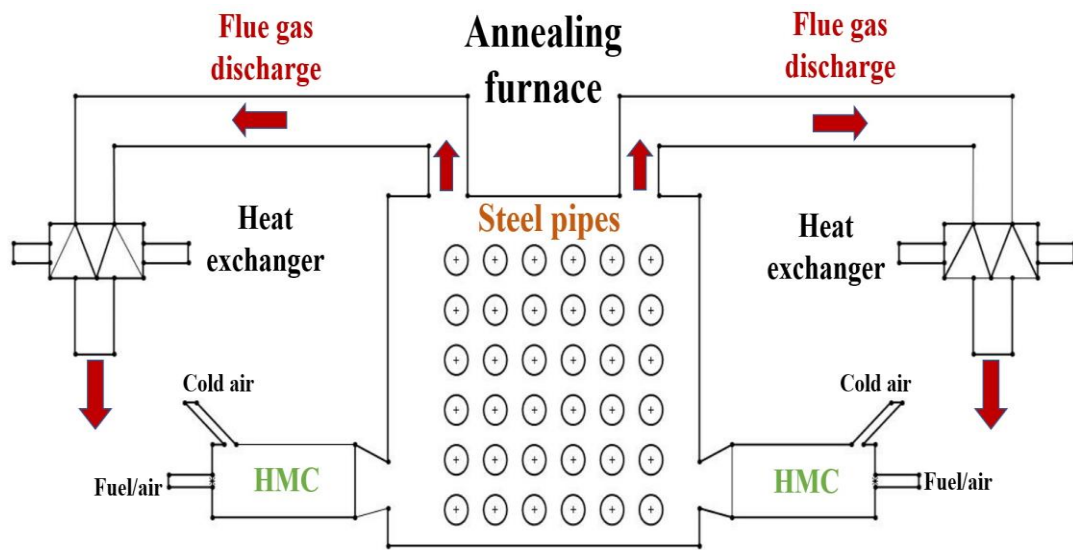
Numerical simulation and experiment have been performed to examine flow field and temperature distribution on the basic and the modified model. The basic model has higher surface temperature. On the contrary, the modified model with three cold air inlets and perforated inner cylinder showed not only uniform mixing of the cold air with the combustion gas but also a desirable cooling of the surface temperature of the HMC. Numerical simulation and experimental results showed good agreements at the center and the surface of HMC.

# **Enhancement of Mixing and Temperature Distribution of Steel Pipes inside an Annealing Furnace by Adopting a Modified Inlet Structure**

## **5.1 Introduction**

Steel annealing is a process of heat treatment that alters the properties of steel to increase its ductility and also makes it more workable. The annealing process is heating the steels arranged within furnace (heating period) to improve yield strength and holding at a constant temperature for a certain time (soaking period) to reform and enhance the grain crystalline structure then finally cooling at a predetermined rate (cooling period). By using HMC, heat source from HMC can be adjusted to meet the requirement by varying the Reynolds number of fuel/air mixture or equivalent ratio of the combustion process. The schematic diagram of the annealing process and steel pipes arranged before annealing process is shown in Figure 5.1.

The physical mechanism of the modified models was compared with the basic model, the uniform flow of the combustion gas was obtained by modifying the elbow inlets combined with the downward jet flow. Consequently, the temperature difference among a bundle of the steel pipes was reduced during annealing process.



(a)



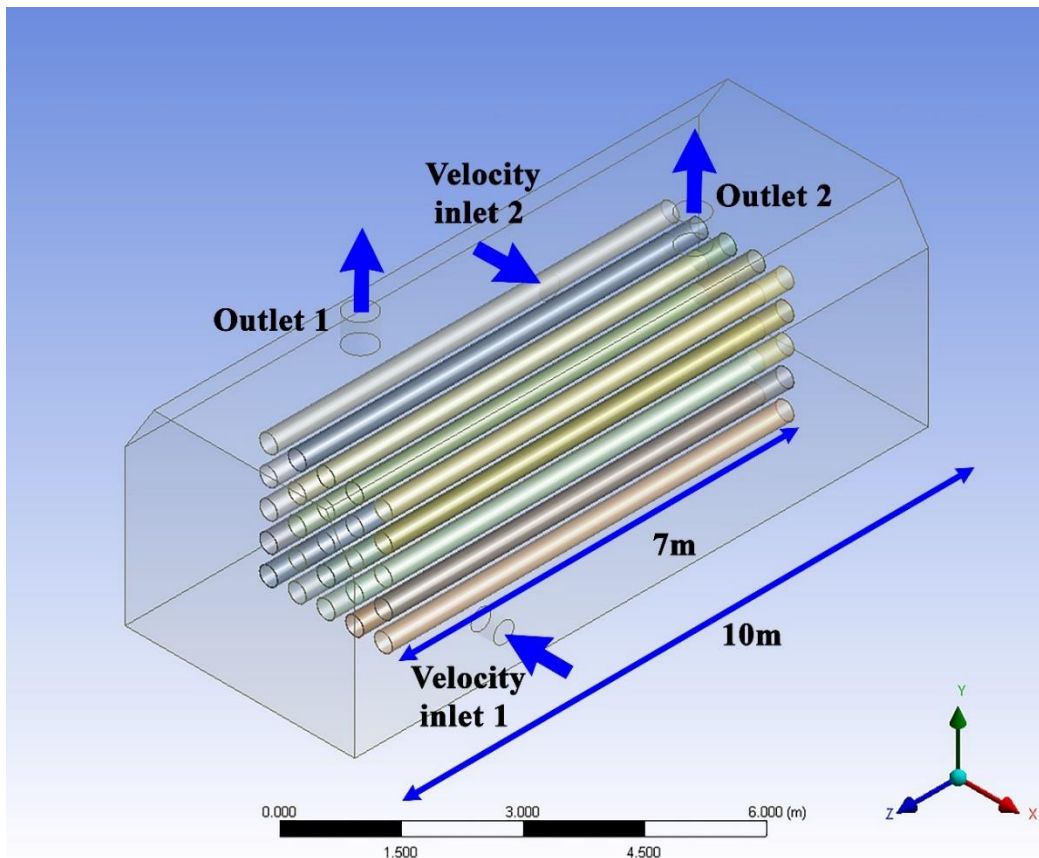
(b)

**Figure 5.1** (a) Schematic diagram of the annealing process; (b) Steel pipes to be arranged before annealing

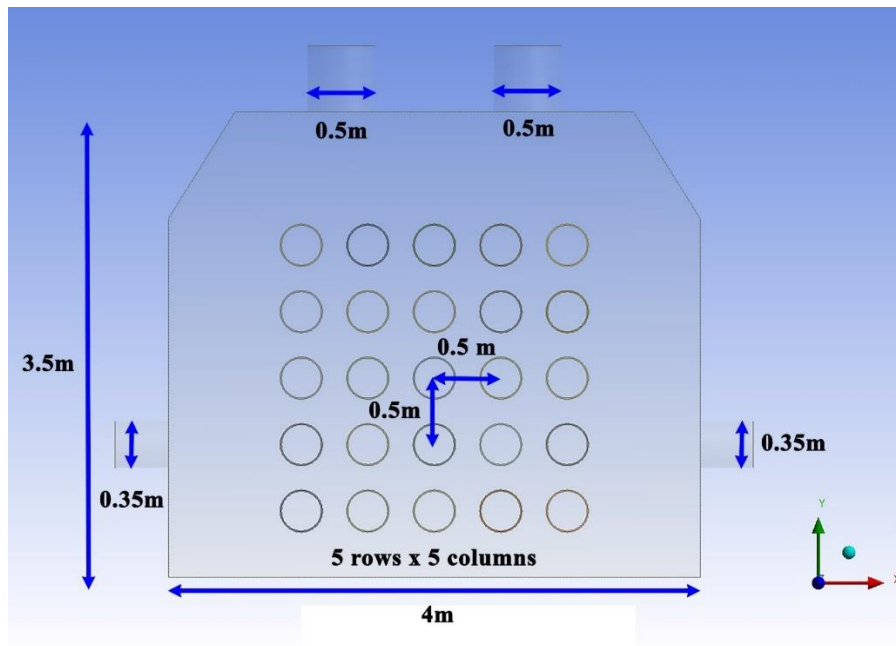
## 5.2 Annealing furnace models

### 5.2.1 Basic model

The basic model has 2 inlets and 2 outlets as shown in Figure 5.2. The dimensions of the basic annealing furnace and steel pipes is shown in Table 5.1. The furnace has the height, width and length of 3.5 m, 4 m and 10 m, respectively. The hot air inlet diameter is 0.35 m and the outlet diameter is 0.5m. Steel pipes arranged inside the furnace have the inner and outer diameter and the length of 0.3 m, 0.32 m, and 7 m, respectively. There are 5 rows and 5 columns of steel pipes arranged in the furnace. The horizontal and vertical distance of the pipes are 0.5 m as shown in Figure 5.2(b).



(a)



(b)

**Figure 5.2** The basic model with dimensions; (a) 3D view; (b) front-view

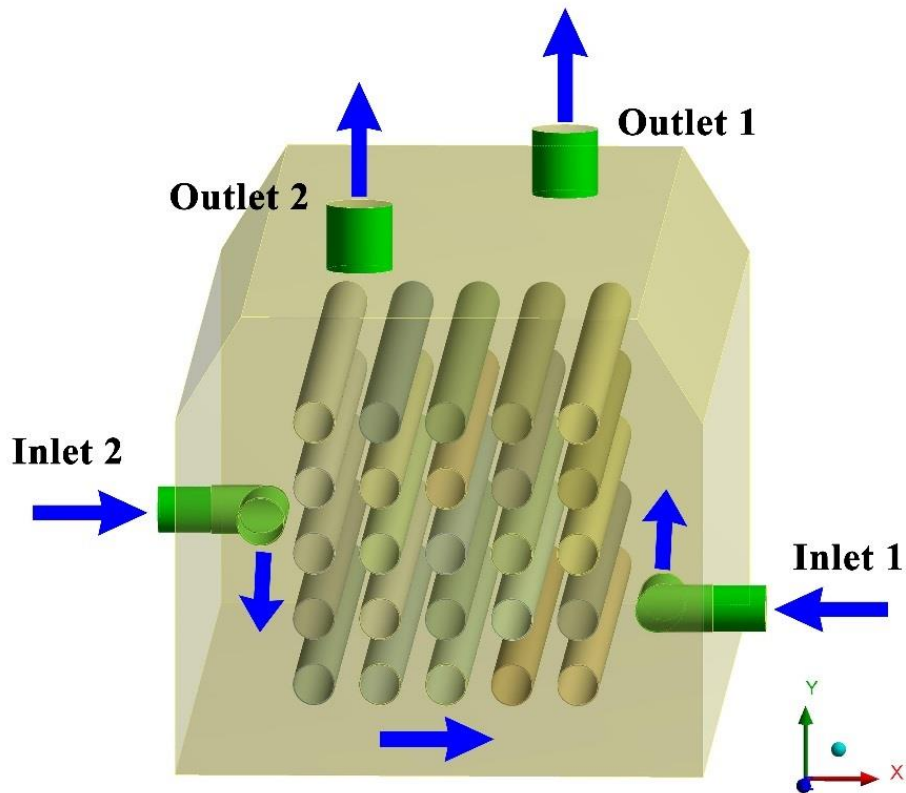
**Table 5.1.** Dimensions of the basic annealing furnace and steel pipes

Parameters	Value
Inlet diameter	0.35 m
Outlet diameter	0.5 m
Width	4 m
Height	3.5 m
Length	10 m
Outer, inner, and length of steel	0.32 m, 0.3 m, and 7 m
Rows x columns	5 x 5

### 5.2.2 Modified annealing furnace models

A new modified model is selected with the elbow inlet as shown in Figure 5.3. The main objective is that the elbow inlet with vertically inclined angle generates the

swirl flow in horizontal direction and also well-mixed flow in vertical direction within the annealing furnace to improve the uniform temperature distribution inside the furnace than the basic model. The three kinds of the inclined angle of the elbow inlet of 0 degrees, 30 degrees and 45 degrees are selected to optimize the minimum temperature difference of steel pipes in the annealing furnace as displayed in Figure 5.4. Larger inlet angle than 45 degrees is not considered in this calculation. This is because the inlet hot flow impinges on the bottom surface of the annealing furnace and thus it results in the undesirable formation of swirling flow inside the furnace.



(a)

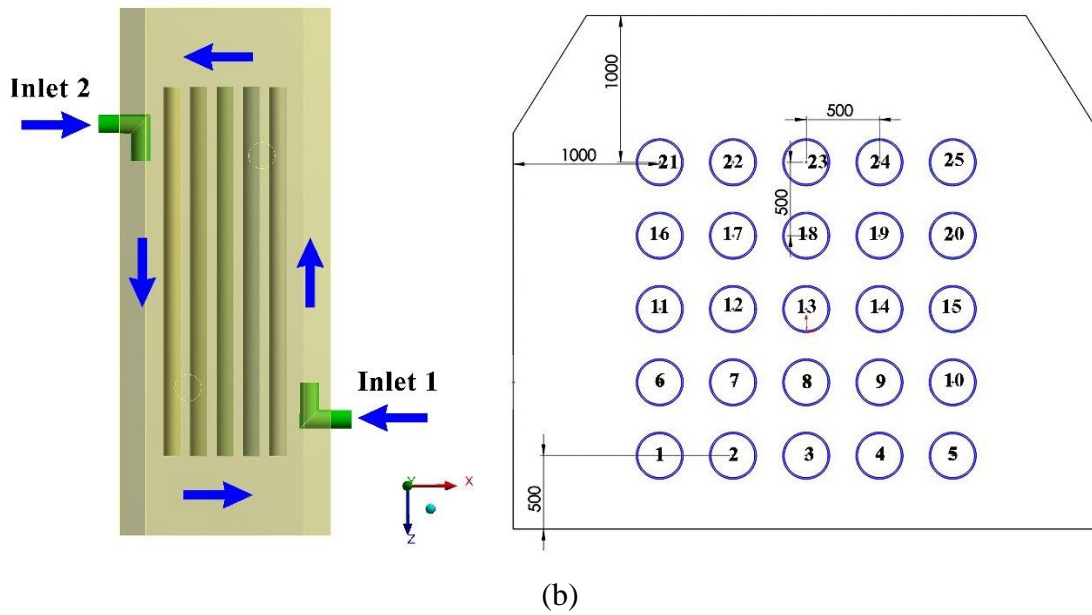


**Figure 5.3** The modified model (a) 3D view; (b) Top and front view

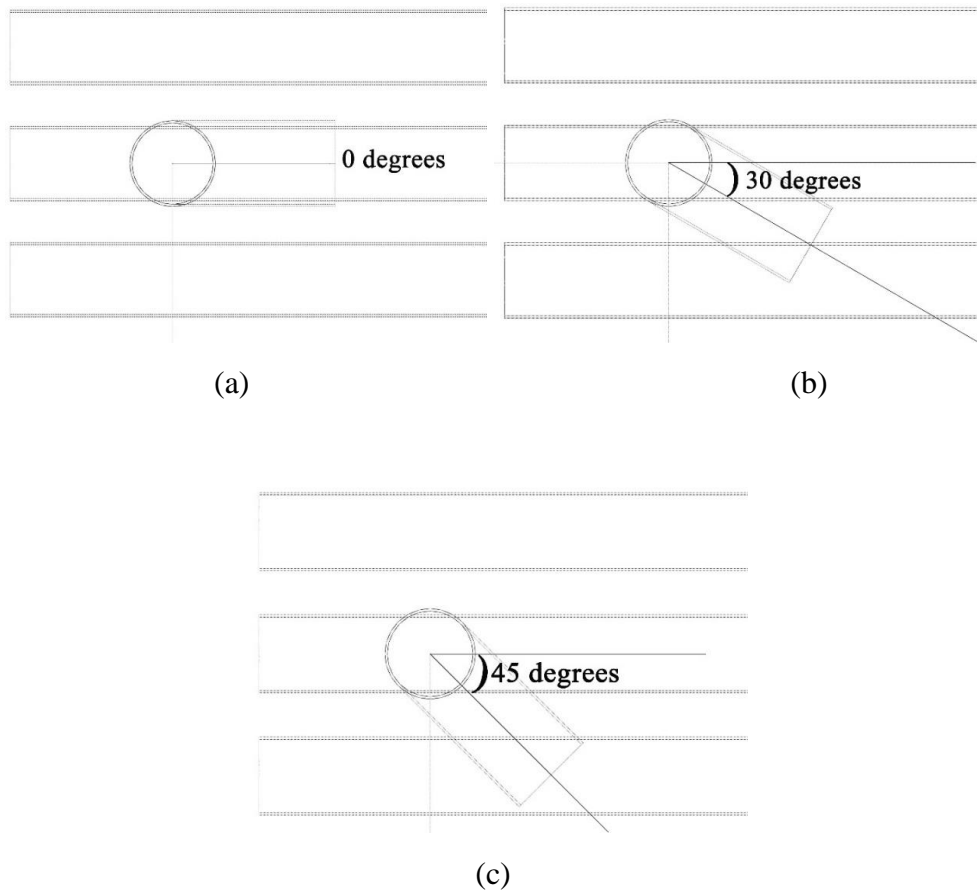


**Figure 5.4** Three kinds of the angle of elbow inlet; (a) 0 degrees, (b) 30 degrees and (c) 45 degrees

### 5.3 Mathematical model and boundary conditions

#### 5.3.1 Mathematical model

The governing equations of continuity, momentum, turbulent kinetic energy and dissipation energy model are utilized as follows:

Continuity equation:

$$\frac{\partial \rho}{\partial t} + \nabla \cdot (\rho \vec{u}) = 0 \quad (5.1)$$

Momentum equation:

$$\frac{\partial (\rho \vec{u})}{\partial t} + \nabla \cdot (\rho \vec{u} \vec{u}) = -\nabla p + \nabla \cdot (\mu + \mu_t) \left[ \left( \nabla \vec{u} + \nabla \vec{u}^T \right) - \frac{2}{3} \nabla \cdot \vec{u} I \right] + \rho f_i \quad (5.2)$$

Energy equation:

$$\frac{\partial}{\partial t} (\rho E) + \nabla \cdot (\vec{u} (\rho E + p)) = \nabla \cdot (k \nabla T) + S_h \quad (5.3)$$

The turbulence kinetic energy  $k$  and the rate of its dissipation  $\varepsilon$  are obtained from the following transport equations:

$$\frac{\partial k}{\partial t} + \frac{\partial}{\partial x_i} (\rho k u_i) = \frac{\partial}{\partial x_j} \left[ \left( \mu + \frac{\mu_t}{\sigma_k} \right) \frac{\partial k}{\partial x_j} \right] + G_k + G_b - \rho \varepsilon \quad (5.4)$$

$$\frac{\partial \varepsilon}{\partial t} + \frac{\partial}{\partial x_i} (\rho \varepsilon u_i) = \frac{\partial}{\partial x_j} \left[ \left( \mu + \frac{\mu_t}{\sigma_\varepsilon} \right) \frac{\partial \varepsilon}{\partial x_j} \right] + C_{1\varepsilon} \frac{\varepsilon}{k} (G_k + C_{3\varepsilon} G_b) - C_{2\varepsilon} \rho \frac{\varepsilon^2}{k} \quad (5.5)$$

Turbulent viscosity is modelled as:

$$\mu_t = \rho C_\mu \frac{k^2}{\varepsilon} \quad (5.6)$$

The production of turbulence kinetic energy is defined as:

$$G_k = -\overline{\rho u_i' u_j'} \frac{\partial u_j}{\partial x_i} \quad (5.7)$$

The generation of turbulence due to buoyancy is given by

$$G_b = \beta g_i \frac{\mu_t}{Pr_t} \frac{\partial T}{\partial x_i} \quad (5.8)$$

where,  $Pr_t$  is the turbulent Prandtl number. In the standard k- $\epsilon$  model, ANSYS FLUENT adopt the default value of  $Pr_t = 0.85$ , and  $g_i$  is the component of the gravitational vector in the  $i_{th}$  direction.

The coefficient of thermal expansion,  $\beta$ , is defined as follows:

$$\beta = -\frac{1}{\rho} \left( \frac{\partial \rho}{\partial T} \right)_p \quad (5.9)$$

$$C_{3\epsilon} = \tanh \left| \frac{v}{u} \right| \quad (5.10)$$

where  $v$  is the component of the flow velocity parallel to the gravitational vector and  $u$  is the component of the flow velocity perpendicular to the gravitational vector. In this way,  $C_{3\epsilon}$  will become 1 for buoyant shear layers for which the main flow direction is aligned with the direction of gravity. For buoyant shear layers that are perpendicular to the gravitational vector,  $C_{3\epsilon}$  will become zero.

The default values for the model constants  $C_{1\epsilon}$ ,  $C_{2\epsilon}$ ,  $C_\mu$ ,  $\sigma_k$  and  $\sigma_\epsilon$  are  $C_{1\epsilon} = 1.44$ ,  $C_{2\epsilon} = 1.92$ ,  $C_\mu = 0.09$ ,  $\sigma_k = 1.0$ , and  $\sigma_\epsilon = 1.3$ .

### 5.3.2. Boundary conditions and grid independence checking

The transient and steady state numerical simulations were performed by ANSYS FLUENT 18.2 software based on finite volume discretization. The boundary condition and numerical method for the basic and modified models are shown in Table 5.2. The inlet condition was set as velocity inlet of the inlets of annealing furnace. Ambient pressure outlet boundary condition was set at the outlet of annealing furnace. No-slip wall boundary condition was set for the outer walls. The standard k- $\epsilon$  turbulence model was used in this study. The SIMPLE algorithm was adopted for coupling of pressure and velocity in this simulation. For more accuracy, the Second-Order Upwind Scheme was selected for the spatial discretization. The convergence criterion was set up  $10^{-4}$  for momentum, continuity, turbulence equations, and  $10^{-6}$  for energy equation. Grid independence checking was performed on the grid amount of 4.2 million, 3.5 million, and 1.9 million. The temperature difference among the steel pipes did not change so much between two kind of grid amounts of 4.2 million and 3.5 million. Therefore, to reduce the computing time, the grid amount of 3.5 million was selected in this study as shown in Figure 5.5.

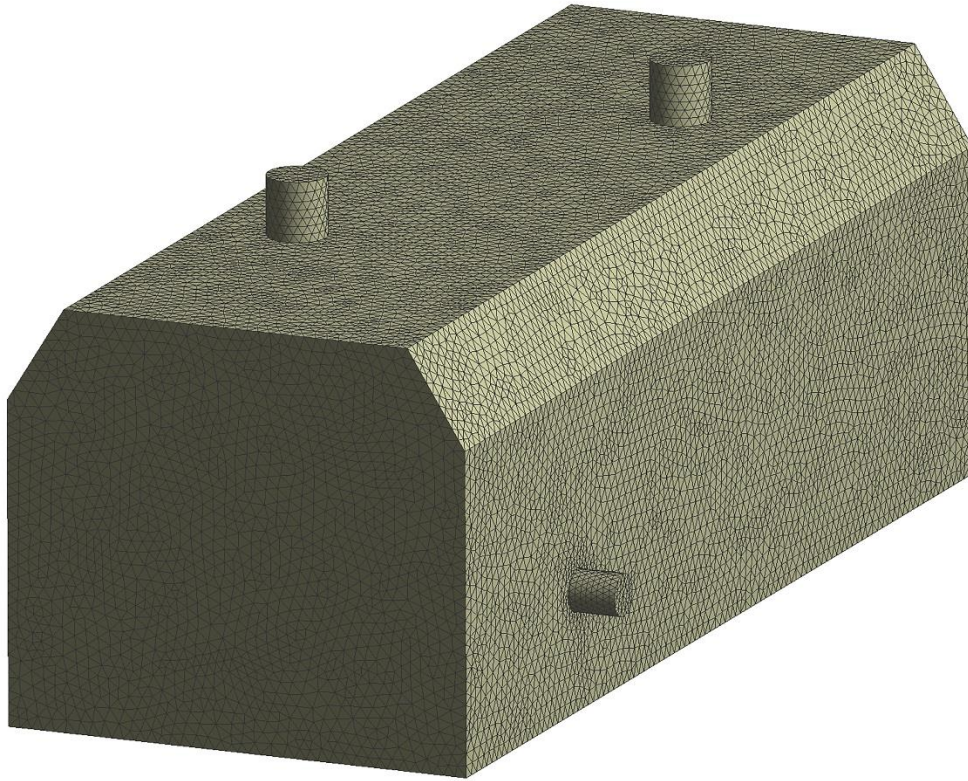


**Figure 5.5** Three dimensional mesh model

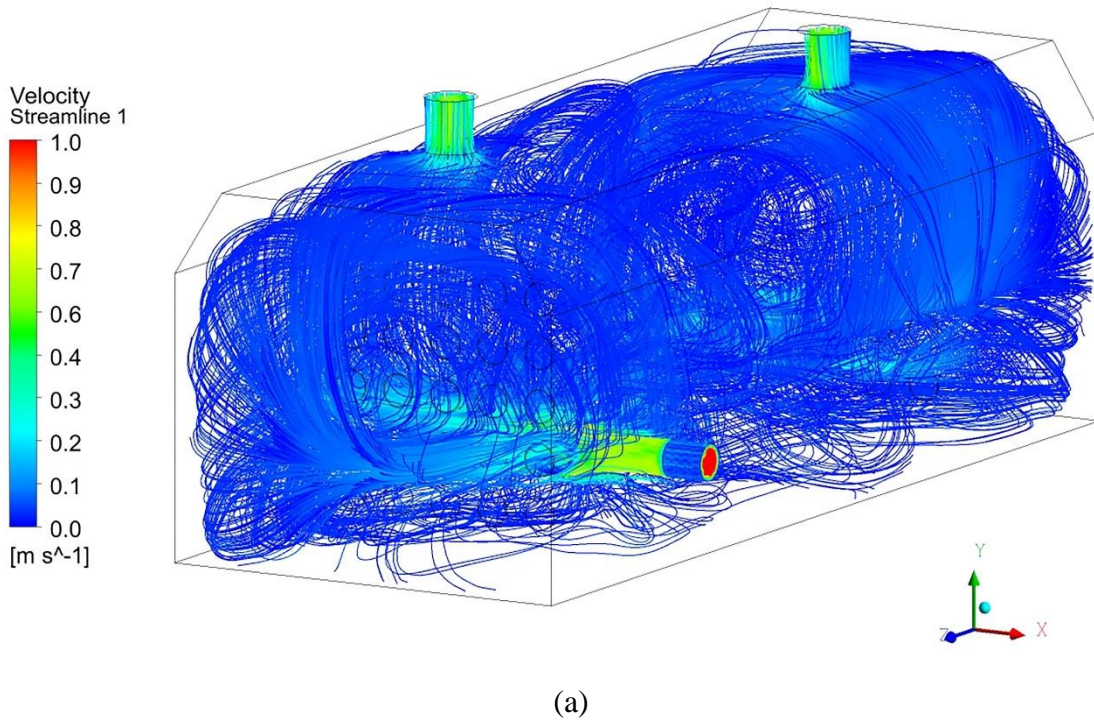
**Table 5.2** Boundary conditions and method

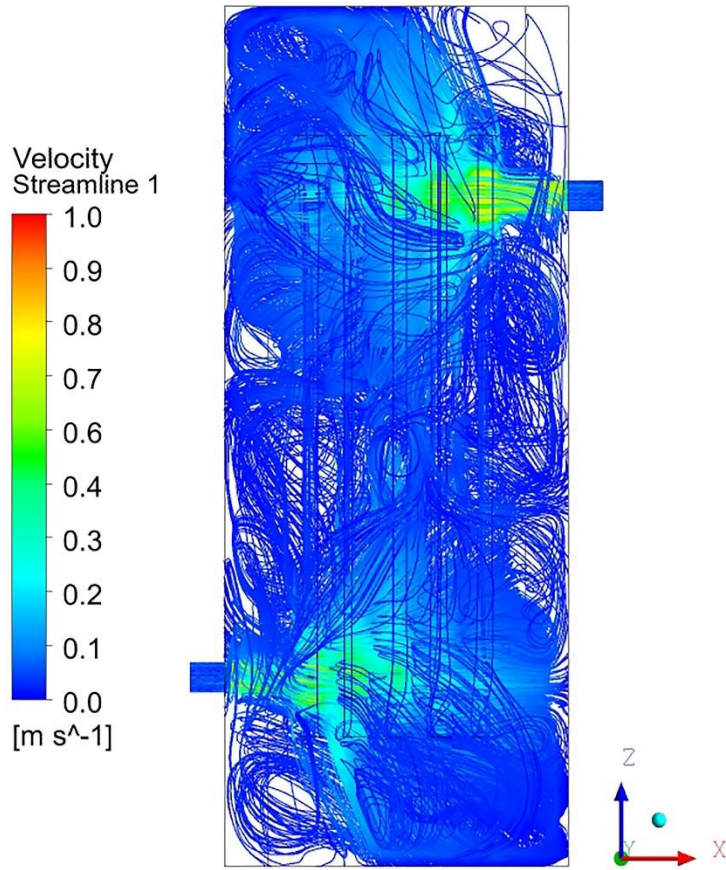
<b>Parameters</b>	<b>Value/method</b>
Velocity inlet	0.1 – 1 m/s
Temperature inlet	1000 K (727°C)
Pressure outlet	0 Pa
Turbulent model	Standard k- $\epsilon$
Annealing time	20005 second

## 5.4 Results and discussions

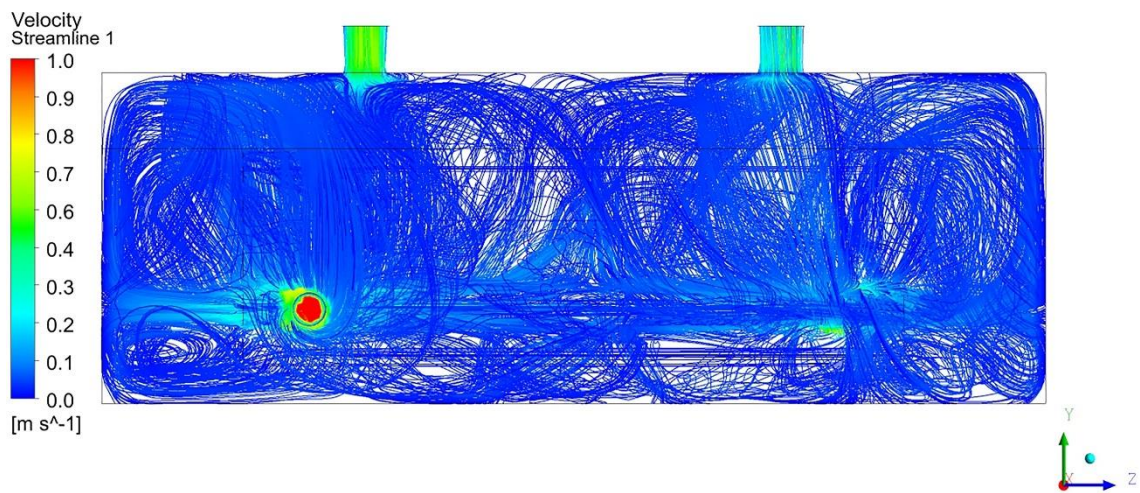
### 5.4.1 Flow field and steel pipe temperature distribution of the basic model

The flow field within the basic furnace model is shown in Figure 5.6. The hot inlet flow transfers heat to the steel pipes which are arranged within the annealing furnace. Convection and radiation heat loss also occur in the furnace walls. The hot flow moves around the outer and inner of the steel pipes and then exits through the two outlets at the top of the basic furnace as shown in Figure 5.6(a). Due to the perpendicular inlet flow, the hot flow impinges on some pipes which are located at outer positions. Hence, the heat from the hot flow transfers to this area of steel pipes more than the other zone. Moreover, the flow field distributions inside the furnace are non-uniform as shown in Figure 5.6(b) and 5.6(c). Consequently, the temperature difference among the steel pipes is higher during the steel annealing process.





(b)



(c)

**Figure 5.6** Flow field distribution within the basic model; (a) 3D view; (b) bottom view; (c) side view.

The temperature contour distribution of the flow field at the top view within the annealing furnace is shown in Figure 5.7. High temperature flow velocity from the inlet reduces gradually when impinging on the first and then the second pipe rows. The non-uniform of flow temperature distribution can also be observed in the Figure 5.7(b) due to the hot flow non-uniformity distribution inside the furnace. Consequently, the parts where the fluid flow impinges have high temperature than the others. Therefore, the temperature difference among a bundle of steel pipes also increases.

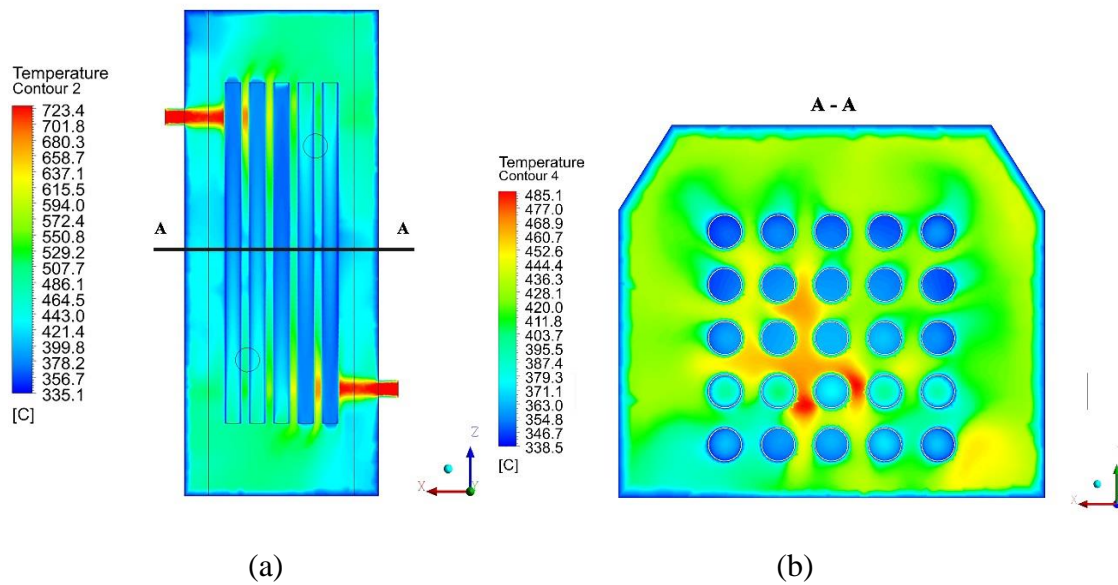


**Figure 5.7** Flow temperature distribution within the basic furnace model.

The steel pipe temperature distribution within the basic model is shown in Figure 5.8. Due to the perpendicular inlet direction, the hottest temperature of the steel pipes located at the position which faces to the hot flow inlet. The temperature difference of steel pipes is around 55.4°C. This is because the flow field distribution is not uniform and the temperature difference of the steel pipes is high.

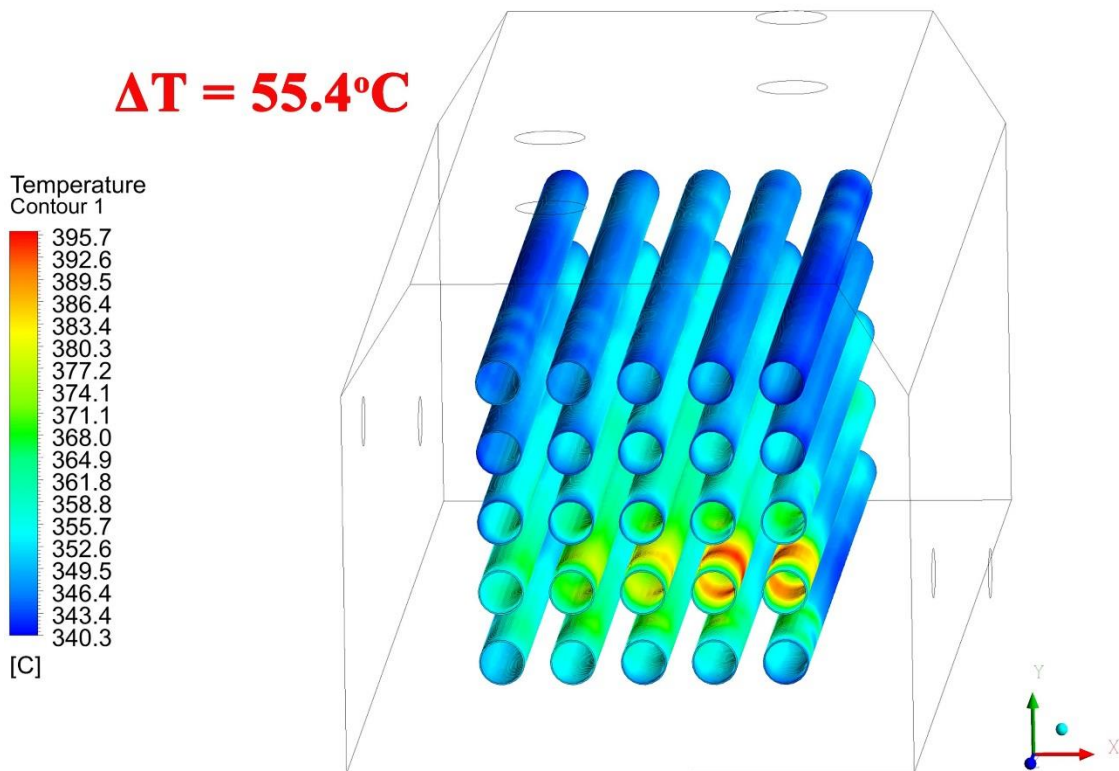


**Figure 5.8** Steel pipe temperature distribution within the basic model

#### 5.4.2 Validation for the three modified models

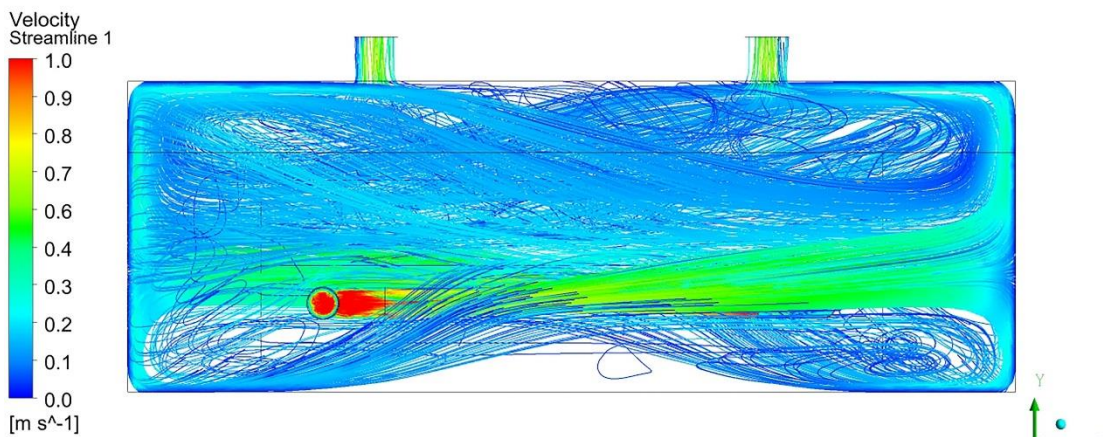
To validate the CFD simulation results, the flow field behavior in this study is compared with that of Han et al. [78] who performed a study on a rotational flow of a fan. The advantage of the present models can neglect the power consumption by the rotational fan but still create swirl flow from two downward jet inlets to improve the flow uniformity. On the other hand, Prieler et al. [94] performed the baffle angle inlets (only upward and downward inlet but without swirl flow inside the furnace). The results from Prieler et al. [94] revealed that the temperature difference obtained from the baffle angle inlet flow achieved 50°C inside the furnace.

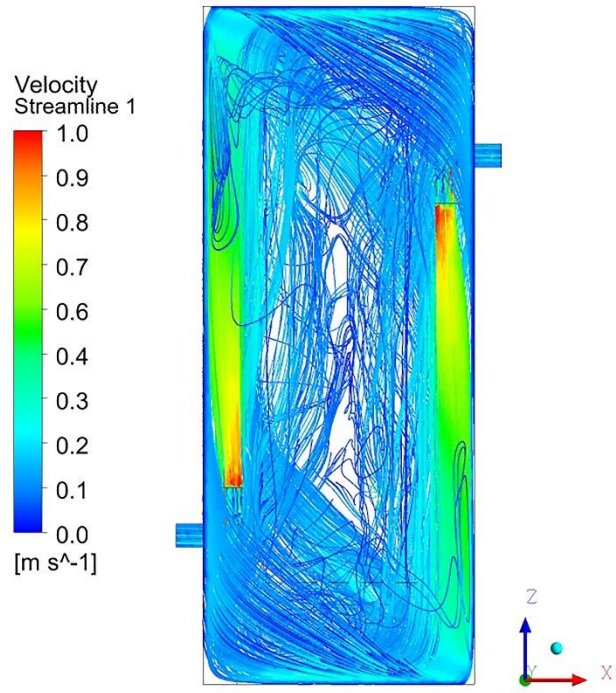
In the present study, by adopting elbow and downward jet configurations to generate the swirl and jet flow, the flow temperature difference value for model 1 (0 degrees) of 27°C, model 2 (30 degrees) of 23°C, and model 3 (45 degrees) of 30°C inside the annealing furnace. Moreover, the more advance in this study than that of Prieler et al. [94] is to investigate simultaneously flow field and steel pipes temperature to meet the goal of the temperature uniformity of steel pipes. Well-mixed uniform flow can reduce the temperature difference of the bundle of steel pipes within the furnace. Consequently, the novelty of three modified models in the present study is to combine two important points of generating the swirl flow by the elbow inlets (without electric power consumption by driving fan) and enhancing the flow and temperature uniformity

by the inclined jets (generate downward jet flow followed by buoyancy flow), but Han et al. [78] and Prieler et al. [94] had not mentioned.

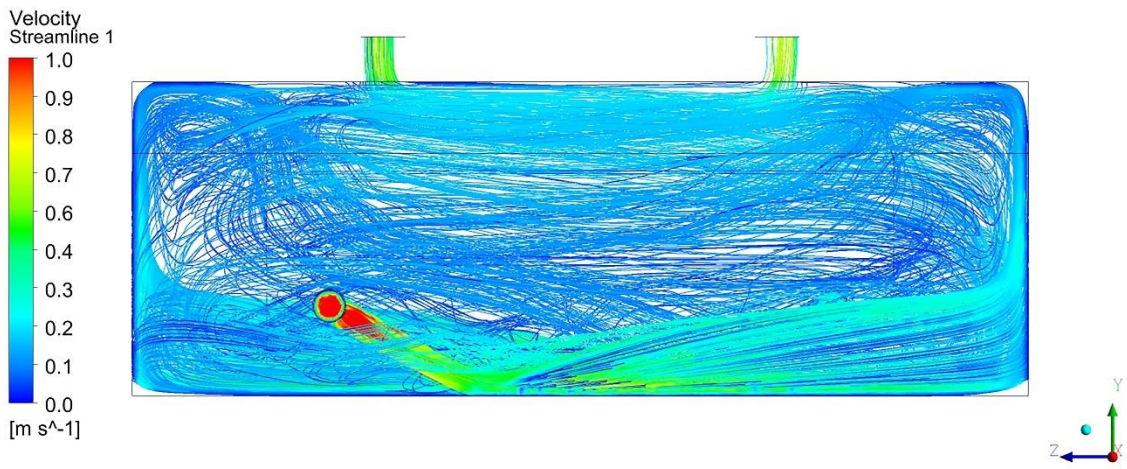
### 5.4.3 Flow fields and steel pipes temperature distribution of the modified models

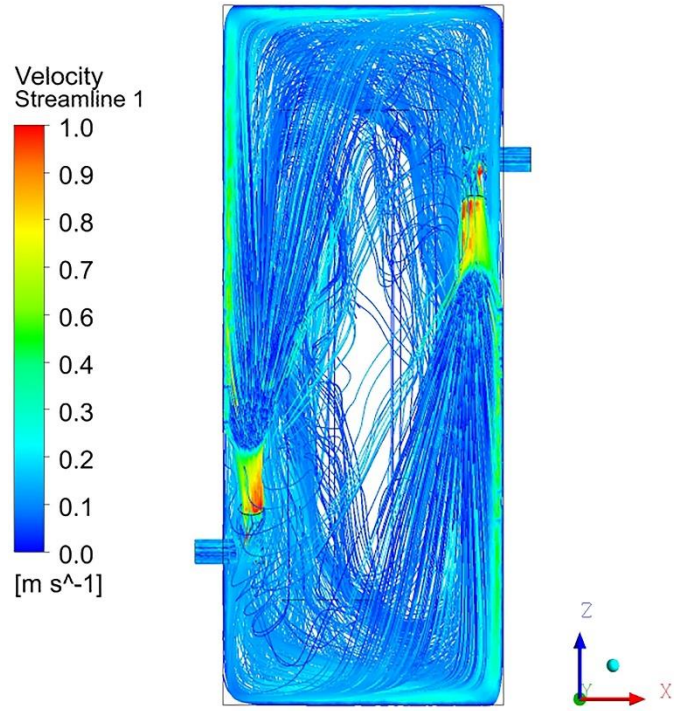
Velocity streamline at the side and bottom views of three kinds of the elbow inlet angle is shown in Figure 5.9. All modified models generate the swirl flow within the annealing furnace as shown clearly in the bottom view of the furnace. This leads to a uniform flow distribution inside the furnace. Moreover, the hot flow could move through every pipe arranged within the furnace easily to transfer heat to pipes. Therefore, temperature difference among steel pipes for all modified models is expected to reduce much more than that for the basic model. In the side view, for the elbow inlet angle of 0 degrees, the hot flow impinges on the back side of the furnace and then combines with the hot flow from the other side to generate the swirl flow inside the furnace. Although the swirl flow is generated in the furnace, there are some regions lack of filling by the hot flow. This is because the inlet port location has a certain height from the bottom of the furnace and the hot flow tends to move up to the top of the furnace due to the buoyancy effect. Consequently, some steel pipes located below the discharge jet line from the inlet elbow have lower temperature than the others. This problem can be solved by a certain downward elbow angle inlet. The flow field for the angle of 30 degrees has better mixing and distribution than that of 45 degrees. This is because the flow field with a high angle inlet tends to impinge on the bottom of the furnace and it may interfere with the uniform flow distribution inside the furnace. By adopting swirl flow, flow field distribution could be uniform inside the annealing furnace. The flow field behavior in this study coincides well with that of Han et al. [78], who performed a study on a rotational flow of a fan.



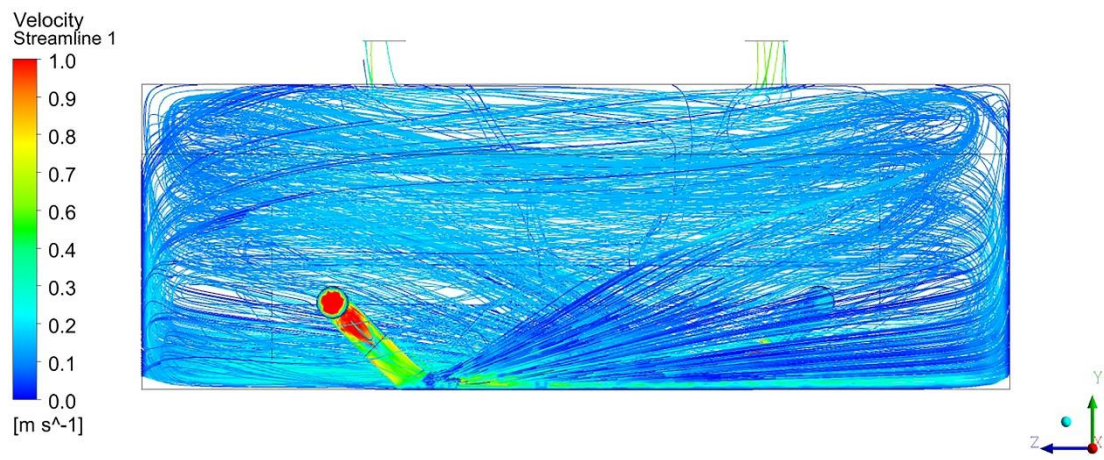


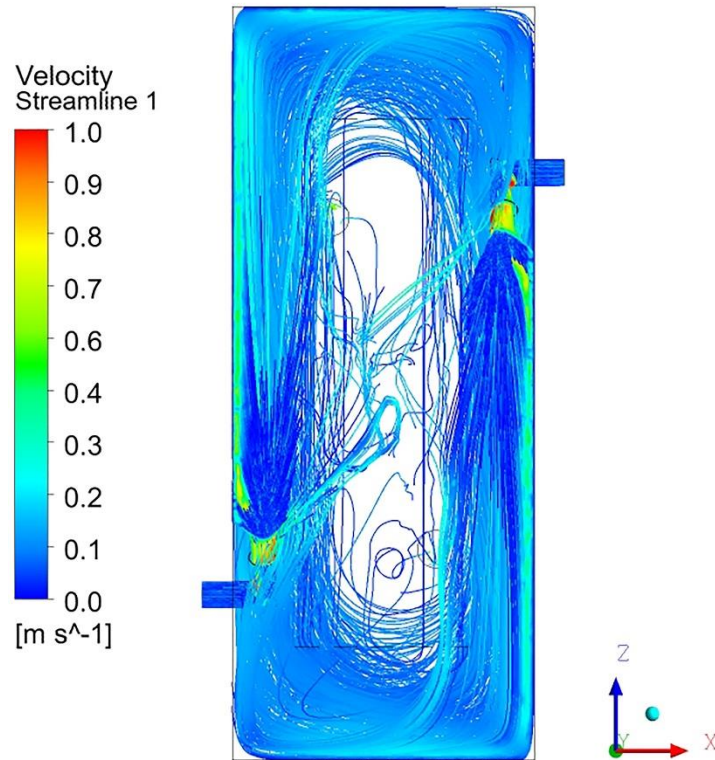
(a)





(b)

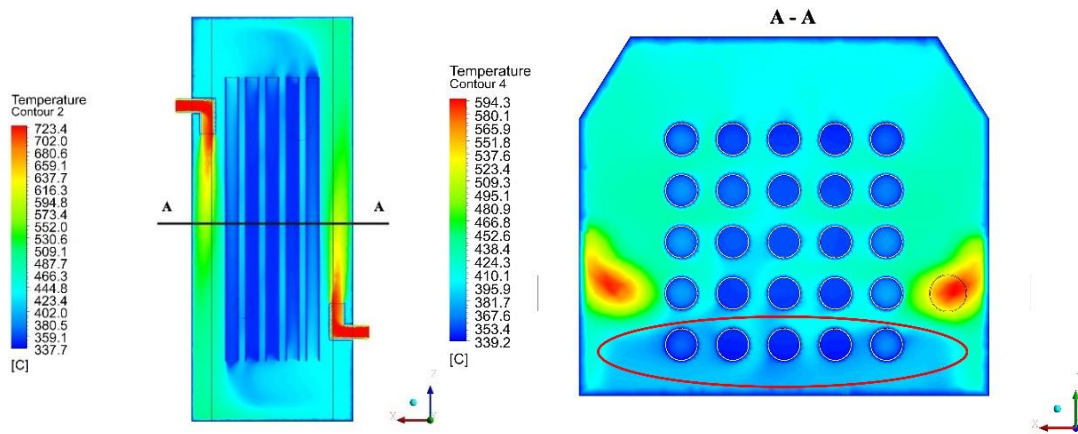




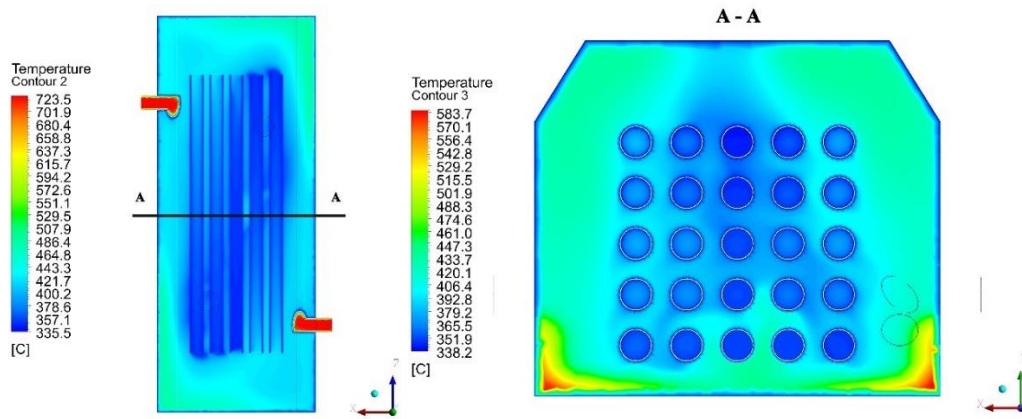
(c)

**Figure 5.9** Velocity streamline at the side and bottom views of three kinds of the elbow inlet angle; (a) 0 degrees, (b) 30 degrees and (c) 45 degrees.

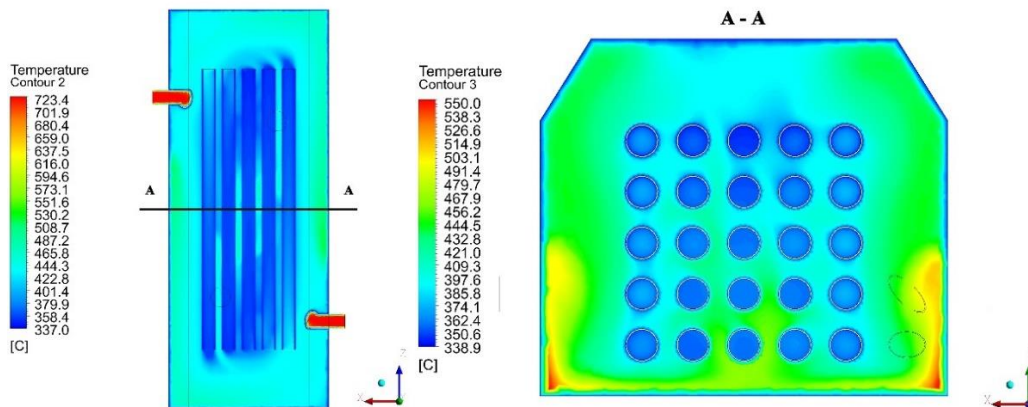
Flow field and temperature distribution at the inlet cross-section plane view of three kinds of the elbow inlet angle of 0 degrees, 30 degrees and 45 degrees are shown in Figure 5.10. Due to the elbow inlet, hot flow temperature decreases along the elbow direction. It avoids direct impinging on the steel pipes. Therefore, high temperature difference problem among steel pipes was solved in all the modified models. The model 1 with elbow inlet angle of 0 degrees showed the cold flow located at the bottom of the furnace due to the buoyancy effect and hot flow tends to go up to the top of the furnace. This problem can be solved by the models with downward inlet flow. The model 2 with downward elbow inlet angle of 30 degrees showed most uniform temperature. This is due to the fact that the elbow inlet with the downward angle of 30 degrees generates the swirl flow horizontally and the downward jet flow followed by the upward buoyancy flow vertically, and thus the whole flow inside the furnace becomes the well-mixed and uniform flows. Consequently, the temperature difference among the steel pipes is the smallest among the others downward angle as shown in Figure 5.11. By adopting elbow angle inlet with the downward jet flow, the flow temperature distribution could enhance uniform as well as reduce temperature difference inside the furnace than the results performed by Prieler et al. [94].



(a)



(b)



(c)

**Figure 5.10** Flow field and temperature distribution of the flow at the inlet cross-section plane view of three kinds of the elbow inlet angle; (a) 0 degrees, (b) 30 degrees and (c) 45 degrees.

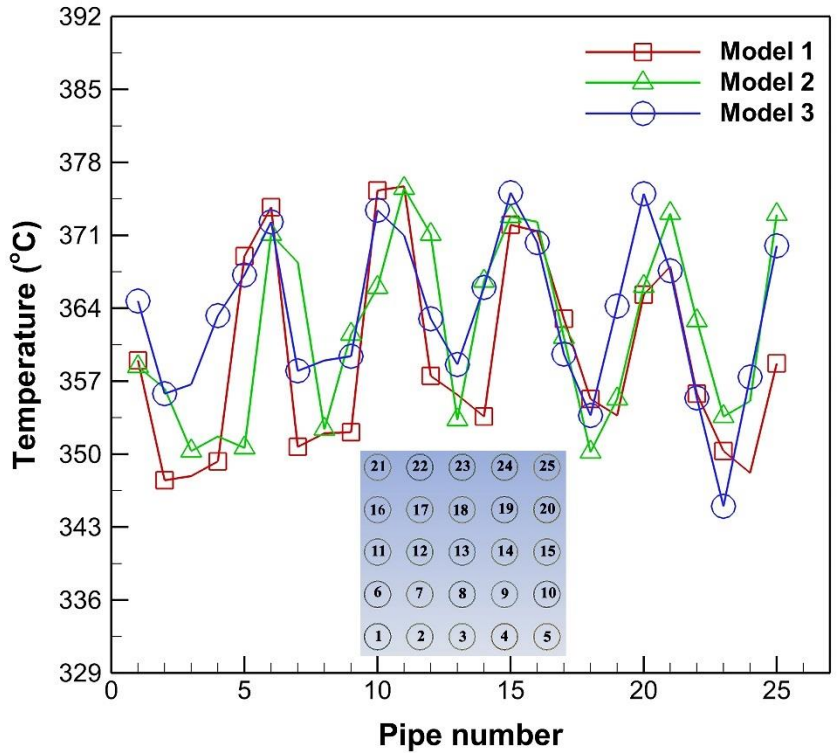
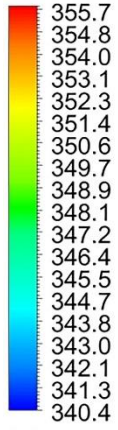


**Figure 5.11.** Flow temperature at every pipe position of the three modified models

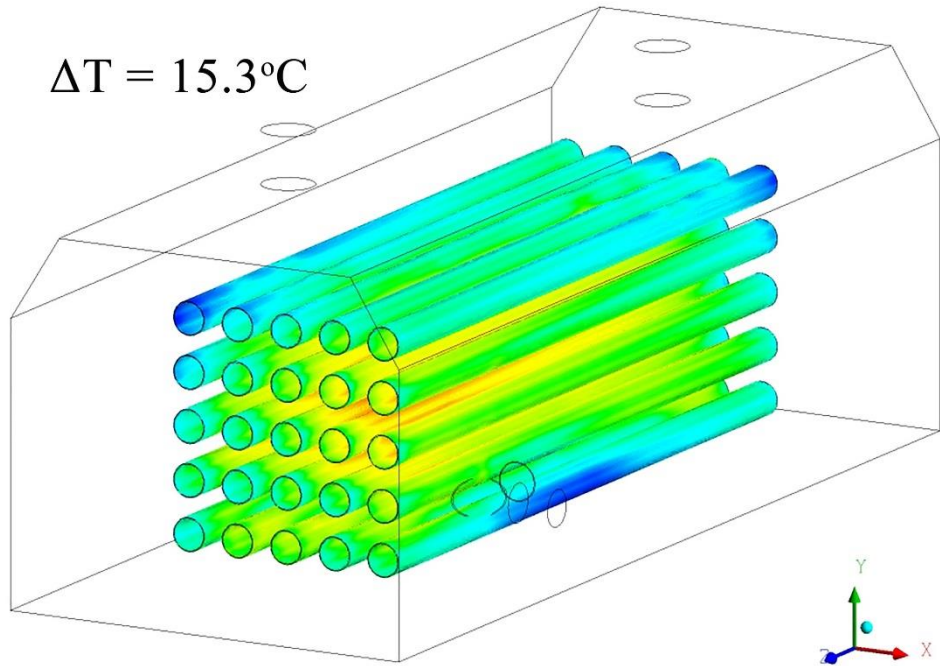
Temperature distribution of steel pipes for annealing process is shown in Figure 5.12. The temperature difference for the elbow inlet with the downward angle of 0 degree, 30 degrees, and 45 degrees showed 15.3°C, 13°C, and 23.6°C, respectively. Trends of the temperature distribution according to variations of the downward inlet angle are similar to those of the velocity streamline behavior as explained in the previous section. The downward angle of 30 degrees showed the lowest temperature difference among the steel pipes. Around this angle, it could be considered as the optimized downward jet angle for this modified annealing furnace. The percentage reduction of temperature difference between the three modified models and basic model are shown in Table 5.3.

Temperature  
Contour 1



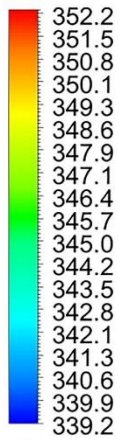
[C]

$\Delta T = 15.3^{\circ}\text{C}$



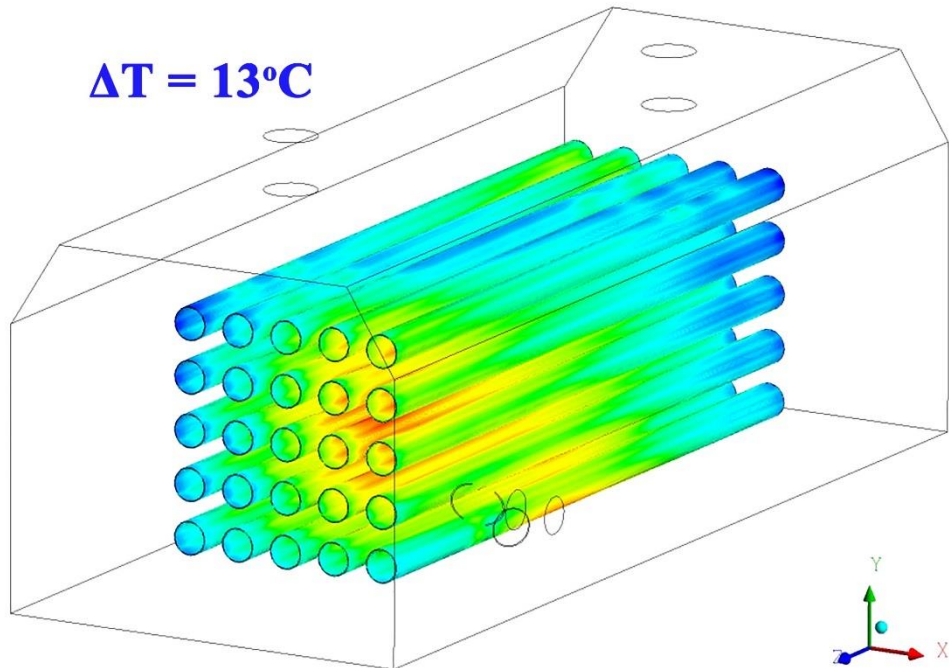
(a)

Temperature  
Contour 1



[C]

$\Delta T = 13^{\circ}\text{C}$



(b)

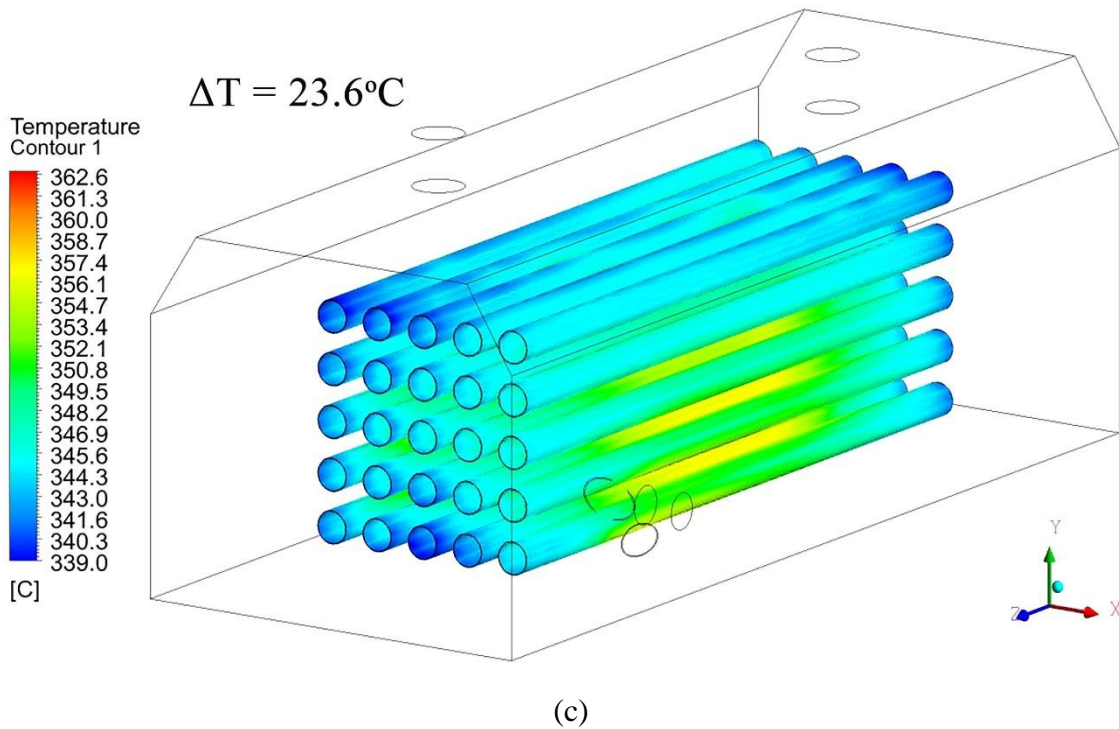


**Figure 5.12** Temperature distribution of steel pipes for annealing process; (a) 0 degrees, (b) 30 degrees and (c) 45 degrees.

**Table 5.3** Percentage reduction of temperature difference among steel pipes between the three modified models and basic model

Models	Value
Model 1 (0 degrees)	72.4%
<b>Model 2 (30 degrees)</b>	<b>76.5%</b>
Model 3 (45 degrees)	57.4%

## 5.5 Effect of Reynolds number at the inlet and the horizontal and vertical steel spacing on the steel temperature difference among steel pipes

### 5.5.1 Effect of Reynolds number at the inlet on the temperature difference among the steel pipes

Since the model 2 with the downward elbow inlet angle of 30 degrees has the lowest temperature difference of the bundle of steel pipes, the model 2 has been selected to investigate the effect of Reynolds number at the inlet, the horizontal and vertical steel spacing on the temperature difference among the steel pipes. And also the model 2 has been utilized to study the transient simulation to consider the behavior of steel temperature during the annealing process. The temperature difference of a bundle of steel pipes within annealing furnace as a function of Reynolds number is displayed in

Figure 5.13. The temperature difference increased as Reynolds number increased. The phenomena also coincide with those of Prieler et al. [94]. This is because high speed fluid flows to impinge on the steel pipes during the annealing process causes high temperature difference of a bundle of steel pipes. As Reynolds number increases from 2400 to 24000, the temperature difference increases from 3°C to 13°C.

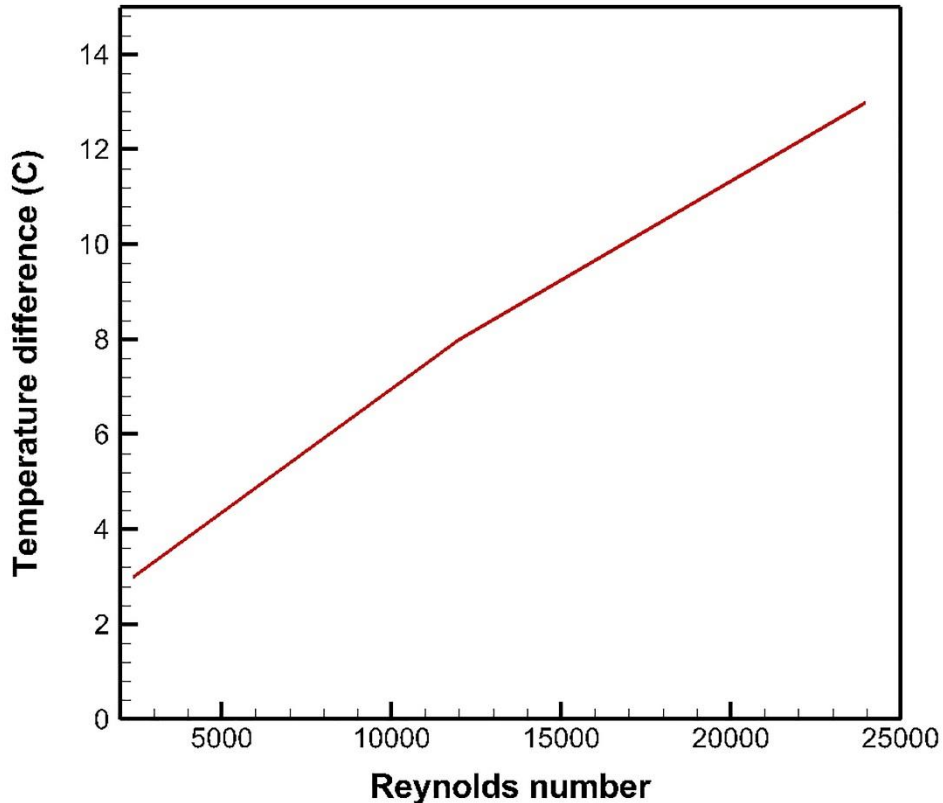


**Figure 5.13** Temperature difference of the bundle of steel pipes as a function of Reynolds number for model 2 with the elbow inlet angle of 30 degrees.

### 5.5.2 Effect of horizontal steel spacing on steel temperature difference among the steel pipes

The temperature difference among the steel pipes as a function of horizontal spacing is shown in Figure 5.14. In this case, the pipe diameter and the distance between the inlet and the first pipe are kept constant. The number of steel pipes is varied if the horizontal spacing is changed. Higher temperature difference occurred at smaller spacing and lower temperature difference occurred at larger spacing. This is due to the fact that larger spacing or smaller number of pipes leads to enough mixing of the flow inside the furnace. On the other hand, smaller spacing or larger number of pipes hinders enough mixing and leads to smaller flow velocity. In this case, the minimum

temperature difference of a bundle of steel pipes is around 9°C at the horizontal spacing,  $S_h/d$  of 3.13.

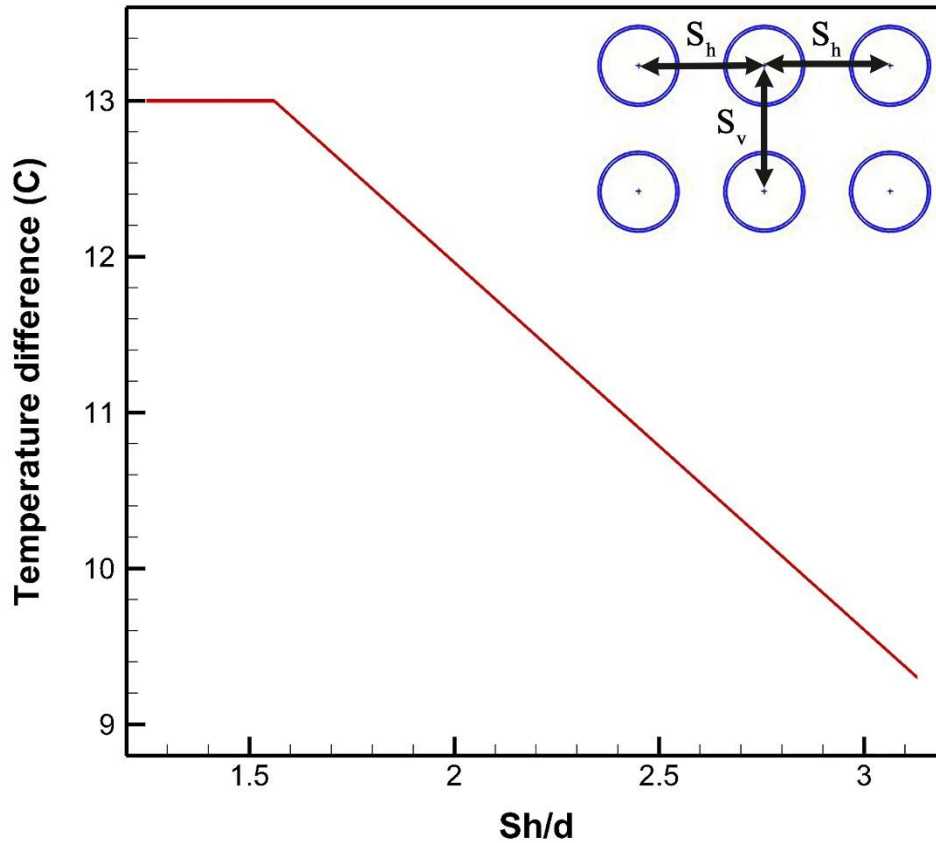


**Figure 5.14** Temperature difference of steel pipes as a function of horizontal spacing to steel pipe diameter ratio at  $S_v/d = 1.56$ .

### 5.5.3 Effect of vertical steel spacing on steel temperature difference among the steel pipes

Similarly, the trends for the temperature difference of a bundle of steel pipes as a function of vertical spacing is shown in Figure 5.15. The lowest temperature difference of 11°C was found at  $S_v/d$  of 3.13. It has the similar reason for the horizontal spacing case which is clearly described in the previous section. With comparing the temperature difference between the horizontal and the vertical spacing of pipes, the vertical spacing shows larger effect on the temperature distribution than the horizontal spacing as shown in Figure 5.14 and Figure 5.15. These phenomena may be caused by the swirl flow passing around a bundle of steel pipes and by lack of spacing for the hot flow passing through vertical pipes. As shown in Figure 5.15, the highest temperature difference of 16°C was found at the  $S_v/d$  of 1.25.

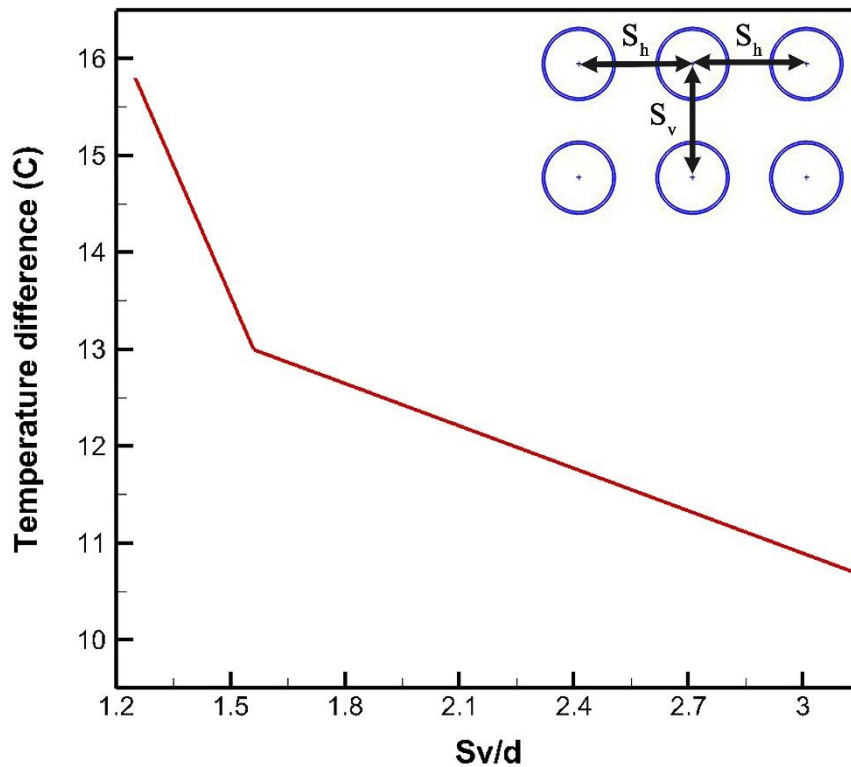


**Figure 5.15** Temperature difference of steel pipes as a function of vertical spacing to steel pipe diameter ratio at  $S_h/d = 1.56$ .

### 5.6 Unsteady state 3D simulation during annealing process

Steel pipe temperature as a function of annealing process time is displayed in Figure 5.16. Steel temperature increases rapidly at the first annealing period because the high temperature difference between the hot flow temperature of 723°C and the steel pipe temperature of 27°C causes high heat transfer from the hot inlet flow to steel pipes. Then, the steel temperature will increase slowly until steady state is reached. The temperature of steel pipes increases rapidly from 27°C to around 275°C, almost linearly from the beginning to 8000 second. Then, for the next period from 8000 second to 14000 second, the temperature gradually rises from 275°C to 350°C. Finally, the temperature increases slowly and then approaches the steady state value of 350°C, for the period from 14000 second to 20005 second. The average temperature rising rate of a bundle of steel pipes during around six hours is 58°C/hr.

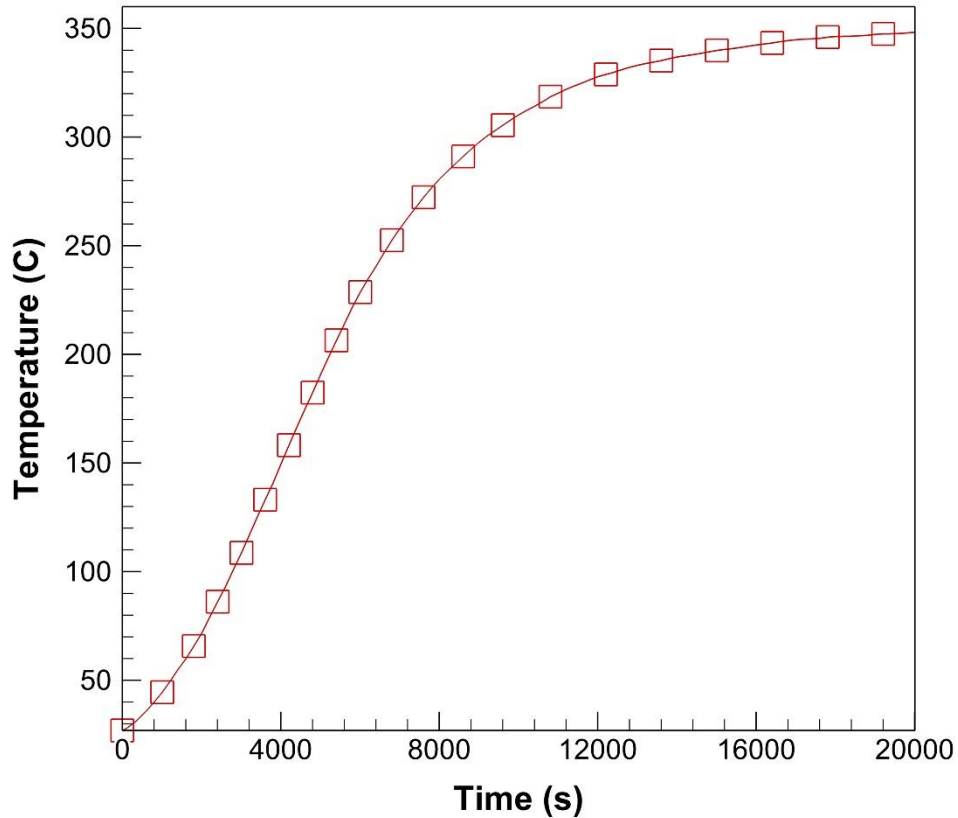
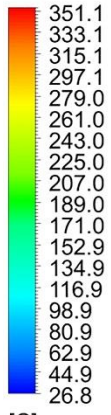


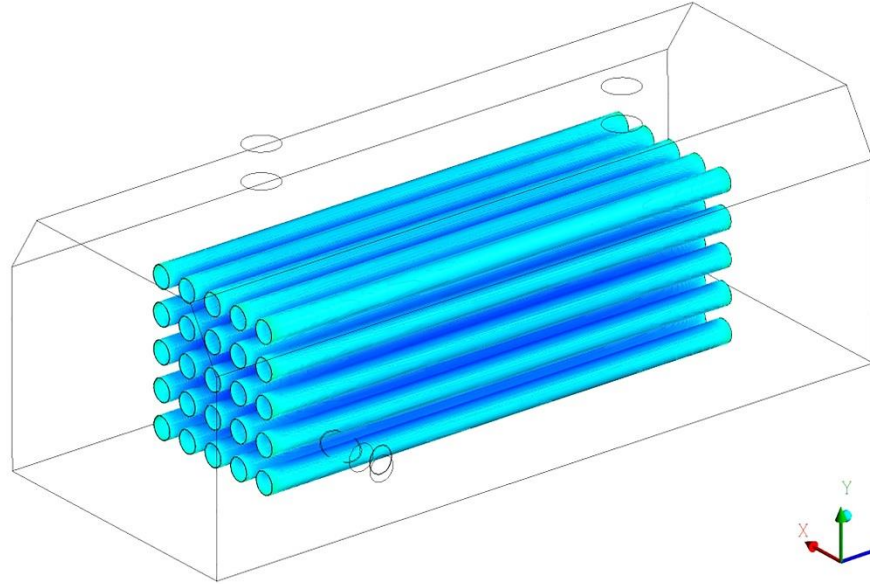
**Figure 5.16** Steel pipes temperature as a function of process time.

Temperature distribution among steel pipes for the three time steps of 605 second, 10800 second, and 20,005 second is shown in Figure 5.17. The initial steel pipe temperature was 27°C. After 605 second, the average temperature of steel pipes reached around 80°C. The average temperature continuously increases around 300°C at 10800 second. Finally, at 20005 second, the average temperature reached around 350°C. Every steel pipe inside the annealing furnace showed nearly the same temperature distribution. This is due to the fact that the swirl flow generated by the elbow inlet and the downward jet flow followed by the upward buoyancy flow make better mixing, and thus the temperature difference among the steel pipes inside the modified furnace reduces remarkably than the temperature difference in the basic furnace model.

Temperature  
Contour 1

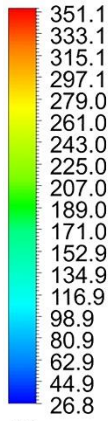


[C]

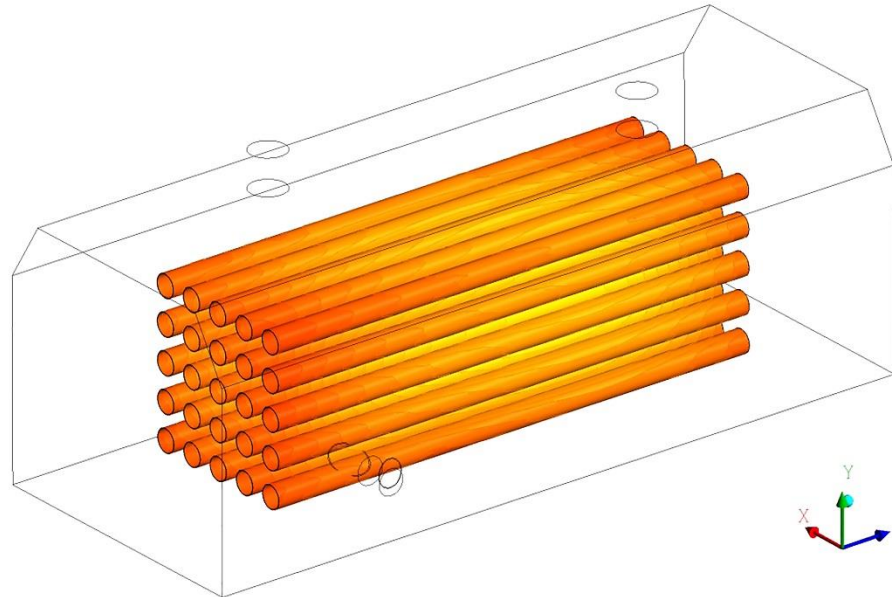


(a)

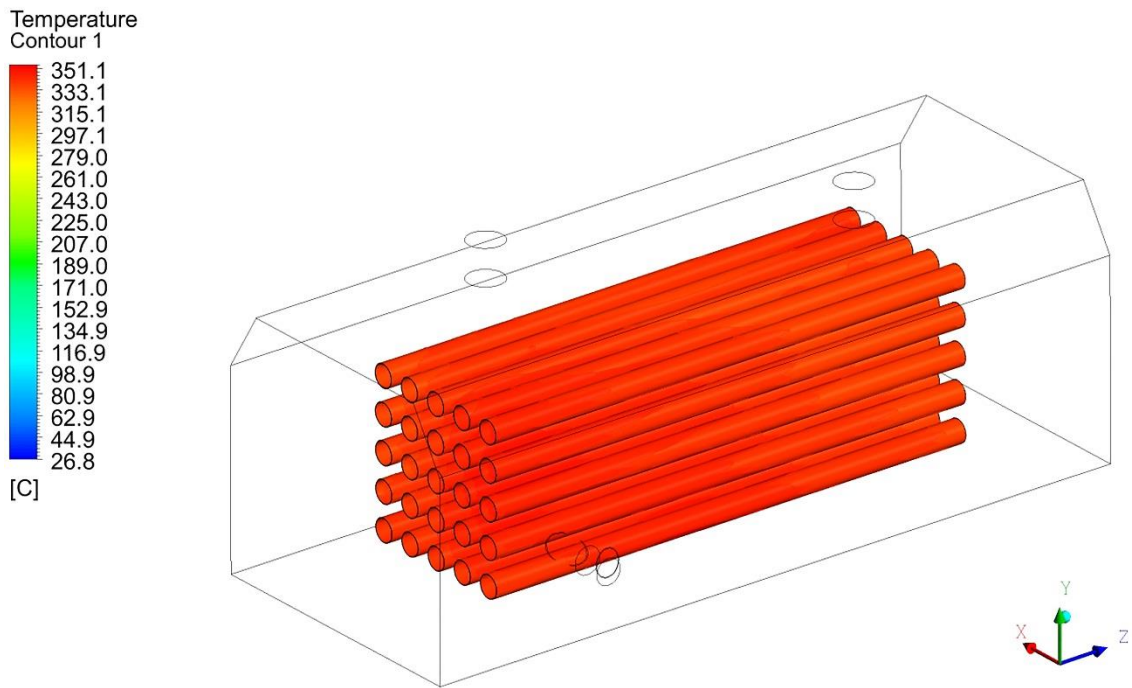
Temperature  
Contour 1



[C]



(b)



(c)

**Figure 5.17** Temperature distribution contour along steel pipes of three kind of time step: (a) 605 second; (b) 10800 second; (c) 20005 second.

### 5.7 Total deformation of steel pipes during annealing process

To investigate the total deformation of a bundle of steel pipes, the right side of steel pipes is assumed as the fixed part and the left side is the free part as shown in Figure 5.18. The mechanical properties of steel pipes are presented in the Table 5.4. Then the total deformation of steel pipes during annealing process with respect to time was presented in Figure 5.19

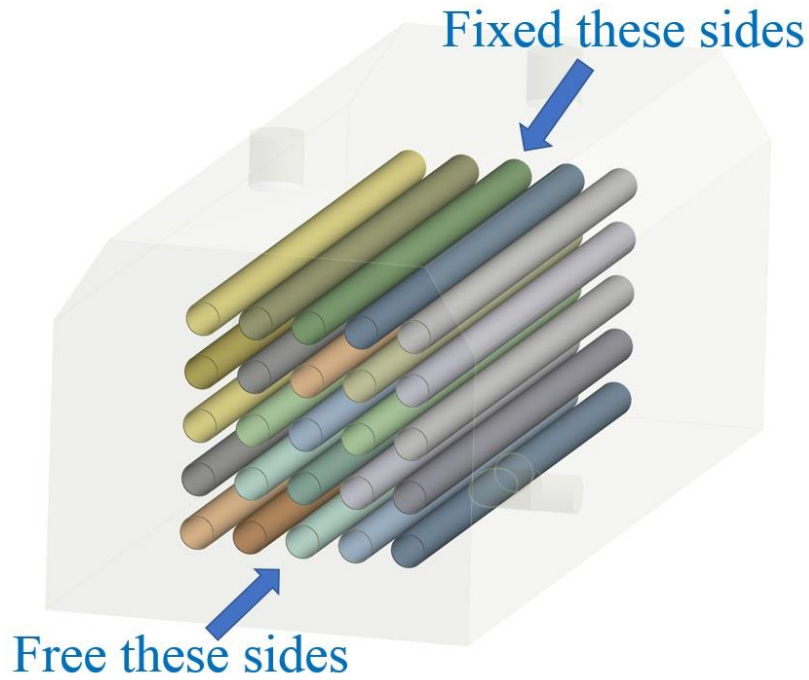
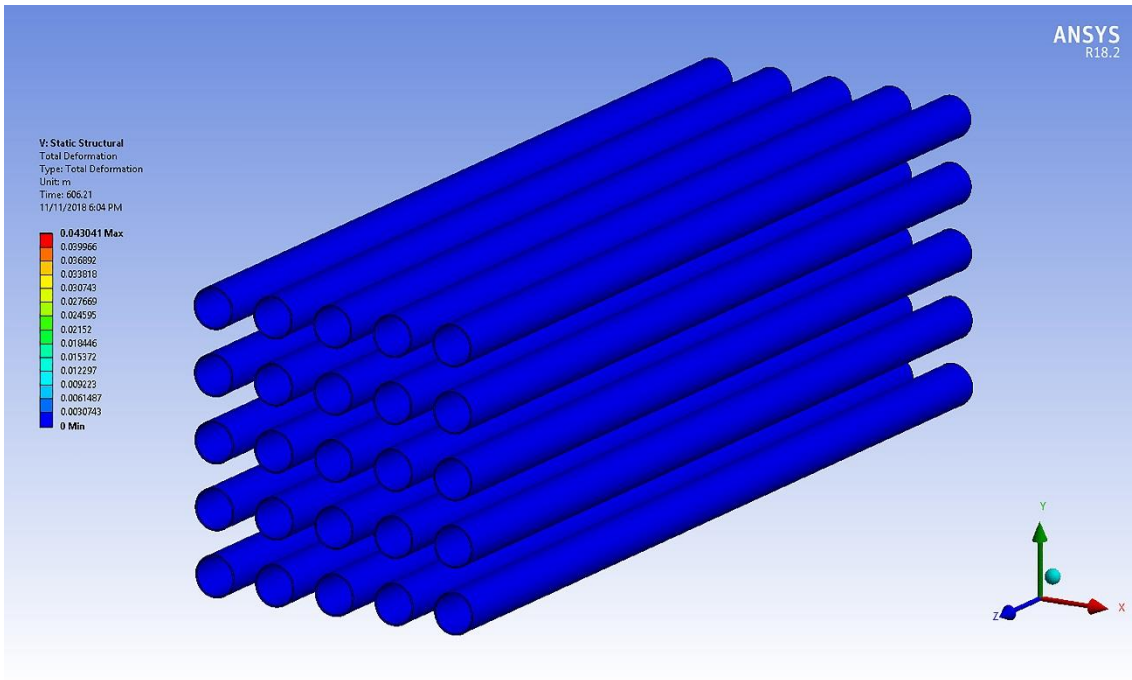


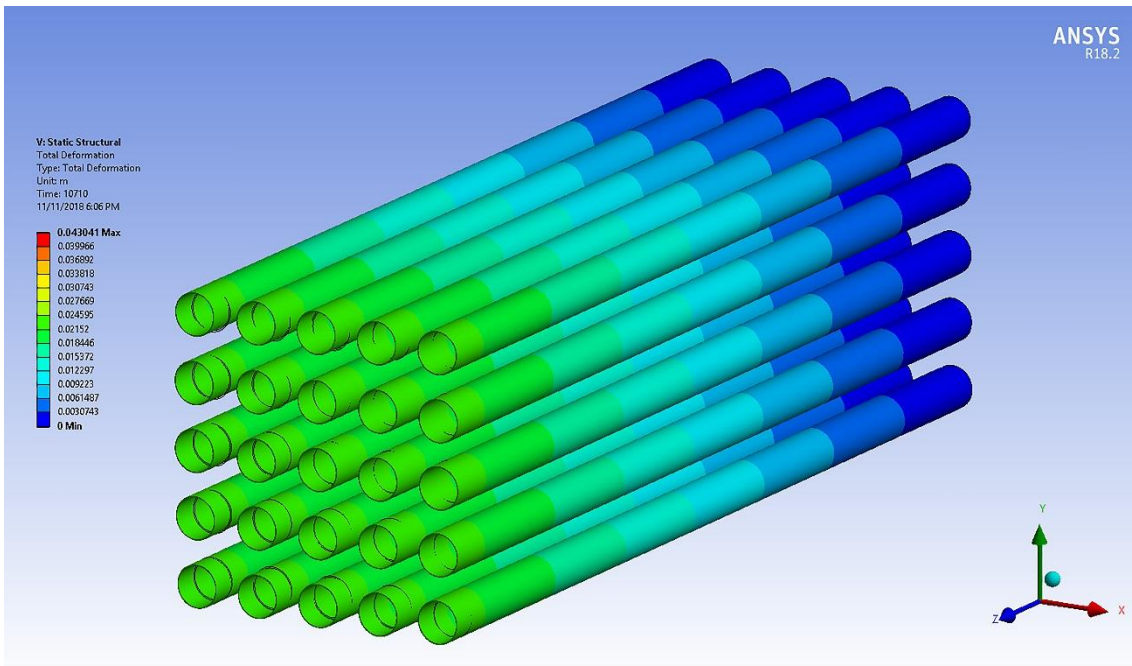
**Figure 5.18 Constraint condition of the bundle of steel pipes**

**Table 5.4 Mechanical properties of steel pipes**

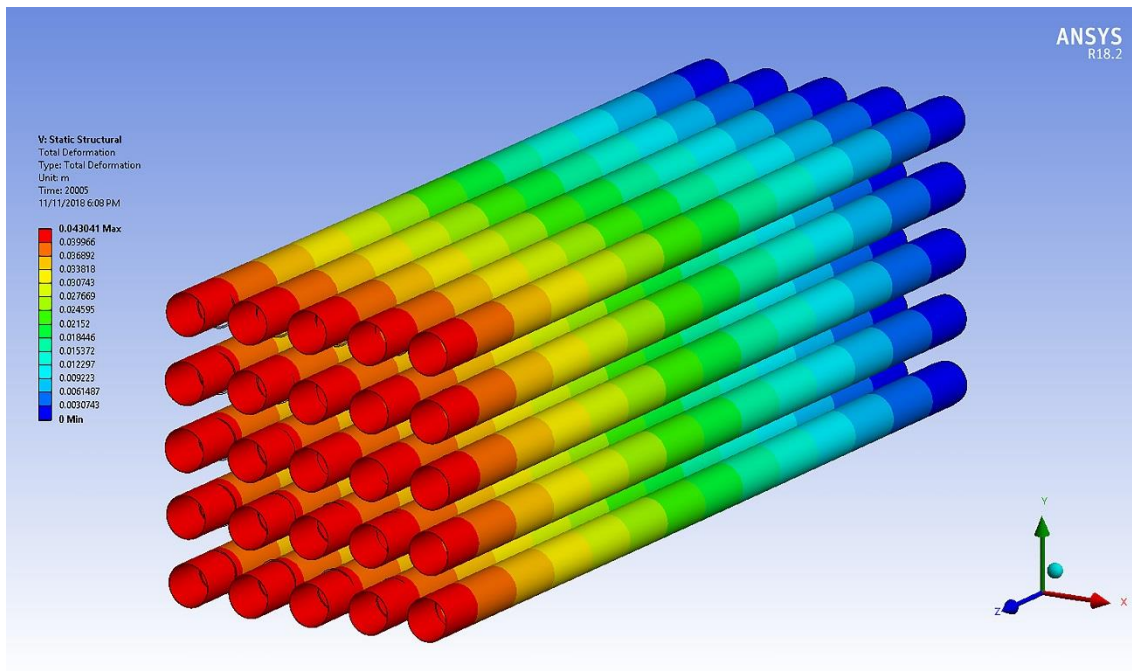
<b>Temperature, (°C)</b>	<b>Density (g/mm<sup>-3</sup>)</b>	<b>Thermal expansion coefficient (°C<sup>-1</sup>)</b>	<b>Young's modulus (GPa)</b>	<b>Poisson's ratio</b>
0	0.790	1.70e <sup>-5</sup>	198.5	0.294
100	0.788	1.74e <sup>-5</sup>	193	0.295
200	0.783	1.80e <sup>-5</sup>	185	0.301
300	0.779	1.86e <sup>-5</sup>	176	0.310
400	0.775	1.91e <sup>-5</sup>	167	0.318
600	0.766	1.96e <sup>-5</sup>	169	0.326
800	0.756	2.02e <sup>-5</sup>	151	0.333



(a)



(b)



(c)

**Figure 5.19** The total deformation of steel pipes for the three kind of time step: (a) 606 second; (b) 10710 second; (c) 20005 second.

In a short time of 600 seconds, the steel deformation does not change by around 3 mm. However, at a time of 10800 seconds, steel expands to around 20 mm and then the maximum deformation for each steel pipe is 43 mm at 20000 seconds. The ratio of the highest pipe expansion to the original length in the final annealing process is 0.43%.

## 5.8 Summary

Numerical simulation with aid of ANSYS FLUENT 18.2 software was performed to study the flow field and temperature difference of a bundle of steel pipes inside the basic and modified annealing furnace models. The modified models showed the well mixed uniform flow than the basic model due to the swirl flow and the downward jet flow followed by the upward buoyancy flow. The temperature difference of a bundle of steel pipes in the modified models was also smaller than that in the conventional basic model. The reduction percentages of the temperature difference among the steel pipes between the model 1, model 2, model 3 based on the basic model were 72.4%, 76.5%, and 57.4%, respectively. The flow field and temperature distribution in this study could enhance those of Han et al. [78] who performed a study on rotational flow of a fan, and Prieler et al. [94] who performed a study on baffle angle inlet.

Moreover, the optimization of the downward elbow inlet angle was carried out for reducing the temperature difference of a bundle of steel pipes for three kinds of models. The elbow angle inlet of 30 degrees had the lowest temperature difference of 13°C for a bundle of steel pipes among the modified models during annealing process. Steel pipe temperature increase sharply from the initial to 8000 second then increased gradually until steady state is reached. The temperature difference of the bundle of steel pipes increased as Reynolds number increased. Effects of the horizontal and vertical spacing of steel pipes on temperature distribution were also examined. Results showed that the temperature difference of steel pipes decreased as the horizontal and vertical spacing increased. Present simulation also provides a kind of design map for an arrangement of steel pipes (horizontal and vertical spacing) in an annealing furnace. For example, the pertinent position of the steel pipe arrangement at  $Re = 24000$  is  $S_h/d = 3.13$  and  $S_v/d = 1.56$  to obtain the lowest temperature difference value of 9°C. During annealing process, the total deformation of a bundle of steel pipes was investigated. The ratio of the highest steel pipe expansion to the original length is 0.43%.

# Conclusions and Further Works

## 6.1 Conclusions

This thesis is associated with the heat treatment processes in steel industry such as preheating and annealing by hot gas combustion. For steel preheating, gas torch using LPG as fuel preheats the steel plate for around 30 minutes. Numerical and experimental results are compared for the temperature distribution on the back side of the steel plate. In addition, a bundle of steel pipes is annealed by hot combustion gas from the Hot Mixing Chamber (HMC). Horizontal and vertical spacing of steel pipes are also investigated to optimize minimum temperature difference of steel pipes.

The results could be expressed as follows:

(1) The uniform flow distribution at the outlet of the gas torch is studied by ANSYS FLUENT 18.2 software. The uniformity was improved by three new models. For three new models, the pressure drop and velocity distribution at the outlet were nearly invariable along the lengthwise direction compared with the basic model. The uniformity indices of the three new models are also better than that of the original model. The maximum percentage between the three new models and the basic model is 7.3%. These models were applied to manufacture as prototype torch, and then they were used for an experiment.

With a pertinent trade-off (between the capital cost for the new design and the operating cost to save the fuel energy and to obtain a good quality for steel preheating), a suitable geometry of gas torch can be used for the actual applications, particular in steel preheating.

(2) Numerical simulation and experiment are performed to study temperature distribution on the back side of the steel plate during the preheating process. For the complete or incomplete combustion, the basic model has a larger temperature difference

between the center and the edge than the modified model. Temperature differences for the basic and the modified model are 229°C and 90°C, respectively. The numerical simulation results using ANSYS FLUENT showed also good agreements with experimental results for both complete and incomplete combustion. Moreover, the influences of the equivalent ratio ( $\Phi$ ), Reynolds number (Re) and the ratio of the axial torch outlet-to-plate distance to the nozzle diameter ( $Y/d$ ) are investigated. For the equivalent ratio, the highest temperature is found at the stoichiometric value whereas the lean or rich fuel is also induced to reduce the temperature. The higher Reynolds number, the higher temperature distribution at the back-side of steel plate. Since the flame temperature decreases due to heat loss by convection and radiation, we need to adjust the distance between the torch and the steel plate for preheating. As present numerical simulation and experimental results are in good agreement for the temperature distribution of the back-side of the steel plate during the steel plate preheating process, a numerical simulation can be a good tool to predict the temperature distribution of the steel plate.

To improve the gas torch performance, the guide vane angle at the outlet of the gas torch should be selected as optimized value. It is found that the angle of 40 degrees has the highest temperature distribution in the present study. With the consideration of the above design and operation variables, it can be selected for a manufacturer to enhance the combustion efficiency and reduce the fuel consumption for industrial steel plate preheating process.

(3) Numerical simulation and experiment are performed to study the flow field and temperature distribution on the basic and modified HMC model. The basic model has so high surface temperature and non-uniform flow mixing. On the contrary, the modified model with the three cold air inlets and the perforated inner cylinder showed not only well-mixed flow between the cold air and the hot combustion gas but also colder surface temperature of the HMC. Numerical simulation results and experimental results show good agreements at the center, the half of radius, and the surface of HMC.

(4) Numerical simulation with aid of ANSYS FLUENT 18.2 software was performed to study flow field and temperature difference of a bundle of steel pipes inside the basic

and modified annealing furnace models. The modified models showed the well-mixed uniform flow than the basic model due to the swirl flow and the downward jet flow followed by the upward buoyancy flow. The temperature difference of a bundle of steel pipes in the modified models was also smaller than that in the conventional basic model. The percentage reductions of the temperature difference of the steel pipes between the three modified models and the basic model were 72.4%, 76.5%, and 57.4%, respectively. The flow field behavior and temperature distribution in this study coincide well with those of Han et al. [78], who performed a study on the rotational flow of a fan.

Moreover, the optimization of the downward elbow inlet angle was carried out for reducing the temperature difference of bundle of steel pipes in three kinds of furnace inlet models. The elbow angle inlet of 30 degrees had the lowest temperature difference of 13°C of the bundle of steel pipes among the modified models during the annealing process. Steel pipe temperature increases sharply from the initial to 8000 seconds then increased gradually until a steady state is reached. The temperature difference of the bundle of steel pipes increased as Reynolds number increased. Effects of the horizontal and vertical spacing of steel pipes on temperature distribution were also examined. Results showed that the temperature difference of steel pipes decreased as the horizontal and vertical spacing increased. The present simulation also provides a kind of design map for an arrangement of steel pipes (horizontal and vertical spacing) in an annealing furnace. For example, the pertinent position of the steel pipe arrangement at  $Re = 24000$  is  $S_h/d = 3.13$  and  $S_v/d = 1.56$  to obtain the lowest temperature difference value of 9°C. During the annealing process, the total deformation of a bundle of steel pipes was investigated. The ratio of the highest steel pipe expansion to the original length is 0.43%.

## **6.2 Limitations and Further Works**

Overall, CFD simulation has limitations because of computer memory problem. For the steel preheating, the moving gas torch is also important during the preheating process. Consequently, the full fluid domain is required for numerical simulation and also high power and memory is necessary. For the steel annealing furnace, simulation was only carried out on the same pipes, instead of the multiple shapes such as fitting, elbows, connecting, etc. In actual work, many kinds of components are arranged on every stage. Moreover, the cooling rate after steel annealing is also important in the

whole annealing process. The issues mentioned in the above are some limitations of this dissertation. In addition, constructing a real furnace to obtain experimental data of the operational conditions and simulation results as well as evaluation of the costs for commercialization of steel annealing process will be the future works.

For the further works, recovering waste heat from the HMC, annealing furnace to harvest electric power is also the interesting point. Thermoelectric generator (TEG) device is a candidate for waste heat recovery in the industry. TEG is a device which generates electricity using the difference in temperature on both sides of TEG device. In recent years, thermoelectric has become increasingly important with numerous applications by some advance.

The necessity of TEG for power harvesting from annealing furnace waste heat recovery:

- TEGs are a solid-state device, which means that they have no moving parts during their operations.
- Because of no rotation parts, this TEG is completely silent and extremely reliable.
- Widely temperature difference range, TEG devices are suitable for waste heat recovery.
- Reduction in consumption and reduction in cost, also a reduction in pollution.
- Long lifetime

There are many kinds of TEG materials that are employed in commercial applications today as shown in Figure 6.1. These materials can be divided into three groups based on the temperature range of operation: (<https://thermoelectric-generator.com/how-thermoelectric-teg-generators-work/>)

- Low-temperature materials (up to around 320°C): Alloys based on Bismuth (Bi) in combinations with Antimony (Sb), Tellurium (Te) or Selenium (Se).
- Intermediate temperature (450 – 600°C): such as materials based on alloys of Lead (Pb)
- The highest temperatures material (600 – 850°C): materials fabricated from silicon germanium (Si-Ge) alloys.

TEG device is intended to use to recover waste heat from annealing furnace as shown in Figure 6.1. The hot flow from two Hot Mixing Chamber (HMC) is supplied to annealing furnace for steel annealing process. Two flue gas leaves the furnace and pass through heat exchangers which placed near the end of discharged pipes. In order to harvest electric power, the hot side of the TEG is exposed to the annealing furnace wall and the flue gas discharge and the cold side releases heat to ambient air. The generated electricity from TEG can be harvested as a power source.

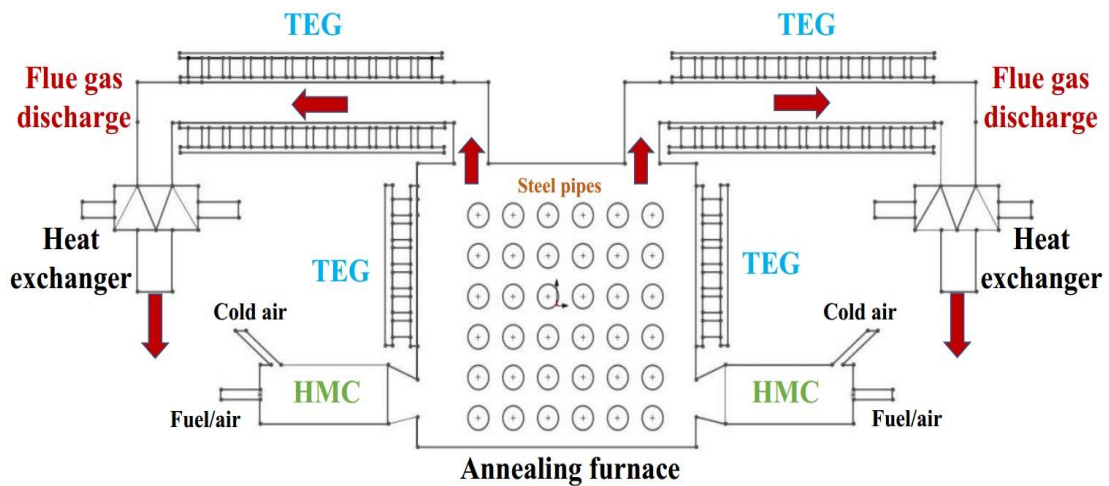


**Figure 6.1** Waste heat recovery from annealing furnace using TEG device

## References

1. Liu, H.; Li, P.; Lew, J.V.; Daniel, J.R. Experimental study of the flow distribution uniformity in flow distributors having novel flow channel bifurcation structures. *Exp. Therm. Fluid Sci.* **2012**, *37*, 131–145.
2. Liu, H.; Li, P. Even distribution dividing of single-phase fluids by symmetric bifurcation of flow channels. *Int. J. Heat Fluid Flow* **2013**, *40*, 165–179.
3. Liu, H.; Li, P. Wang, K. The flow downstream of a bifurcation of a flow channel for uniform flow distribution via cascade flow channel bifurcations. *App. Therm. Eng.* **2015**, *81*, 114–127.
4. Liu, H.; Li, P.; Lew, J.V. CFD study on flow distribution uniformity in fuel distributors having multiple structural bifurcations of flow channels. *Int. J. Hyd. Energy* **2010**, *35*, 9186–9198.
5. Huang, C.; Wen-jie, Lv.; Wang, J.G.; Wang J.Y.; Wang, H.L. Uniform distribution design and performance evaluation for uu-type parallel mini-hydro cyclones, *Sep. Pur. Tech.* **2014**, *125*, 194–201.
6. Commenge, J.M.; Saber, M.; Falk, L. Methodology for multi-scale design of isothermal laminar flow networks, *Chem. Eng. Jour.* **2011**, *173*, 541–551.
7. Commenge, J.M.; Falk, L.; Corriou, J.P.; Matlosz, M. Optimal design for flow uniformity in microchannel reactors, *AIChE Jou.* **2002**, *48*, 345–358.
8. Luo, L.; Fan, Z.; Gall, H.L.; Zhou, X.; Yuan, W. Experimental study of constructal distributor for flow equidistribution in a mini cross flow heat exchanger (MCHE), *Chem. Eng. Proc.* **2008**, *47*, 229–236.
9. Luo, L.; Wei, M.; Fan, Y.; Flamant, G. Heuristic shape optimization of baffled fluid distributor for uniform flow distribution, *Chem. Eng. Sci.* **2015**, *123*, 542–556.
10. Luo, L.; Tondeur, D. Multiscale optimization of flow distribution by constructal approach, *China Part.* **2005**, *3*, 329–336.
11. Lalot, S.; Florent, P.; Lang, S.K.; Bergles, A.E. Flow maldistribution in heat exchangers, *Appl. Therm. Eng.* **1999**, *19*, 847–863.
12. Fan, Z.; Zhou, X.; Luo, L.; Yuan, W. Experimental investigation of the flow distribution of a 2-dimensional constructal distributor, *Exp. Therm. Fluid Sci.* **2008**, *33*, 77–83.
13. Purimetla, A.; Cui, J. CFD studies on burner secondary airflow, *Appl. Math. Model.* **2009**, *33*, 1126–1140.
14. Zhang, T.H.; Liu, F.G.; You, X.Y. Optimization of gas mixing system of premixed burner based on CFD analysis, *Energy Convers. Manag.* **2014**, *85*, 131–139.
15. Heggemann, M.; Hirschberg, S.; Spiegel, L.; Bachmann, C. CFD Simulation and experimental validation of fluid flow in liquid distributors, *Inst. Chem. Eng.* **2007**, *85*, 59–64.

16. Perta, E.S.D.; Agizza, M.A.A.; Sorrentino, G.; Boccia, L. Pindozzi, S. Study of aerodynamic performances of different wind tunnel configurations and air inlet velocities, using computational fluid dynamics (CFD). *Comp. Elec. Agr.* **2016**, 125, 137–148.
17. Remie, M.J.; Cremers, M.G.G.; Schreel, K.R.A.M.; Goey, L.P.H. Analysis of the heat transfer of an impinging laminar flame jet. *Int. J. Heat Mass Transfer* **2007**, 50, 2816–2827.
18. Sahu, S.; Dewangan, M.; Analysis of heat transfer characteristics of flame impinging to a plane surface perpendicular to flame jet axis. *Int. J. Eng. Res. Tech.* **2013**, 2, 578–593.
19. Tajik, A.R.; Kuntikana, P.; Prabhu, S.V.; Hindasageri, V. Effect of preheated mixture on heat transfer characteristics of impinging methane–air premixed flame jet. *Int. J. Heat Mass Transfer* **2015**, 86, 550–562.
20. Yu, C.C.; Derek, D.R. Electric field induced changes of a diffusion flame and heat transfer near an impinging surface. *Energ.* **2018**, 11, 1–13.
21. Liu, Y.F.; Xiang, Q.; Li, Z.; Yao, S.Z.; Liang, X.Y.; Wang, F. Experiment and simulation investigation on the characteristics of diesel spray impingement based on droplet impact phenomenon. *Appl. Sci.* **2018**, 8, 1– 11.
22. ANSYS FLUENT Theory Guide; ANSYS Inc: Canonsburg, PA, USA, 2013; pp.133–720.
23. Sorrentino, G.; Ceriello, G.; Joannon, M.; Sabia, P.; Ragucci, R.; Oijen, J.; Cavaliere, A.; Goey, L.P.H. Numerical investigation of moderate or intense low-oxygen dilution combustion in a cyclonic burner using a flamelet generated manifold approach. *Energy Fuels* **2018**, 32, 10242–10255.
24. Attarha, M.J.; Sattari-Far, I. Study on welding temperature distribution in thin welded plates through experimental measurements and finite element simulation. *J. Mat. Pro. Tech.* **2011**, 211, 688–694
25. Akram, M.; Kumar, S.; Saxena, P. Experimental and computational determination of laminar burning velocity of liquefied petroleum gas-air mixtures at elevated temperatures. *J. Eng. Gas Turb. Power* **2013**, 135, 1–5.
26. Li, H.B.; Zhen, H.S.; Leung, C.W.; Cheung, C.S. Nozzle effect on heat transfer and CO emission of impinging premixed flames. *Int. J. Heat Mass Transfer* **2011**, 54, 625–635.
27. Li, H.B.; Zhen, H.S.; Leung, C.W.; Cheung, C.S. Effects of plate temperature on heat transfer and emissions of impinging flames. *Int. J. Heat Mass Transfer* **2010**, 53, 4176–4184.
28. Zhen, H.S.; Leung, C.W.; Cheung, C.S. Heat transfer characteristics of an impinging premixed annular flame jet. *Appl. Therm. Eng.* **2012**, 36, 386–392.
29. Chander, S.; Ray, A. Heat transfer characteristics of laminar methane air flame impinging normal to a cylindrical surface. *Exp. Therm. Fluid Sci.* **2007**, 32, 707–721.

30. Katti, V.; Prabhu, S.V. Experimental study and theoretical analysis of local heat transfer distribution between smooth flat surface and impinging air jet from a circular straight pipe nozzle. *Int. J. Heat Mass Transfer* **2008**, *51*, 4480–4495.
31. Hindasageri, V.; Vedula, R.P.; Prabhu, S.V. Heat transfer distribution for impinging methane-air premixed flame jets. *Appl. Therm. Eng.* **2014**, *73*, 461–473.
32. Wei, D.H.; Ta, H.L. Methane flame stability in a jet impinging onto a wall. *Energy Convers. Manag.* **2005**, *46*, 727–739.
33. Zhao, Z.; Wong, T.T.; Leung, C.W. Impinging premixed butane air circular laminar flame jet influence of impingement plate on heat transfer characteristics. *Int. J. Heat Mass Transfer* **2004**, *47*, 5021–5031.
34. Akram, M.; Kumar, S. Measurement of laminar burning velocity of liquefied petroleum gas air mixtures at elevated temperatures. *Energy Fuels* **2012**, *26*, 3267–3274.
35. Akram, M.; Kumar, S.; Saxena, P. Experimental and computational determination of laminar burning velocity of liquefied petroleum gas-air mixtures at elevated temperatures. *J. Eng. Gas Turb. Power* **2013**, *135*, 1–5.
36. Remie, M.J.; Cremers, M.G.G.; Schreel, K.R.A.M.; Goey, L.P.H. Analysis of the heat transfer of an impinging laminar flame jet. *Int. J. Heat Mass Transfer* **2007**, *50*, 2816–2827.
37. Sahu, S.; Dewangan, M. Analysis of heat transfer characteristics of flame impinging to a plane surface perpendicular to flame jet axis. *Int. J. Eng. Res. Tech.* **2013**, *2*, 578–593.
38. Tajik, A.R.; Kuntikana, P.; Prabhu, S.V.; Hindasageri, V. Effect of preheated mixture on heat transfer characteristics of impinging methane–air premixed flame jet. *Int. J. Heat Mass Transfer* **2015**, *86*, 550–562.
39. Liu, Y. F.; Xiang, Q.; Li, Z.; Yao, S. Z.; Liang, X. Y.; Wang, F. Experiment and simulation investigation on the characteristics of diesel spray impingement based on droplet impact phenomenon. *Appl. Sci.* **2018**, *8*, 1–11.
40. Zhen, H.S.; Cheung, C.S.; Leung, C.W.; Choy, Y.S. Effects of hydrogen concentration on the emission and heat transfer of a premixed LPG-hydrogen flame. *Int. J. Hyd. Energy* **2012**, *37*, 6097–6105.
41. Zhen, H.S.; Cheung, C.S.; Leung, C.W.; Choy, Y.S. A comparison of the emission and impingement heat transfer of LPG-H<sub>2</sub> and CH<sub>4</sub>-H<sub>2</sub> premixed flames. *Int. J. Hyd. Energy* **2012**, *37*, 10947–10955.
42. Mohr, J.W.; Yagoobi, J.S.; Page, R.H. Combustion measurements from an impinging radial jet reattachment flame. *Comb. Flame* **1996**, *106*, 69–80.
43. Singh, G.; Chander, S.; Ray, A. Heat transfer characteristics of natural gas/air swirling flame impinging on a flat surface. *Exp. Therm. Fluid Sci.* **2012**, *41*, 165–176.

44. Singh, S.; Chander, S. Heat transfer characteristics of dual flame with outer swirling and inner non-swirling flame impinging on a flat surface. *Int. J. Heat Mass Transfer* **2014**, *77*, 995–1007.
45. Singh, S.; Chander, S. Heat transfer characteristics of dual swirling flame impinging on the flat surface. *Exp. Therm. Fluid Sci.* **2015**, *89*, 1–12.
46. Huang, X.Q.; Leung, C.W.; Chan, C.K.; Probert, S.D. Thermal characteristics of a premixed impinging circular laminar-flame jet with induced swirl. *Appl. Energy* **2006**, *83*, 401–411.
47. Zhao, Z.; Yuen, D.W.; Leung, C.W.; Wong, T.T. Thermal performance of a premixed impinging circular flame jet array with induced-swirl. *Appl. Therm. Eng.* **2009**, *29*, 159–166.
48. Luo, D.D.; Zhen, H.S.; Leung, C.W.; Cheung, C.S. Premixed flame impingement heat transfer with induced swirl. *Int. J. Heat Mass Transfer* **2010**, *53*, 4333–4336.
49. Agrawal, G.K.; Chakraborty, S.; Som, S.K. Heat transfer characteristics of premixed flame impinging upwards to plane surfaces inclined with the flame jet axis. *Int. J. Heat Mass Transfer* **2010**, *53*, 1899–1907.
50. Kwok, L.C.; Leung, C.W.; Cheung, C.S. Heat transfer characteristics of an array of impinging. *Int. J. Heat Mass Transfer* **2005**, *48*, 1727–1738.
51. Makmool, U.; Jugjai, S.; Tia, S. Structures and performances of laminar impinging multiple premixed LPG–air flames. *Fuel* **2013**, *112*, 254–262.
52. Dong, L.L.; Leung, C.W.; Cheung, C.S. Heat transfer and wall pressure characteristics of a twin. *Int. J. Heat Mass Transfer* **2004**, *47*, 489–500.
53. Dong, L.L.; Leung, C.W.; Cheung, C.S. Heat transfer of a row of three butane/air flame jets impinging on a flat plate. *Int. J. Heat Mass Transfer* **2003**, *46*, 113–125.
54. Chander, S.; Ray, A. Heat transfer characteristics of three interacting methane air flame jets impinging on a flat surface. *Int. J. Heat Mass Transfer* **2007**, *50*, 640–653.
55. Hindasageri, V.; Kuntikana, P.; Vedula, R.P.; Prabhu, S.P. An experimental and numerical investigation of heat transfer distribution of perforated plate burner flames impinging on a flat plate. *Int. J. Therm. Sci.* **2015**, *94*, 156–169.
56. Penumadu, P.S.; Rao, A.G. Numerical investigations of heat transfer and pressure drop characteristics in multiple jet impingement system. *App. Therm. Eng.* **2017**, *110*, 1511–1524.
57. Shariatmadar, H.; Momeni, A.; Karimi, A.; Ashjaee, M. Heat transfer characteristics of laminar slot jet arrays impinging on a constant target surface temperature. *App. Therm. Eng.* **2015**, *76*, 252–260.
58. Shariatmadar, H.; Mousavian, S.; Sadoughi, M.; Ashjaee, M. Experimental and numerical study on heat transfer characteristics of various geometrical arrangement of impinging jet arrays. *Int. J. Therm. Sci.* **2016**, *102*, 26–38.

59. Hindasageri, V.; Vedula, R.P.; Prabhu, S.V. A novel concept to estimate the steady state heat flux from impinging premixed flame jets in an enclosure by numerical IHCP technique. *Int. J. Heat Mass Transfer* **2014**, *79*, 342–352.
60. Hindasageri, V.; Vedula, R.P.; Prabhu, S.V. Heat transfer distribution for three interacting methane–air premixed impinging flame jets. *Int. J. Heat Mass Transfer* **2015**, *88*, 914–925.
61. Kuntikana, P, Prabhu, S.V. Heat transfer investigations on impinging flame jets of a multi-port convex burner. *Appl. Therm. Eng.* **2018**, *142*, 793–814.
62. Li, J. Z.; Yuan, L.; Mongia, H. C. Simulation investigation on combustion characteristics in a four-point lean direct injection combustor with hydrogen/air. *Appl. Sci.* **2017**, *7*, 1–17.
63. Pantangi, V.K.; Mishra, S.C.; Muthukumar, P.; Reddy, R. Studies on porous radiant burners for LPG (liquefied petroleum gas) cooking applications. *Energy* **2011**, *36*, 6074–6080.
64. Muthukumar, P.; Shyamkumar, P.I. Development of novel porous radiant burners for LPG cooking applications. *Fuel* **2013**, *112*, 562–566.
65. Boggavarapu, P.; Ray, B.; Ravikrishna, R.V. Thermal efficiency of LPG and PNG-fired burners experimental and numerical studies. *Fuel* **2014**, *116*, 709–715.
66. Wu, J.; Seyed-Yagoobi, J. Heat transfer and combustion characteristics of an array of radial jet reattachment flames. *Comb. Flame* **2001**, *125*, 955–964.
67. Tajik, A.R.; Hindasageri, V. A numerical investigation on heat transfer and emissions characteristics of impinging Radial Jet Reattachment Combustion (RJRC) flame. *Appl. Therm. Eng.* **2015**, *89*, 534–544.
68. ANSYS FLUENT theory guide, ANSYS Inc, USA, **2013**, pp. 187–194.
69. Sorrentino, G.; Ceriello, G.; de Joannon, M.; Sabia, P.; Ragucci, R.; van Oijen, J.; Cavaliere, A.; de Goey, L.P.H. Numerical investigation of moderate or intense low-oxygen dilution combustion in a cyclonic burner using a flamelet generated manifold approach. *Energy Fuels* **2018**, *32*, 10242–10255.
70. Attarha, M.J.; Sattari-Far, I. Study on welding temperature distribution in thin welded plates through experimental measurements and finite element simulation. *J. Mat. Pro. Tech.* **2011**, *211*, 688–694.
71. Strommer, S.; Niederer, M.; Steinboeck, A.; Kugi, A. A mathematical model of a direct-fired continuous strip annealing furnace. *Int. J. Heat Mass Transfer* **2014**, *69*, 375–389.
72. Zareba, S.; Wolff, A.; Jelali, M. Mathematical modelling and parameter identification of a stainless-steel annealing furnace. *Sim. Mod. Pract. Theory* **2016**, *60*, 15–39.
73. Marlow, D.O. Modelling direct-fired annealing furnaces for transient operations. *Appl. Math. Modelling* **1996**, *20*, 34–40.

74. Wan, F.; Wang, Y.Q.; Qin, S.R. Modeling of strip heating process in vertical continuous annealing furnace. *J. Iron Steel Res.* **2012**, *19*, 29–36.
75. Wan, F.; Wang, Y.Q.; Qin, S.R. Modeling of strip temperature in rapid cooling section of vertical continuous annealing furnace. *J. Iron Steel Res., Int.* **2012**, *19*, 27–32.
76. Hajaliakbari, N.; Hassanpour, S. Analysis of thermal energy performance in continuous annealing furnace. *App. Eng.* **2017**, *206*, 829–842.
77. Durdan, M.; Stehlikova, B.; Pastor, M.; Kacur, J.; Laciak, M.; Flegner, P. Research of annealing process in laboratory conditions. *Measurement.* **2015**, *73*, 607–618.
78. Han, Y.; Yu, E.; Han, Z. Study on temperature distribution non-uniformity of inner grooved copper tubes during pit furnace annealing. *Int. J. Heat Mass Transfer* **2017**, *104*, 749–758.
79. Bina, M.H.; Dini, G.; Vaghefi, S.M.M.; Saatchi, A.; Raeissi, K.; Navabi, M. Application of homogenization heat treatments to improve continuous-annealing furnace roller fractures. *Eng. Fail. Anal.* **2009**, *16*, 1720–1726.
80. Martins, G.; Mendoza, O.S.H.; Amjad, M.; Filho, E.P.B. Geometric optimization of radiative heat transfer on surfaces of corrugated furnaces. *App. Therm. Eng.* **2016**, *104*, 344–357.
81. Niederer, M.; Strommer, S.; Steinboeck, A.; Kugi, A. Nonlinear model predictive control of the strip temperature in an annealing furnace. *J. Proc. Control* **2016**, *48*, 1–13.
82. Li, Y.; Wang, G.; Chen, H. Simultaneously estimation for surface heat fluxes of steel slab in a reheating furnace based on DMC predictive control. *App. Therm. Eng.* **2015**, *80*, 396–403.
83. Yan, Z.; Quan, Y.; He, A.R.; Yao, X.J.; Gou, D.F. Deviation Prevention Ability of Rollers in Continuous Annealing Furnace and Application. *J. Iron Steel Res., Int.* **2012**, *19*, 08–13.
84. Depree, N.; Sneyd, J.; Taylor, S.; Taylor, M.P.; Chen, J.J.J.; Wang, S.; O'Connor, M. Development and validation of models for annealing furnace control from heat transfer fundamentals. *Comp. Chem. Eng.* **2010**, *34*, 1849–1853.
85. Chen, T.C.; Ho, C.H.; Lin, J.C.; Wu, L.W. 3-D temperature and stress distributions of strip in preheating furnace of continuous annealing line. *App. Therm. Eng.* **2010**, *30*, 1047–1057.
86. Kang, Z.W.; Chen, T.C. Three-dimensional temperature distributions of strip in continuous annealing line. *App. Therm. Eng.* **2013**, *58*, 241–251.
87. Kang, Z.W.; Chen, T.C. Longitudinal residual warpage of strip in continuous annealing line. *App. Therm. Eng.* **2014**, *62*, 1–12.
88. Zhao, Z.; Cheng, X.; Xue, F.; He, T.; Wang, T. Effect of annealing temperature on the stress and structural properties of Ge core fibre. *J. Cry. Gro.* **2017**, *473*, 1–5.
89. Cheema, T.A.; Ali, H.; Park, C.W. Thermal-FSI based analysis of annealing process for a steel wire in a tube furnace. *App. Therm. Eng.* **2016**, *98*, 340–351.

90. Fatla, O.M.H.; Medina, A.V.; Robinson, F.; Cichuta, M.; Beynon, N. Development of convection in high temperature coil annealing furnaces using rotating cylinder technique. *App. Therm. Eng.* **2018**, 129, 1392–1402.
91. Hachem, E.; Jannoun, G.; Veysset, J.; Henri, M.; Pierrot, R.; Poitrault, I.; Massoni, E.; Coupez, T. Modeling of heat transfer and turbulent flows inside industrial furnaces. *Sim. Mod. Practice Theory* **2013**, 30, 35–53.
92. Yuan, X.; Chen, L.; Zhao, Y.; Di, H.; Zhu, F. Influence of annealing temperature on mechanical properties and microstructures of a high manganese austenitic steel. *J. Materials Proc. Tech.* **2015**, 217, 278–285.
93. Zhang, X.; Zhang, T.Y.; Wong, M.; Zohar, Y. Residual-stress relaxation in polysilicon thin films by high-temperature rapid thermal annealing. *Sensors and Act.* **1998**, 64, 109–115.
94. Prieler, R.; Mayrhofer, M.; Gaber, C.; Gerhardter, H.; Schluckner, C.; Landfahrer, M.; Gruber, M. E.; Schwabegger, G.; Hochenauer, C. CFD-based optimization of a transient heating process in a natural gas fired furnace using neural networks and genetic algorithms. *App. Therm. Eng.* **2018**, 138, 217–234.

# APPENDIX 1

## A. List of Publications

1. **Ngo, T.T.**; Go, J.; Zhou, T.; Nguyen, H.V.; Lee, G.S. Enhancement of Exit Flow Uniformity by Modifying the Shape of a Gas Torch to Obtain a Uniform Temperature Distribution on a Steel Plate during Preheating. *Appl. Sci.* **2018**, *8*, 2197.
2. **Ngo, T.T.**; Zhou, T.; Go, J.; Nguyen, H.V.; Lee, G.S. Improvement of the Steel-Plate Temperature during Preheating by Using Guide Vanes to Focus the Flame at the Outlet of a Gas Torch. *Energies* **2019**, *12*, 869.

## B. List of Conferences

### International Conferences

1. **Thien Tu Ngo**, Junho Go, Tianjun Zhou, Geun Sik Lee, 2016, “Numerical and experimental investigation of temperature distribution of a steel plate by preheating from gas torch with multi-jet flame”, IFOST Conference.
2. **Thien Tu Ngo**, Geun Sik Lee and Nguyen Minh Phu, 2017, “Transient Simulation for Heat Transfer and Pressure Drop of a Helical Heat Exchanger”, IFOST Conference.
3. **Thien Tu Ngo**, Nguyen Minh Phu and Geun Sik Lee, 2018, “Analysis of the Effects of Thermal Distribution of Tri-Generation System on Coefficient of Performance”, IFOST Conference, pp. 654-657.
4. **Thien Tu Ngo**, Minh Phu Nguyen and Geun Sik Lee, 2018, “Enhancement of Temperature Uniformity of Steel Pipes inside an Annealing Furnace by adopting Modified Inlet Geometry and Their Arrangement”, ETME, International Conference.
5. Hap Van NGUYEN, **Tu Thien NGO**, Phu Minh NGUYEN, **Geun Sik Lee**. “Numerical Investigation of Combustion for the Steel Plate during Preheating Process using the Multi-holes Gas Torch”. THE 5TH INTERNATIONAL CONFERENCE ON SUSTAINABLE ENERGY - Ho Chi Minh, 122-126 (2017).
6. Nguyen Minh Phu, **Ngo Thien Tu**, and Phan Thi Thanh Huong, 2018, “Heat transfer and friction factor correlations for a novel solar air heater”, ICMT, International Conference.

## **Domestic Conferences**

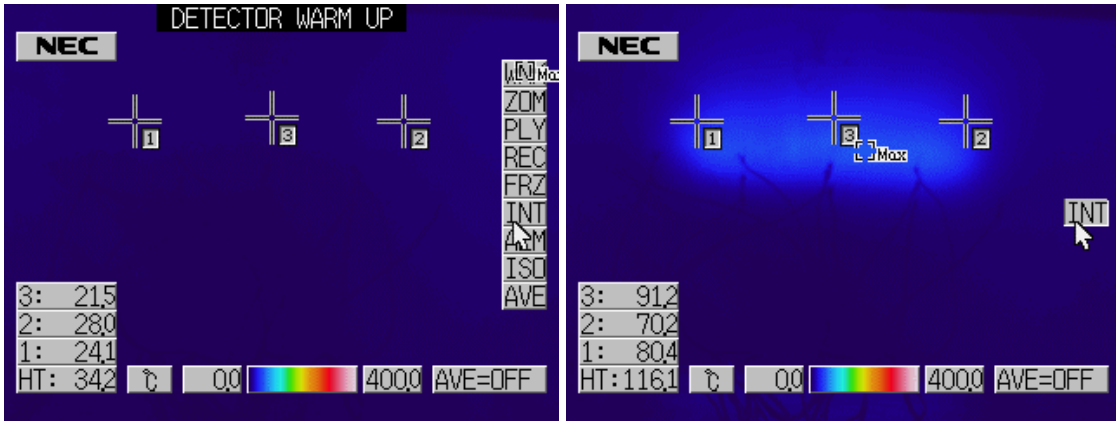
1. Geun Sik Lee, **Tu Thien Ngo**, Hap Van Nguyen and Jun Ho Go, 2015, “Improvement of Exit Flow Uniformity by Modifying the Inner and Outer Shape of Gas Torch for Steel Plate Preheating”, KSME Jeju Conference, p. 184.
2. **Thien Tu Ngo**, Hap Van Nguyen and Geun Sik Lee, 2016 “Analysis of Steel Preheating Process using Gas Torch with Multi-hole Impinging Flame”, KSME conference, pp. 314~315.
3. **Thien Tu Ngo** and Geun Sik Lee, 2017 “Investigating of Flow and Temperature Field in a Furnace for Variations of Inlets of Hot Gas during Drying Process”, KSFM conference, pp. 311~312.
4. **Thien Tu Ngo**, Geun Sik Lee, Geun Joon Lee and Seung Pil Moon, 2017, “Sensor Power from Thermoelectric Generators (TEG) Obtained from Waste Heat Discharged from a Household Air Conditioning”, KSME conference, p.45.
5. **Thien Tu Ngo**, Van Hap Nguyen and Geun Sik Lee, 2018, “Enhancement of Mixing and Temperature Distribution of Steel Pipes inside an Annealing Furnace by Adopting a Modified Inlet Structure”, KSME conference.

## **C. Awards**

1. Best paper award at Korean Society of Mechanical Engineers (KSME) conference in Gangwon, December 2018.
2. Best paper award at International Forum on Strategic Technology (IFOST), International conference in Ulsan, May 2017.

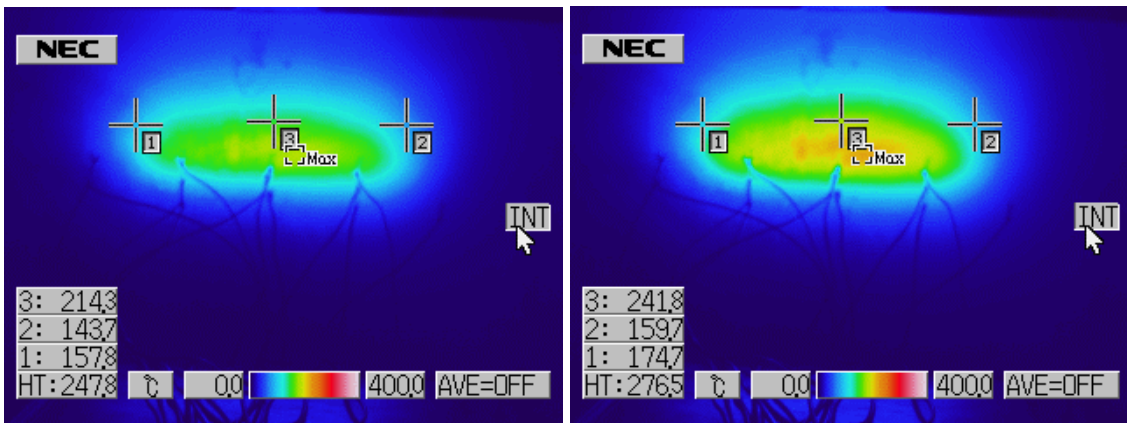
# APPENDIX 2

## 1. Experimental results of modified gas torch:



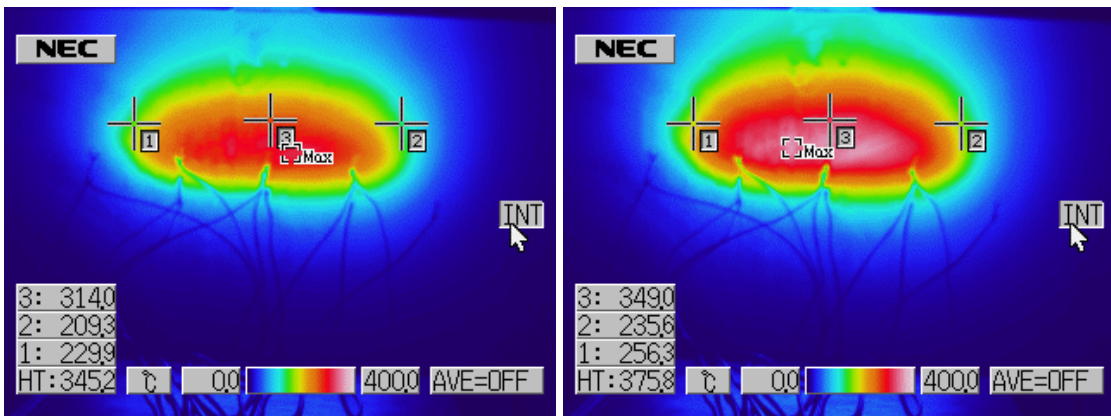
Time = 5 second

Time = 135 second



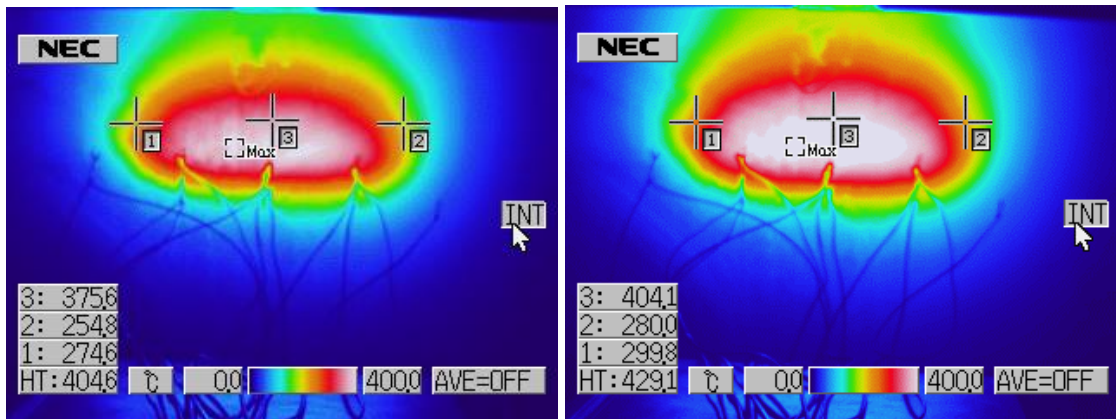
Time = 300 second

Time = 420 second



Time = 660 second

Time = 1005 second



Time = 1320 second

Time = 1800 second

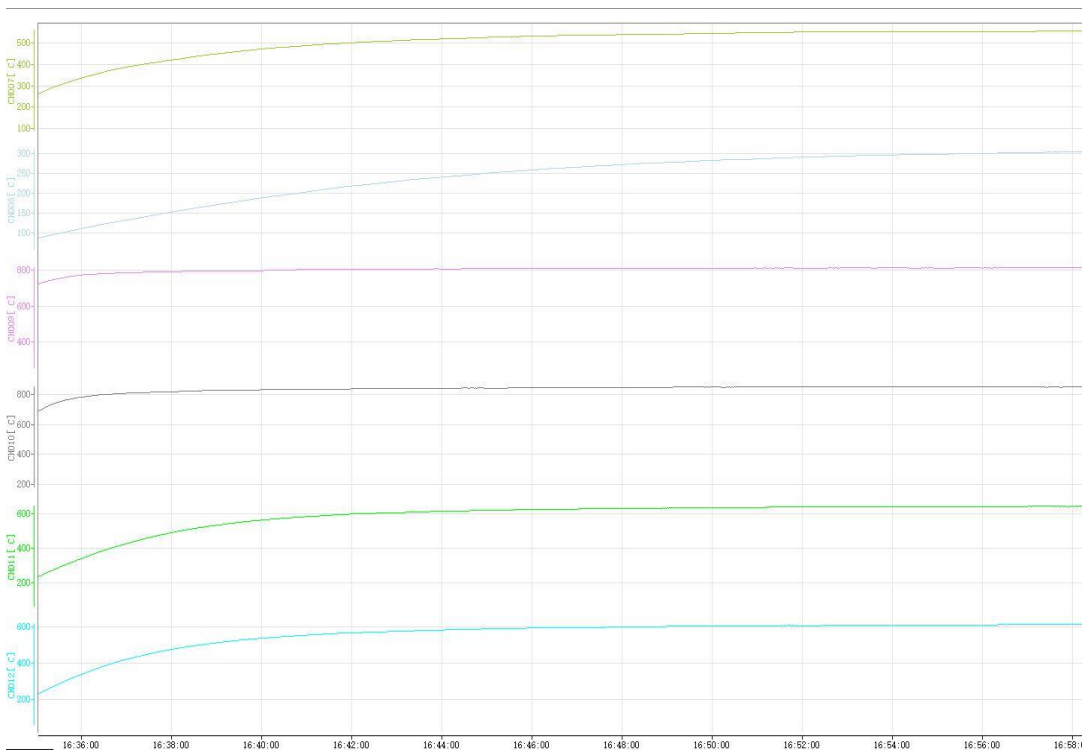
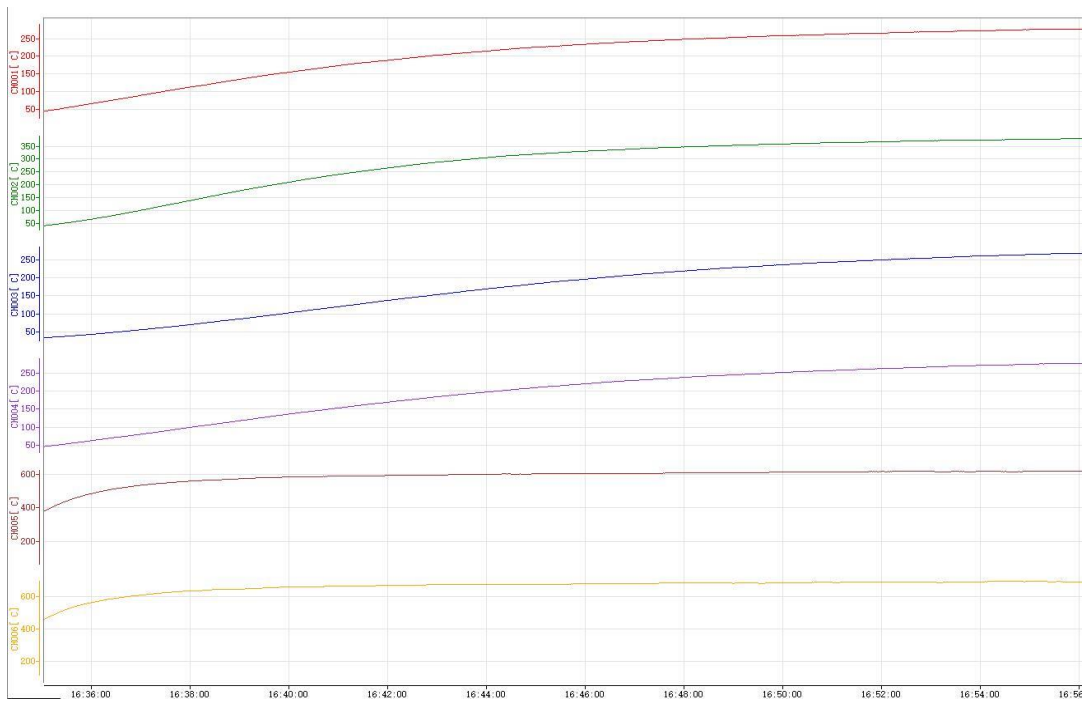
## 2. Experimental results of HMC:



Channel 1-4 HMC surface temperature

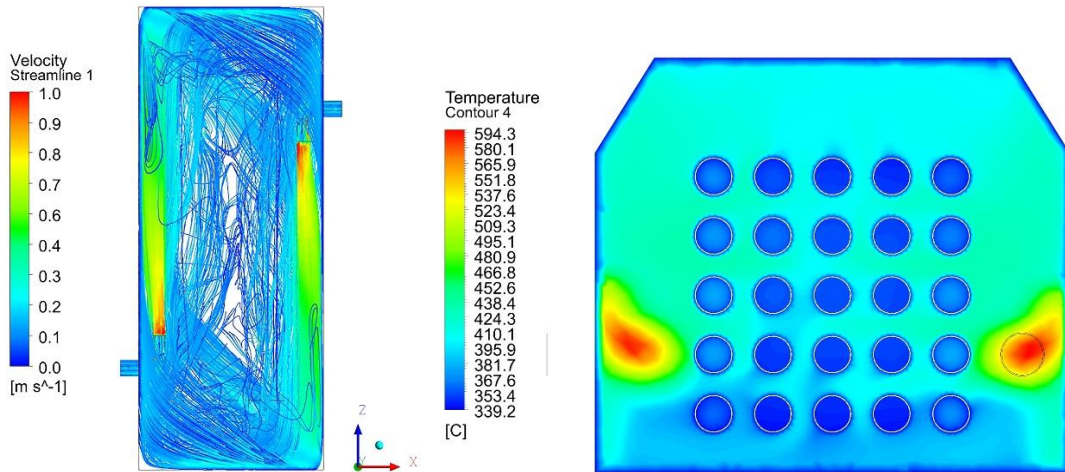
Channel 5-8 HMC quarter inner temperature

Channel 9-12 HMC middle inner temperature

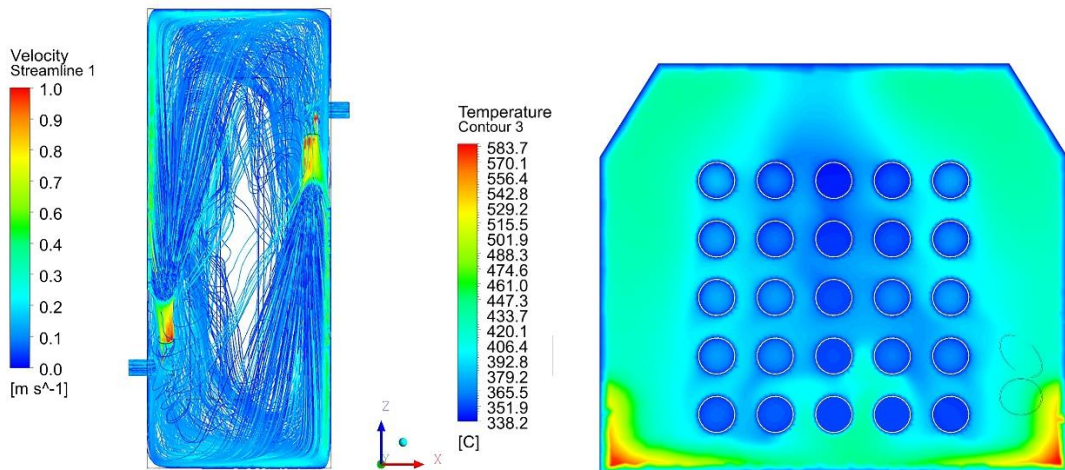


### 3. Simulation results of annealing furnace:

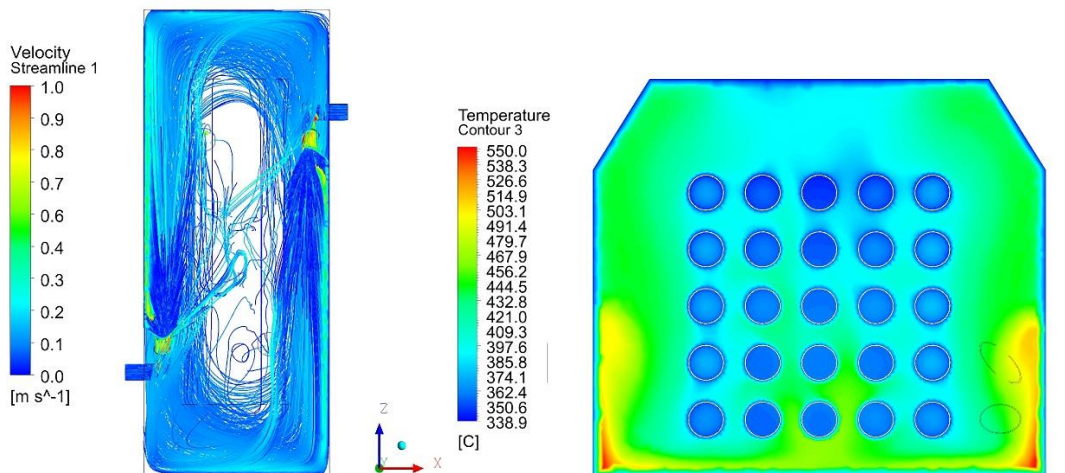
- **Model 1:** Flow field and temperature distribution



- **Model 2:** Flow field and temperature distribution



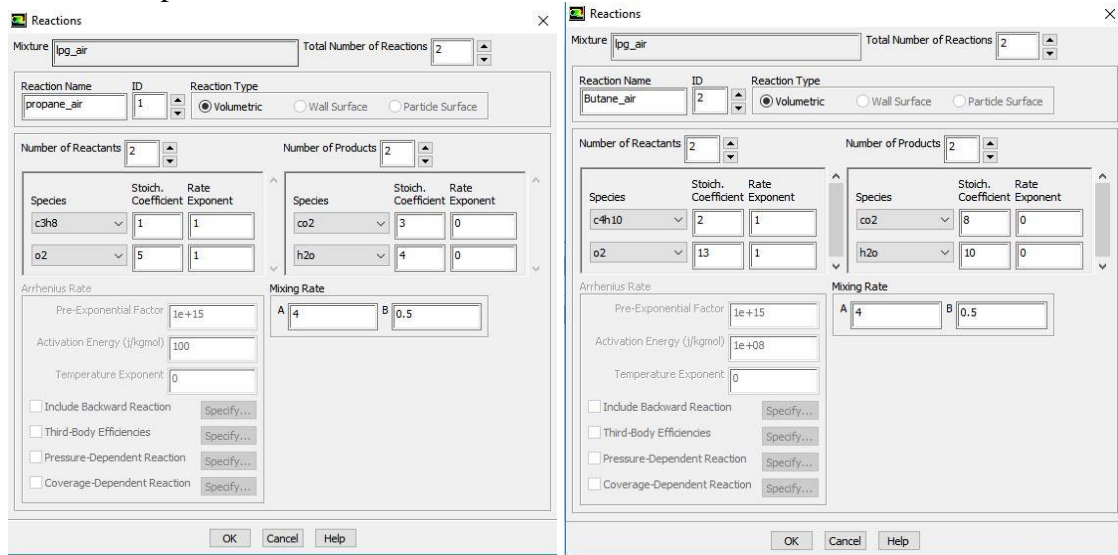
- **Model 3:** Flow field and temperature distribution



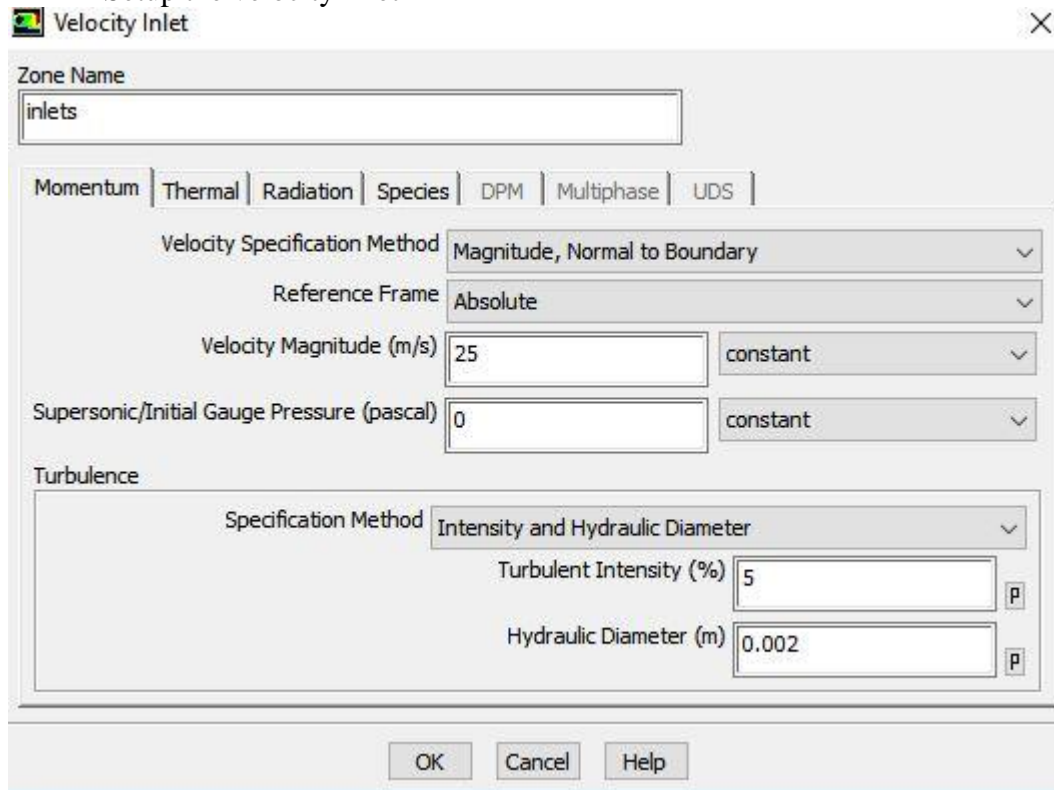
## APPENDIX 3

The tutorial process of the combustion simulation by used of FLUENT software:

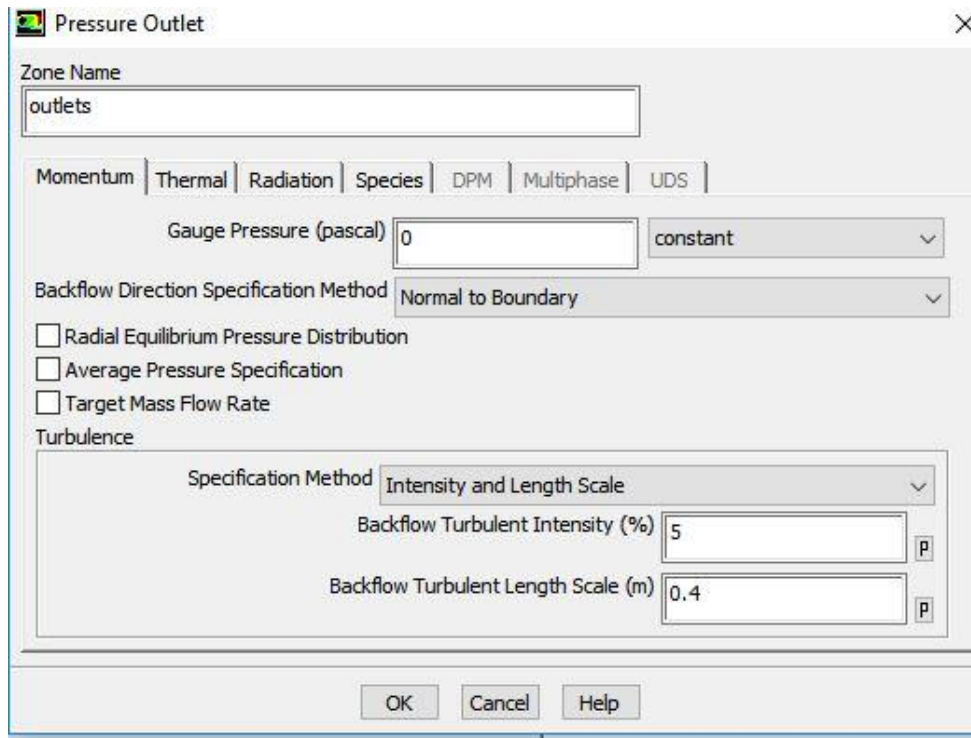
- Setup the combustion reaction



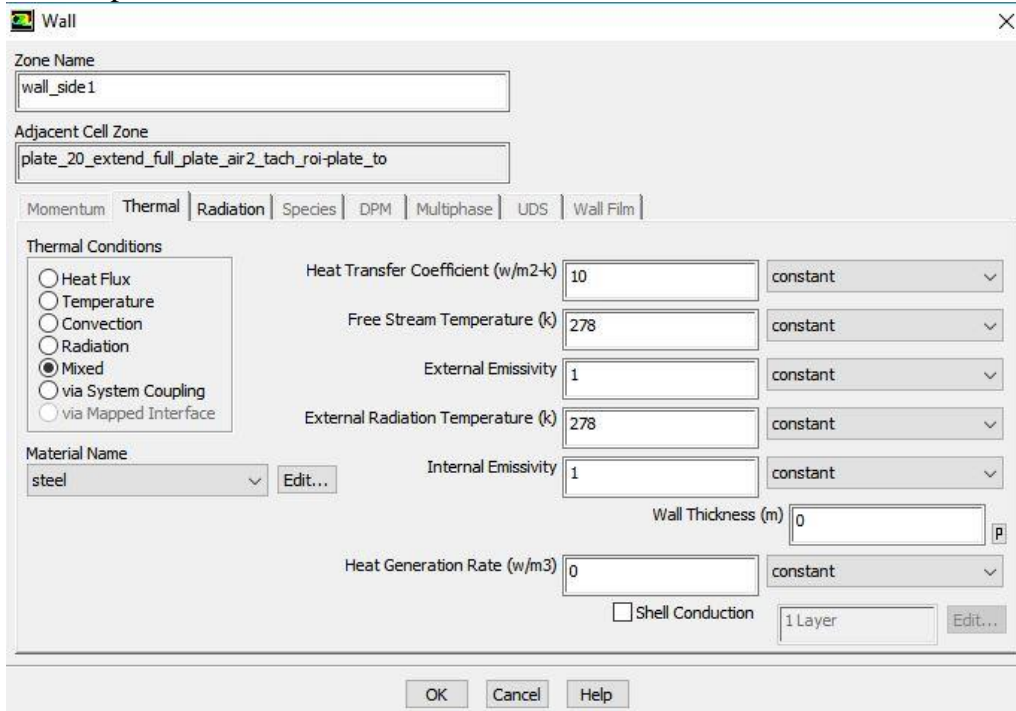
- Setup the velocity inlet



- Setup the pressure outlet



- Set up the convection and radiation effect on the walls



- Finally, run the calculation with the iteration of 2000 then obtaining the results.